Structural Identification and Buffet Alleviation of Twin-Tailed Fighter Aircraft

Ayman Aly El-Badawy

Dissertation submitted to the Faculty of the
Virginia Polytechnic Institute and State University
in partial fulfillment of the requirements for the degree of

Doctor of Philosophy
in
Mechanical Engineering

Ali H. Nayfeh, Chairman
Dean T. Mook
Gordon Kirk
William R. Saunders
Mehdi Ahmadian
Harley H. Cudney

March 30, 2000
Blacksburg, Virginia

Keywords: Buffet, Active Control, Perturbation, Nonlinear Dynamics,
Smart Structures, Neural Networks, Fighter Aircraft

Structural Identification and Buffet Alleviation of Twin-Tailed Fighter Aircraft

Ayman Aly El-Badawy

(ABSTRACT)

We tackle the problem of identifying the structural dynamics of the twin tails of the F-15 fighter plane. The objective is to first investigate and identify the different possible attractors that coexist for the same operating parameters. Second is to develop a model that simulates the experimentally determined dynamics. Third is to suppress the high-amplitude vibrations of the tails due to either principal parametric or external excitations.

To understand the dynamical characteristics of the twin-tails, the model is excited parametrically. For the same excitation amplitude and frequency, five different responses are observed depending on the initial conditions. The coexisting five responses are the result of the nonlinearities. After the experimental identification of the system, we develop a model to capture the dynamics realized in the experiment.

We devise a nonlinear control law based on cubic velocity feedback to suppress the response of the model to a principal parametric excitation. The performance of the control law is studied by comparing the open- and closed-loop responses of the system. Furthermore, we conduct experiments to verify the theoretical analysis. The theoretical and experimental findings indicate that the control law not only leads to effective vibration suppression, but also to effective bifurcation control.

We investigate the design of a neural-network-based adaptive control system for active vibration suppression of the model when subjected to a parametric excitation. First, an emulator neural network was trained to represent the structure and thus used to predict the future responses of the model. Second, a neurocontroller is developed to determine the necessary control action. The computer-simulation studies show great promise for artificial neural networks to control the model vibrations caused by parametric excitations.

We investigate the use of four different control strategies to suppress high-amplitude responses of the F-15 fighter to a primary resonance excitation. The control strategies are linear velocity feedback, nonlinear velocity feedback, positive position feedback, and saturation-based control. For each case, we conduct bifurcation analyses for the open- and closed-loop responses of the system and investigate theoretically the performance of the different control strategies. We also calculate the instantaneous power requirements of each control law. The experimental results agree with the theoretical findings.

To my parents

Acknowledgments

I cannot ever give Professor Ali Nayfeh the credit that he deserves. I was lucky to have him as my advisor. Professor Nayfeh is the one who initiated my interest in the area of nonlinear dynamics. His patient support and vast knowledge helped me greatly in producing this Dissertation.

I thank Professors Dean Mook, Harley Cudney, Mehdi Ahmadian, Will Saunders, and Gordon Kirk for serving on my committee and reading my Dissertation.

I also thank my past and present labmates Dr. Char-Ming Chin, Dr. Jon Pratt, Dr. Shafic Oueini, Dr. Haider Arafat, Osama Ashour, Sean Fahey, Benjamin Hall, and Ryan Krauss. In addition to their stimulating conversations and friendship, their questions and suggestions helped me understand better my work. A word of appreciation goes to Mrs. Sally Shrader for her indispensable help and friendship.

This work was supported by the Air Force Office of Scientific Research under Grant No. F496020-98-1-0393.

Most of all, I want to thank my beloved wife for her unconditional love and support. I also want to express my deepest gratitude toward my parents, who sacrificed enormously for their children, for their unconditional support in my life. I am also in debt to my elder brother and his family for their support and help in pursuing my graduate study. Finally, I would like to dedicate this Dissertation to my family, wife, Nour, and our soon-to-be-borne baby.

Ayman Aly El-Badawy
March 2000

Contents

List of Figures

Chapter 1

Introduction

1.1 Buffeting phenomenon

The design of present aircraft demands light-weight, high-aspect-ratio wings and tails that are very flexible. This in turn leads to many aeroelastic problems. In fact, aeroelasticity is not only important in the design of airplanes, but also in many other applications, such as suspension bridges, power lines, tall buildings, and chimney stacks. These are only few examples to mention.

In general, aeroelasticity deals with the behavior of any elastic body in an airstream wherein there is significant reciprocal interaction between the deformation and the flow. The main problems of aeroelasticity are the determination of the stability and the response of the elastic body. These problems can be classified into divergence, flutter, loss and reversal of control, and buffeting [1, 2]. In this work we are concerned with buffeting.

Historically, the term buffeting was originated in connection with an accident of a commercial airplane (type Junkers F13) at Meopham, England, on July 21, 1930. Four passengers and two pilots were killed [3]. The British Aeronautical Research Committee conducted extensive laboratory investigations and concluded that the most probable cause of the accident was "buffeting" of the tail. In these wind-tunnel-model investigations, it was established that,

at large angles of attack (AOA), the tail vibrated intensely but irregularly, and the "mean" amplitude of vibration increased with the flow speed. The general picture is therefore as follows: Whenever separation occurs in a flow, the turbulence level increases. If an airfoil is situated in a turbulent flow, it buffets. Buffeting, however, is not limited to airfoils. The oscillation of a smokestack in the wake of another smokestack is also an example of buffeting. In this work, we are concerned with buffeting of the tails of high-performance twin-tail aircraft (HPTTA).

In HPTTA, buffet induced tail vibrations were first noticed through their destructive effects of induced fatigue cracks in the vertical tail structural assembly of the F-15 aircraft. These fatigue cracks were noticed shortly (less than six months) after the aircraft was placed in service during the seventies, and many high angles of attack were executed [4]. After repeated temporary structural repairs, a thorough investigation of the conditions leading to the fatigue cracks confirmed that buffet-induced tail vibrations were the cause. The damage location is found to be in the forward box near the top of the tail. Since the forward box is a bonded honeycomb sandwich assembly, cracks in it allow moisture to seep into the honeycomb core. As a result, corrosion and skin disbonding problems have arisen. Due to these effects, a significant amount of maintenance is spent on high-performance twin-tail aircraft vertical tail assemblies, such the F-14, F-15, F-18, and F-22. Moreover, buffeting puts a restriction on the angles of attack and speeds at which certain maneuvers can be executed.

1.2 Theories of Tail Buffeting

Aircraft buffet may originate from atmospheric turbulence (gust) and flow separation. For atmospheric turbulence, the external load-time history is typically measured on an actual airplane flying through a turbulent atmosphere to estimate the statistical nature of the gust problem. An interesting problem is thus how to derive from the experimental data the statistical information that is useful in airplane design. Another problem of practical importance is how to use the statistical information to predict theoretically the airplane

responses (acceleration, inertia load, stresses, etc.) to atmospheric turbulence [3]. Flow Separation may produce buffeting on the surface from which the separation originated. This is mainly true on aeroplane wings. In fact, although buffeting is unlikely to cause failure in wings, the ability of aircraft to aim missiles successfully is affected by the degree of buffeting [5]. Flow separation may produce buffeting on downstream surfaces. This is the reason behind tail buffet. This work is concerned with tail buffet.

Tail buffet is basically an incompressible flow phenomenon [6]. This is because empennage buffet occurs at high angles of attack, which can be attained only at relatively low dynamic pressures that do not exceed the design limit load of the aircraft. These conditions can be contrasted to those where wing buffet occurs. Wing buffet is usually considered to be a high dynamic pressure, transonic phenomenon. Having this in mind, it is necessary to know the buffet load characteristics that lead to tail vibrations. In this case(high angle of attack and low dynamic pressure), numerous numerical and experimental studies have been conducted to examine various aspects of the tail-buffet loads.

1.3 Buffet Background

Triplett [7] reported surface pressure measurements on rigid and aeorelastically scaled vertical tails. The spectra showed broad-band humps. The root-mean-square (RMS) levels on the inside surfaces were substantially lower than those on the outboard surfaces for the rigid tail. Fluctuating loads on the elastic tails were substantially (25%) higher than those on the rigid tails, and the RMS levels on the elastic tails were of the same order on the inboard and outboard surfaces. Sharp spectral peaks occured at the frequencies of the structural modes of the elastic tails.

Sellers *et al.* [8] presented detailed measurements of the flow over a 3%-scale model of a YF-17. They showed the dominance of the leading-edge extension (LEX) vortices and attributed the large velocity fluctuations (RMS values of 30% of the mean) at the vertical tails to the bursting of these vortices. Zimmerman *et al.* [9] extended the work of reference [7] to the F-

18 and developed a method for predicting tail buffet loads based on test data. They showed that buffet spectra could be extrapolated over large ranges of velocity, dynamic pressure, and model size and that wind-tunnel data could be used to predict flight loads.

Moss *et al.* [10] presented buffet response over a range of angles of attack, -10° to +40° , and a range of Mach numbers, 0.30 to 0.95, for a wind-tunnel model of the twin vertical tails of the F-18. They found that the buffet response occured in the first bending mode and was a maximum in the 30° to 40° angle-of-attack range. They also noted that the buffet response increased in a nonlinear fashion with increasing dynamic pressure.

Komerath *et al.* [11] studied the frequency content of the fluctuating flowfield over scaled models of F-15 and F-18 at high angles of attack using hot-film anemometry. They found that the spectra over the wing develop a narrowband peak, with the dominant frequency varying linearly with the freestream velocity at a fixed angle of attack. The frequency of the peak and the shape of the spectrum change with angle of attack. For angles of attack above 30° , they observed multiple peaks. They observed sharply peaked spectra near the top of the vertical tails of F-18 rigid models. These narrowband spectra were masked over the rest of the tail by the more intense broadband fluctuations due to the burst vortex from the leading-edge extensions.

Washburn *et al.* [12] measured the pressure fluctuations on both sides of the twin tails of a model with a 76° delta wing; one of the tails is rigid, while the other is flexible. They placed the tails at nine different positions. They calculated the mean and RMS values as well as the spectra of the pressures. They found out that buffeting on the vertical tails depends strongly on their locations. Moreover, they observed two distinct peaks in the flowfield downstream of the vortex breakdown; the magnitudes and frequencies of these peaks varied with the angle of attack. Additionally, it was found that the presence of a flexible tail can affect the unsteady pressures on the rigid tail.

Numerous numerical studies have also been conducted to examine various aspects of the buffet problem. Several numerical solutions were carried out by Kandil and his coworkers [13, 14, 15] to study the flow about a 76° sharp-edged delta wing exhibiting tail buffet. Aeroelastic

Figure 1.1: Flow visualization of leading-edge extension vortex burst, 30° angle of attack (Photograph Courtesy of the NASA Dryden Flight Research Center)

solutions were obtained by coupling the structural equations of motion for the vertical surface and the laminar Navier-Stokes equations while updating the grid displacement equations at each time step. Both subsonic and transonic flow regimes were examined. The flow conditions and wing angle of attack were selected to produce an unsteady vortex-breakdown flow.

Krist *et al.* [16] employed a combination of the Euler and laminar Navier-Stokes equations to describe the flow over a thin delta wing and swept at 76° and having sharp leading edges, with the vertical tails located downstream of the wing trailing edge. The computed results compared reasonably well with the experimental data. Rizetta [17] computed the flowfield over a 70° delta wing with rigid twin vertical tails. Navier-Stokes solutions obtained by employing two different turbulence models were compared to an inviscid calculation. The results indicate that the dominant features of the vortex/tail interaction could be reproduced by the Euler equations. Morton *et al.* [18] extended the computations of Rizzetta by allowing the tail structures to be flexible. The tail planform used is similar to that of an F-15. The interaction of a vortex undergoing breakdown and a flexible tail immersed in the broken down portion of the vortex was analyzed. They demonstrated an upstream movement of the vortex breakdown position as the magnitude of the tip deflection was increased, demonstrating the importance of fluid-structure feedback.

Several hypotheses have been advanced about the spectra of the fluctuations observed in

Figure 1.2: Buffet at high angle-of-attack on the F-15

the flowfield over twin-tailed swept wing aircraft at high angles of attack. In one hypothesis, the spectra of the buffet loads are broadband for very special flight conditions and narrowband for a wide range of conditions in which the dominant frequency varies substantially with flight conditions. Previous work has shown that such narrowband fluctuations are common to models of existing combat aircraft, generic wing-bodies, and swept delta wings. In another hypothesis, buffet loads are produced by vortices generated over highly swept leading-edge extensions of the wing. These vortices at some flight conditions burst and undergo violent breakdown near the vertical tails. The result is that the tails encounter large-amplitude fluctuations with a relatively broadband spectral distribution, causing high levels of aerodynamic forcing. Buffeting of the vertical tails of the F-18 (Figure 1.1) fits into this category.

When the wing sweep is below 50° , the vortex bursting phenomenon is generally not observed [19]. When the angle of attack α exceeds about 18° , the flowfield, beginning very near the wing-root juncture, appears to be a large swirling flow with no clear core. This has been declared to be a "post-burst" flow [20], but can be described more usefully as "never unburst flow" due to the absence of any region where actual "bursting" occurs [21]. The point is that there are no large-amplitude fluctuations to be seen: the broadband spectrum of low-intensity fluctuations, in an otherwise quasi-steady helical flowfield, has a low overall level of disturbance [22]. The "never-unburst" model has enabled systematic identification of other phenomena [23, 24]. Figure 1.2 shows an F-15 aircraft in a buffeting flow at a high angle of attack.

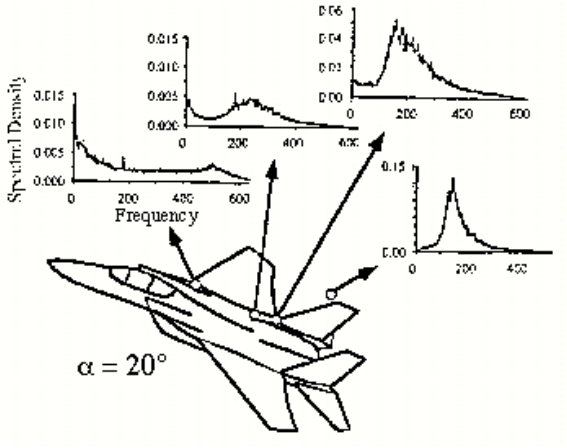

Figure 1.3: A 1/32-scale F-15 model at $33m/s$ (Komerath, et al., AIAA-91-0279)

In contrast to the F-18 case, the fluctuations over the F-15 and other moderately swept configurations start as a small blip in the velocity spectrum over the wing in a region where the flow has no strong vortex core and where the overall turbulence intensity is quite low. These fluctuations then amplify downstream and shift down in frequency. In front of the vertical tails, the spectrum of the velocity fluctuations is sharply peaked, with much of the energy being contained within a narrow frequency band. This is shown in Figure 1.3, from reference [22]. To understand this phenomenon, the flowfield was studied using hot-film probes [25], flow visualization [26], surface hot-film sensors, and laser velocimetry [27] on a 59.3° flat-plate delta wing. A 59.3° delta wing was selected because it exhibited the vortex-bursting phenomenon, and yet was of moderate-enough sweep to study buffet of the F-15. The fluctuations in the flowfield have been traced to counter-rotating structures, oriented along helical trajectories that lie nearly spanwise near the wing surface. These appear to be consistent with a centrifugal type of instability [24, 27, 28]. Using small fences, disruption of these structures near their origin has been shown to reduce the spectral peaks [27, 28].

1.4 Tail Buffet Alleviation

In the literature, many different approaches to tail buffet alleviation have been investigated, These approaches can be classified into a) aerodynamic techniques and b) structural dynamic techniques. Both techniques can further be divided into passive and active. Active in the sense that it requires power to drive the control system.

Aerodynamic techniques in general are used to reduce the strength or delay the formation of the vortices. The passive approach consists of adding fences on the wing or the fuselage. An example of this is the leading-edge-extension (LEX) fences on the F-18 aircraft. A LEX is a small trapezoidal plate that is attached to the leading edge of the wing. The effects of the LEX fences on tail buffeting have been studied extensively both numerically [29] and experimentally [30, 31, 32, 33]. Other research on fences include the work of Klein *et al.* [12,13] on the F-15 aircraft as well as on generic twin-tail aircraft. They used passive and active mini fences to modify the narrowband velocity fluctuations over a 59.3° delta wing at high angles of attack.

Several different active aerodynamic methods are also used. One of the these methods is based on Tangential-Leading-Edge-Blowing (TLEB) technique. It is used to reduce the "effective angle of attack" of the vortex core. Its application has been studied on single-fin aircraft [34] and twin-tail aircraft [35]. For the case of twin-tail configurations, Bean *et al.* [35] measured the buffeting response levels on a flexible fin, and the unsteady pressure on a rigid fin of similar planform for 60° delta wings with twin fin configurations. They used a laser-light-sheet-visualization technique to determine the vortical flow over the wings and hence reduce buffeting using TLEB. The idea behind TLEB is injecting a thin tangential jet into the cross-flow boundary layer near the leading edge, thereby enabling control of the vortex equilibrium condition at a given AOA. They concluded that a symmetric TLEB at a blowing momentum coefficient of 0.05 induced a linear shift in the buffeting excitation and response. Larger blowing rates reduced the overall buffet excitation levels and hence substantially reduced the buffeting response levels.

Another active aerodynamic technique is based on forebody tangential slot blowing. It has been shown [36] that such a technique reduces the buffet induced vibrations by moving away the main frequencies of the vortices from those of the structural modes. Finally, Kandil and his coworkers [37, 38] used flow suction along the vortex cores (FSVC) of the leading edges of a delta wing. Their numerical studies showed that FSVC can delay the vortex breakdown upstream of the twin tail and can also modify the vortex core path.

Structural dynamic passive techniques consist of reinforcing the fin assembly with patches both to repair existing defects and to stiffen the assembly. Ferman *et al.* [4] added composite skin doublers or "exoskin" to the main torque box as a form of stiffness modification. The F-15 stiffness modifications accomplished a 40 % increase in the overall sectional bending stiffness through the use of a pre-cured, cold bonded, carbon epoxy lay-up. This approach has achieved nearly an order-of-magnitude improvement in fatigue life. Also, selective stiffening of the main torque box by the bond-on exoskin is a simple concept for reducing buffet related vibrations and fatigue. Also, passive techniques can be implemented to enhance the structural damping. It has been increased by applying various methods, such as constrained-layer damping, damped link, tuned mass damper, interface damping, and solid-spacer damping [39]. The combined system has often a higher damping level that reduces the unwanted vibrations.

Structural dynamic active techniques use either the rudder or embedded smart materials in the tail together with a feedback control law. Lazarus *et al.* [40, 41] numerically studied the feasibility of using an active piezoelectric buffet-suppression system. This system called the Buffet Load Alleviation (BLA) consisted of a state-space aeroservoelastic model that incorporated 1) a finite element model of the tail structure, 2) an aerodynamic model, which accounted for the aerodynamic inertia damping and stiffness, and 3) a gust disturbance model to replicate the buffet spectrum. The aeroservoelastic model provided the predicted strain levels and accelerations on the tail. Optimization analysis was performed to place the minimum volume of piezoelectric actuator while maximizing its authority. Finally, a multi-input, multi-output controller was designed using linear quadratic Gaussian technique. The

effective reduction obtained using their design was estimated to be 57%, which exceeded their goal of 50%.

Recently, Spangler and Jacques [42] experimentally tested this BLA system on a full-scale F-18 empennage. They noted that the closed-loop attenuation of the strain tends to decrease as the severity of the buffet disturbance increases. They were able to meet the 50% reduction in the RMS strain at the aft root only at the nominal flight condition.

Hauch *et al.* [43] developed an Active Vertical Tail (AVT) to study the feasibility of buffet alleviation using piezoceramic actuators, strain gage sensors, and simple control techniques. The AVT was a 5% aeroelastically scaled structure with embedded piezoceramic wafers based on a generic aircraft. During wind-tunnel experiments, the control techniques used to reduce buffet were based on proportional, integral and derivative (PID) feedback from each of the sensors

Nitzsche *et al.* [44] compared the control using aerodynamic surfaces with that using piezoceramic actuators. Using LQG controllers, they showed that the performance of the strain actuation approach is better. Then Nitzsche *et al.* [45] tested their LQG controller on a full-scale F-18 empennage with strain actuation. Their results showed an attenuation exceeding 60% for the nominal flight configuration and 30% for the most severe case.

During the ACROBAT (Actively Controlled Response of Buffet Affected Tails) program, Moses [46] performed wind-tunnel tests on a 1/6 scale model of the F-18. The model was tested in the transonic dynamics tunnel at the NASA Langley Research Center. He used feedback control to suppress the response in the first bending mode of the tail. He used either the rudder on the starboard fin or some piezoceramic patches on the port fin. Reductions up to 60 % in the peak value of the PSD of the root bending moment at the frequency of the first bending mode were observed at gains well below the physical limits of the actuators. He noted that the performance of the control law appeared to deteriorate as the AOA was increased. He also anticipated that significant improvements in the performance of buffet-load alleviation over the entire range of AOA may be achieved by using adaptive control methods that adjust the parameters of the control law based on the AOA.

During the SIDEKIC (Scaling Influences Derived from Experimentally-Known Impact of Controls) program [47], a hybrid actuator system using the rudder for the control of the first bending mode and piezoceramic wafers for the control of the first torsional mode was developed. Pado and Lichtenwalner [48] demonstrated, during wind-tunnel tests, the ability of this hybrid actuator system in combination with neural predictive control to alleviate buffet-induced vibration in the vertical tails of the F-18 aircraft.

Hanagud *et al.* [49] developed a model for the vertical tail sub-assembly in the form of a transfer function matrix, which yields the natural frequencies, the mode shapes, and the damping ratios. They used acceleration feedback-control compensators. The effectiveness of their controller was validated by testing 1) the full-scale laboratory sub-assembly excited by a shaker and 2) a 1/16 scale model in a wind tunnel. Their results show that, as the disturbance increases, the effectiveness of the controller decreases. However, the minimum RMS reduction they were able to achieve was 17%.

A summary on tail-buffet-alleviation advances using smart structures can be found in the paper by Hopkins it et al. [50]. Finally, Moses [47] has presented the contributions of NASA in this field.

1.5 Alternate Solution: Neural Networks

Buffet data are extremely difficult to model using traditional regression techniques due to the multiple number of noisy parameters that interact in a nonlinear manner [6]. Neural networks are especially suited for modeling this type of data because their inter-connected algorithms can accommodate these nonlinearities.

A neural network can be defined as a massively parallel, highly interconnected collection of simple processing units that receives inputs (sensor output and input history), passes them through its network of weights and nonlinearities, and transforms them into outputs (future state predictions). These models can be created with much less effort than first-principle models and can capture real world effects. Figure 1.4 shows a typical architecture

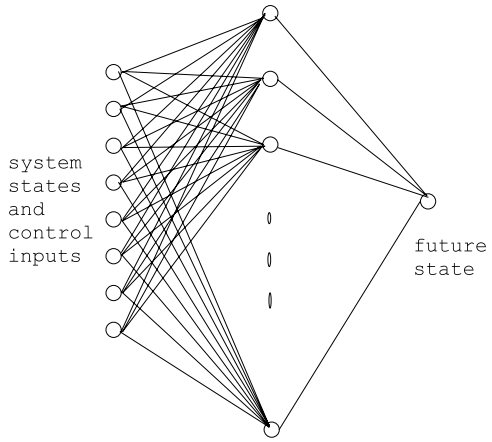

Figure 1.4: An example of a neural network model

for capturing the plant dynamics. Both past states and past controls applied at discrete instances of time are used along with the candidate future control to predict the future state of the system.

One of their most important characteristics is the ability to generalize from the data they have already seen, which makes them a good candidate for the sparse buffet data. Three neural-network paradigms can be used to model the data: the multi-layer perceptron trained with backpropagation (MLP) [51], the radial basis function network trained with orthogonal least-squares learning (RBF) [52], and the general regression neural network (GRNN) [53].

Jacobs *et al.* [54] were the first to employ a combined neural network and finite-element modeling to predict flexible tail responses based on rigid-pressure information. They concluded that, although the method is dependent on experimental data to train the neural network algorithms, it is robust enough to expand its knowledge base with additional aircraft data. The results show a potential to predict accurate RMS and frequency-dependent tail pressures as well as flexible responses while providing the future capability to incorporate upstream computational fluid dynamics data for advanced design aircraft buffet-pressure predictions.

In 1993, Boeing began looking for an adaptive control architecture for smart structures applications with automated synthesis, self optimization, real-time adaptation, nonlinear control, and fault tolerance capabilities. The nonlinear and adaptable requirements imme-

diately suggested the use of neural network technology in what they referred to be neural predictive control (NPC). A description of the NPC architecture developed at Boeing and its performance in suppressing the vibration of a cantilevered beam is given by Pado and Damle [55]. Other results of applying the NPC system for active flutter suppression is given by Lichtenwalner *et al.* [56].

Finally, Pado and Lichtenwalner [48] used NPC-based active control along with a combination of PZT patches and an active rudder to alleviate the effects of the buffeting environment on structural fatigue. Wind-tunnel tests were undertaken on a 1/16th scale YF-17 model with two flexible tails in the NASA Langley's Transonic Dynamics Tunnel (TDT). The tail was actuated with a hydraulically powered rudder for first-mode control and with a PZT patch for second-mode control. Reductions of up to 30% RMS in the vibration of the first mode and 12% RMS in the vibration of the second mode were achieved.

1.6 Organization of the Dissertation

The Dissertation is divided into two parts. In Part I, we consider the response of the twin-tail model to a principal parametric resonance, and in Part II, we consider its response to a primary resonance.

We begin Part I by developing a nonlinear model that describes the dynamics of the twin tails. We use experimental data obtained with a 1/16 structural dynamic scale model of the twin-tail assembly of the F-15 aircraft to develop a mathematical model of its dynamics. In Chapter 3, we consider the problem of suppressing the vibrations of the model when subjected to a principal parametric resonance, develop the control law using cubic velocity feedback, and investigate the dynamics of the closed-loop system. To implement the control law, we design and build analog circuits and apply the control law through the use of piezoelectric actuators and different feedback sensors.

In Chapter 4, we describe application of neural networks to identify and then control the model. All of the analysis made use of the identified model. And through simulations, a

neural network was devised that can emulate the response of the tails to different excitation amplitudes. A model reference adaptive control was then developed and trained to suppress the vibrations of the tails.

In Part II, we present four techniques for controlling the twin-tail vibrations subjected to a primary resonance. In Chapter 5, motivated by the results of Part I, we explore, using cubic velocity feedback, controlling externally forced tails. We compare the closed-loop results with those obtained using rate feedback. Furthermore, we compare the performance of both techniques.

In Chapter 6, we develop two linear tuned vibration absorbers: one absorber is tuned to each tail. We investigate the effect of changing the damping ratios of the absorbers and the value of the feedback gain on the response of the tails.

In Chapter 7, we develop two saturation-based absorbers: one absorber is tuned to each tail. Again, we investigate the effect of changing the damping ratios of the absorbers and the value of the feedback gain on the response of the tails. We also, compare the results of the quadratic absorber with those of the linear absorber. Finally, we carry out experiments using a digital signal processing board (DSP) that replaces the analog circuit. We report results that are in agreement with the theoretical development.

We end the Dissertation in Chapter 8 with a summary of our findings and suggestions for future work.

Part I

Parametric Excitation

Chapter 2

Nonlinear Identification

2.1 Introduction

A complete understanding of the tail buffet loads and the tail responses will eventually lead to the ability of predicting and alleviating buffeting. As mentioned in the introduction, buffet loads on the F-15 tails have a single frequency. The purpose of this chapter is to develop a scheme for the nonlinear identification of the linear and nonlinear dynamical characteristics of the twin-tail structure of F-15 aircraft using such an excitation. The model is then used to develop control strategies for buffet alleviation.

We use nonlinear identification techniques to estimate the nonlinear parameters in a mathematical model of the tail assembly. Nayfeh *et al.* [3] proposed a consistent methodology whereby perturbation techniques, complex Fourier amplitudes, and higher-order statistics can be combined to characterize and quantify the parameters of nonlinear systems. They used the method to identify the parameters of a three-beam two-mass frame. Fahey and Nayfeh [57] estimated the nonlinear parameters by regressive fits. We extend these techniques to the F-15 tail section.

2.2 Modeling

The tail section used in the experiments is a 1/16 dynamically scaled model of the F-15 tail assembly. The model was constructed by Professor Sathya Hanagud of the Georgia Institute of Technology from a series of aluminum channels, brass rings, composite plates, metal masses, and various adhesives, as shown in Figure 2.1. The model is approximately 0.355 m long, 0.228 m tall, and 0.482 m wide. The objective of this work is to develop a mathematical model that can capture the dynamics of the twin-tail assembly and identify its linear and nonlinear parameters. We use a combination of experimental modal analysis, nonlinear vibration testing, and perturbation methods.

For the nonlinear vibration testing, we mount the model on a 250-lb shaker and excite it with a principal parametric resonance. The tail deflections are measured with a series of four strain gages. The centers of the gage pairs are 0.9 cm and 8.5 cm from the top of the aluminum channels. One pair is on the outside of the right vertical tail; the other pair is on the outside of the left vertical tail. Changes in the gages are measured with a strain gage conditioning amplifier, in a quarter bridge configuration.

In the nonlinear identification, we exploit resonances to maximize the influence of the nonlinear parameters on the response. For the arrangement in Figure 2.2, the maximum response occurs when the excitation frequency is near twice the natural frequency of either of the vertical tails; that is, principal parametric resonance.

A series of bolts and several positioning blocks fixes the model to a 250-lb shaker. In this way, we are able to excite parametrically the tails without any additional masses. The shaker excitation is measured with an accelerometer studded to the base. The accelerometer signal is conditioned with an amplifier. The shaker amplifier is driven with a signal generator. The signal from the accelerometer amplifier and the strain gage conditioner is read with a data acquisition computer using LABVIEW software. The signals sent to the data acquisition computer are conditioned with a multiple channel filter set at 100 Hz low pass. The system identification is carried out using a four-channel signal analyzer and an oscilloscope. An

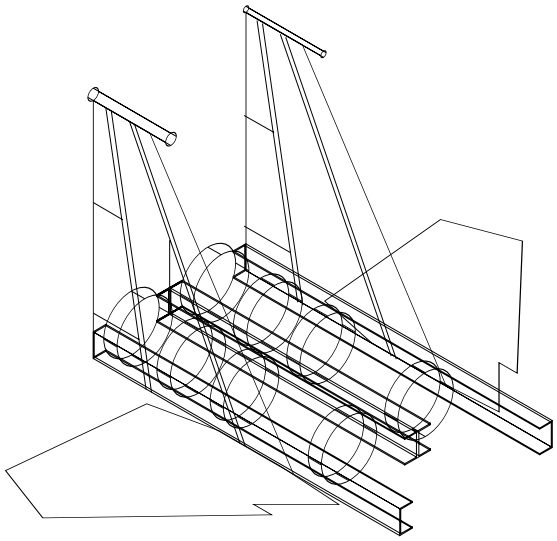

Figure 2.1: A three-dimensional view of the twin tails

impulse force hammer is also employed for impact testing. Figure 2.2 shows the experimental setup.

The experimental results show that the tails are responding in their first bending modes. Hence, the assembly is modeled with two oscillators, each describing a tail. We let u_1 and u_2 denote the generalized coordinates of the first bending modes of the two tails and let ω_1 and ω_2 be their linear undamped natural frequencies. For energy dissipation, we note that the surface areas of the tails are large and hence include both viscous damping and airflow drag. Thus, we incorporate linear and quadratic damping terms. To account for large deflections, we add a cubic nonlinear term to each oscillator. By plucking one tail, we have obtained a response in the other tail. Hence, we include linear coupling terms. They account for structural as well as aerodynamic coupling between the tails. Thus, we assume that the dynamics of the tails are governed by the following two mass-normalized second-order coupled differential equations:

$$\ddot{u}_1 + \omega_1^2 u_1 = -2\mu_1 \dot{u}_1 - \alpha_1 u_1^3 - \mu_3 \dot{u}_1 \mid \dot{u}_1 \mid + k(u_2 - u_1) \tag{2.1}$$

$$\ddot{u}_2 + \omega_2^2 u_2 = -2\mu_2 \dot{u}_2 - \alpha_2 u_2^3 - \mu_4 \dot{u}_2 \mid \dot{u}_2 \mid + k(u_1 - u_2) \tag{2.2}$$

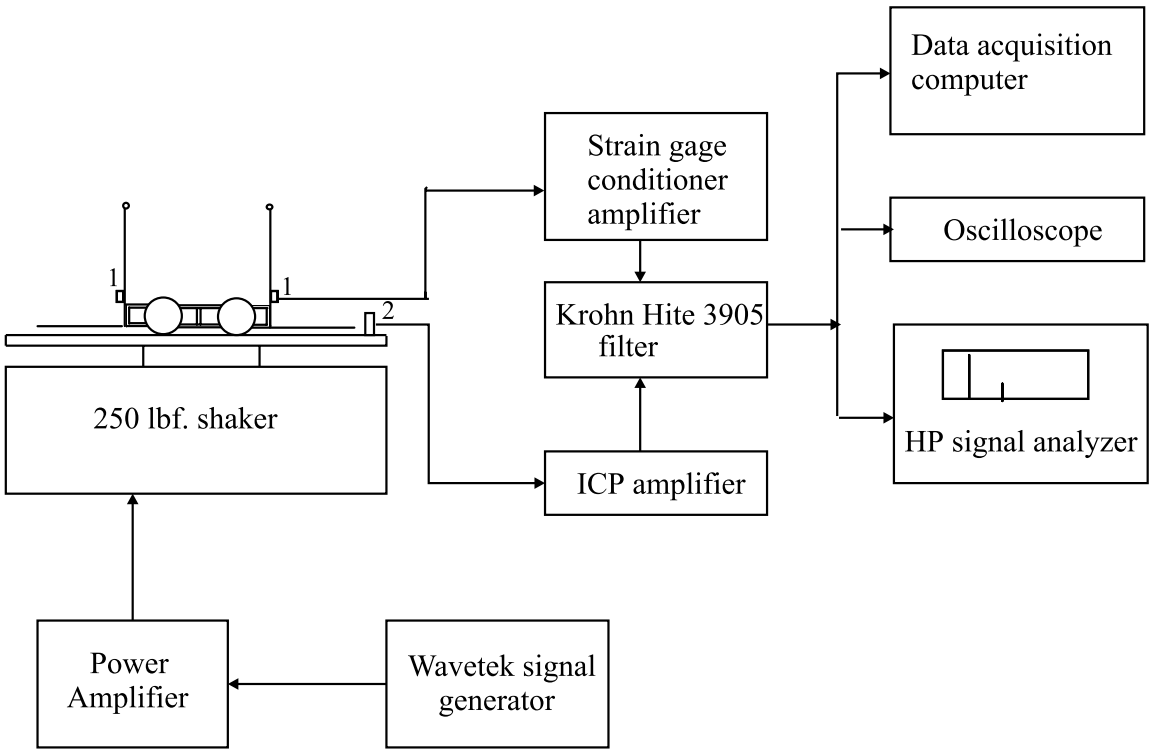

1: Strain gage
2: Accelerometer

Figure 2.2: Experimental setup

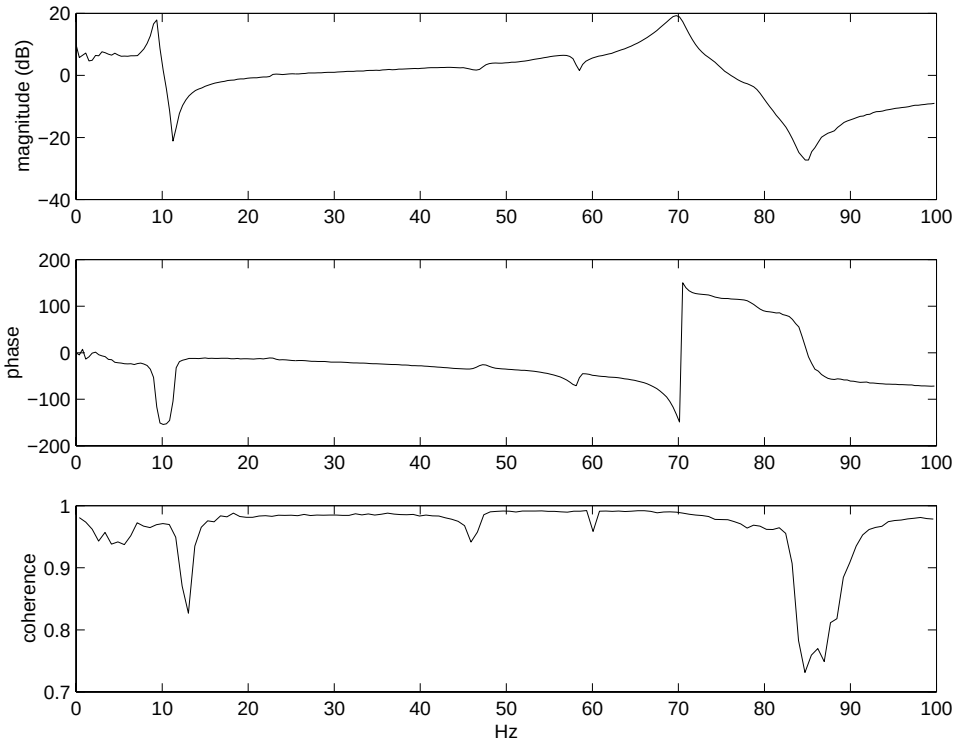

Figure 2.3: Frequency-response and coherence functions for the right tail

where $\omega_2 \approx \omega_1$. For the arrangement shown in Figure 2.2, we add the forcing terms $u_1\eta_1 F\cos(\Omega t+\tau_1)$ and $u_2\eta_2 F\cos(\Omega t+\tau_2)$ to the right-hand side of equations (2.1) and (2.2). To induce the maximum response, we let $\Omega \approx 2\omega_1$.

2.3 Identification of Linear Terms

The first step in the identification of any nonlinear system is the identification of its linear parameters: natural frequencies, damping ratios, and modal factors of the dominant modes. To accomplish this, we used experimental modal analysis. We used an impact hammer to excite the structure and then generated frequency-response functions. We averaged the transfer functions of 10 sequential hammer impacts. We consistently tried to strike the tails in the normal direction and at the same location every time. By monitoring the frequency

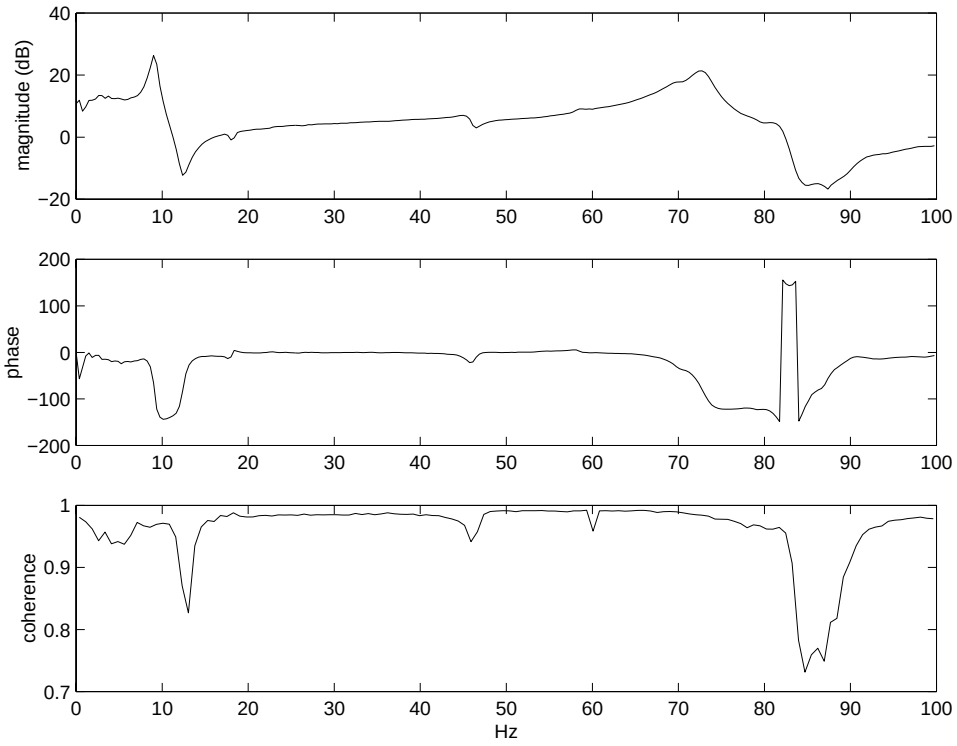

Figure 2.4: Frequency-response and coherence functions for the left tail

spectrum, we chose a tip for the hammer such that the drop in the frequency spectrum of an impact was less than 10% in the frequency range of interest. To avoid leakage, we used an exponential window. We zoomed around the first natural frequency to improve the resolution and hence to better estimate the linear identified parameters. During the experiments, we periodically checked the natural frequencies to detect any fatigue damage. The hammer impacts were done very close to the strain gages to realize a collocated response.

In Figures 2.3 and 2.4, we show the average frequency-response functions (FRFs) and their coherence functions for the right and left tails, respectively. Double hits were avoided. Clearly the tails resonant peaks are fairly well separated. An antiresonance always follows a resonance, which is a characteristic of a point FRF. The coherence function drops at the anti resonances, as expected.

We used very small excitation levels to obtain the frequency-response functions shown in Figures 2.3 and 2.4. The transfer functions are sensitive to slight changes in the excitation level. The location of the first natural frequency changes with excitation level.

The experimentally determined natural frequency of the first bending mode of the right tail is 9.135 Hz and that of the left tail is 9.05 Hz. An estimate of the linear damping ratios of the tails were found using both the half-power point and the logarithmic decrement over ten periods of the oscillations of each tail. The average was used to give a damping ratio of 0.14% for the right tail and 0.19% for the left tail. The values obtained with both techniques were nearly equal. An alternate way of estimating the linear damping coefficients is through a nonlinear technique, as discussed in the next section.

2.4 Identification of Nonlinear Terms

We used the method of multiple scales [58, 59] to derive four first-order nonlinear differential equations governing the modulation of the amplitudes and phases of both tails. These equations were used to construct the steady-state amplitudes and phases as functions of the excitation amplitude and frequency. We estimated the parameters of the model from

regressive fits between the experimentally and theoretically determined steady-state response amplitudes.

2.4.1 Approximate Solution

To determine an approximate solution of equations (2.1) and (2.2), we introduce a nondimensional parameter ϵ as a bookkeeping parameter. Then, we scale the α_i, μ_i, k, and F as $\epsilon\alpha_i, \epsilon\mu_i, \epsilon k$, and ϵF. Moreover, to quantitatively describe the nearness of the resonances, we introduce the detuning parameters σ_1 and σ_2 defined by $\Omega = 2\omega_1 + \epsilon\sigma_1$ and $\omega_2 = \omega_1 + \epsilon\sigma_2$.

Using the method of multiple scales, we seek a first-order uniform expansion of the solution of equations (2.1) and (2.2) in the form

$$u_1 = u_{11}(T_0, T_1) + \epsilon u_{12}(T_0, T_1) + \cdots \tag{2.3}$$

$$u_2 = u_{21}(T_0, T_1) + \epsilon u_{22}(T_0, T_1) + \cdots \tag{2.4}$$

where $T_0 = t$ is a fast time scale and $T_1 = \epsilon t$ is a slow time scale. In terms of T_0 and T_1, the time derivatives become

$$\frac{d}{dt} = D_0 + \epsilon D_1 + \cdots \tag{2.5}$$

$$\frac{d^2}{dt^2} = D_0^2 + 2\epsilon D_0 D_1 + \cdots \tag{2.6}$$

where $D_n = \frac{\partial}{\partial T_n}$. Substituting equations (2.3)–(2.6)into equations (2.1) and (2.2) and equating coefficients of like powers of ϵ gives

$O(\epsilon^0)$:

$$D_0^2 u_{11} + \omega_1^2 u_{11} = 0 \tag{2.7}$$

$$D_0^2 u_{21} + \omega_2^2 u_{21} = 0 \tag{2.8}$$

$O(\epsilon)$:

$$D_0^2 u_{12} + \omega_1^2 u_{12} = -2D_0 D_1 u_{11} - 2\mu_1 D_0 u_{11} + \eta_1 k_1 (u_{21} - u_{11})$$
$$-\alpha_1 u_{11}^3 - \mu_3 D_0 u_{11} \mid D_0 u_{11} \mid$$

$$+\eta_1 u_{11} F\cos(\Omega t+\tau_1) \tag{2.9}$$

$$\begin{aligned} D_0^2 u_{22}+\omega_2^2 u_{22} = & -2D_0D_1u_{21}-2\mu_2 D_0 u_{21}+\eta_2 k_2(u_{11}-u_{21}) \\ & -\alpha_2 u_{21}^3-\mu_4 D_0 u_{21}\mid D_0 u_{21}\mid \\ & +\eta_2 u_{21} F\cos(\Omega t+\tau_2) \end{aligned} \tag{2.10}$$

The general solution of equations (2.7) and (2.8) can be written as

$$u_{11}=A_1(T_1)e^{i\omega_1 T_0}+\bar{A}_1(T_1)e^{-i\omega_1 T_0} \tag{2.11}$$

$$u_{21}=A_2(T_1)e^{i\omega_2 T_0}+\bar{A}_2(T_1)e^{-i\omega_2 T_0} \tag{2.12}$$

where the $A_i(T_1)$ are determined by eliminating the secular terms from the next-order approximation.

Substituting equations (2.11) and (2.12) into equations (2.9) and (2.10) yields

$$\begin{aligned} D_0^2 u_{12}+\omega_1^2 u_{12} = & -2i\omega_1(A_1' e^{i\omega_1 T_0}+2i\omega_1 \bar{A_1}' e^{-i\omega_1 T_0})-2\mu_1 i\omega_1 A_1 e^{i\omega_1 T_0}+2\mu_1 i\omega_1 \bar{A}_1 e^{-iw_1 T_0} \\ & +\eta_1 k(A_2 e^{i\omega_2 T_0}+\bar{A}_2 e^{-i\omega_2 T_0}-A_1 e^{i\omega_1 T_0}-\bar{A}_1 e^{-i\omega_1 T_0})-\alpha_1 A_1^3 e^{3i\omega_1 T_0} \\ & -3\alpha_1 A_1^2 \bar{A}_1 e^{iw_1 T_0}-3\alpha_1 A_1 \bar{A_1}^2 e^{-i\omega_1 T_0}-\alpha_1 \bar{A_1}^3 e^{-3i\omega_1 T_0}-\mu_3[(i\omega_1 A_1 e^{i\omega_1 T_0} \\ & -i\omega_1 \bar{A}_1 e^{-i\omega_1 T_0})|i\omega_1 A_1 e^{i\omega_1 T_0}-i\omega_1 \bar{A}_1 e^{-i\omega_1 T_0}|]+\eta_1 \frac{F}{2}(A_1 e^{i\omega_1 T_0} \\ & +\bar{A}_1 e^{-i\omega_1 T_0})(e^{i(2\omega_1 T_0+\sigma_1 T_1+\tau_1)}+e^{-i(2\omega_1 T_0+\sigma_1 T_1+\tau_1)}) \end{aligned} \tag{2.13}$$

$$\begin{aligned} D_0^2 u_{22}+\omega_2^2 u_{22} = & -2i\omega_2(A_2' e^{i\omega_2 T_0}+2i\omega_2 \bar{A_2}' e^{-i\omega_2 T_0})-2\mu_2 i\omega_2 A_2 e^{i\omega_2 T_0}+2\mu_2 i\omega_2 \bar{A}_2 e^{-iw_2 T_0} \\ & +\eta_2 k(A_2 e^{i\omega_2 T_0}+\bar{A}_2 e^{-i\omega_2 T_0}-A_2 e^{i\omega_2 T_0}-\bar{A}_2 e^{-i\omega_2 T_0})-\alpha_2 A_1^3 e^{3i\omega_2 T_0} \\ & -3\alpha_2 A_2^2 \bar{A}_2 e^{iw_2 T_0}-3\alpha_2 A_2 \bar{A_2}^2 e^{-i\omega_2 T_0}-\alpha_2 \bar{A_2}^3 e^{-3i\omega_2 T_0}-\mu_4[(i\omega_2 A_2 e^{i\omega_2 T_0} \\ & -i\omega_2 \bar{A}_2 e^{-i\omega_2 T_0})|i\omega_2 A_2 e^{i\omega_2 T_0}-i\omega_2 \bar{A}_2 e^{-i\omega_2 T_0}|]+\eta_2 \frac{F}{2}(A_2 e^{i\omega_2 T_0} \\ & +\bar{A}_2 e^{-i\omega_2 T_0})(e^{i(2\omega_2 T_0+\sigma_4 T_1+\tau_2)}+e^{-i(2\omega_2 T_0+\sigma_4 T_1+\tau_2)}) \end{aligned} \tag{2.14}$$

Eliminating the terms that produce secular terms in equations (2.13) and (2.14) gives

$$2i\omega_1 A_1' = -2\mu_1 i\omega_1 A_1+\eta_1 k A_2 e^{i\sigma_2 T_1}-\eta_1 k A_1-3\alpha_1 A_1^2 \bar{A}_1$$

$$+\frac{1}{2}\eta_1 F\bar{A}_1 e^{i\sigma_1 T_1+\tau_1} - i\frac{4}{3\pi}\mu_3\omega_1^2 a_1^2 e^{i\beta_1} \tag{2.15}$$

$$2i\omega_2 A_2' = -2\mu_2 i\omega_2 A_2 + \eta_2 k A_1 e^{i\sigma_3 T_1} - \eta_2 k A_2 - 3\alpha_2 A_2^2\bar{A}_2$$
$$+\frac{1}{2}\eta_2 F\bar{A}_2 e^{i\sigma_4 T_1+\tau_2} - i\frac{4}{3\pi}\mu_4\omega_2^2 a_2^2 e^{i\beta_2} \tag{2.16}$$

Expressing the A_n in terms of polar coordinates as

$$A_n = \frac{1}{2}a_n e^{i\beta_n} \tag{2.17}$$

and separating real and imaginary parts in equations (2.15) and (2.16), we obtain

$$a_1' = -\mu_1 a_1 + \frac{\eta_1 F a_1}{4\omega_1}\sin\gamma_2 - \frac{4\mu_3\omega_1}{3\pi}a_1^2 + \frac{\eta_1 k a_2}{2\omega_1}\sin\gamma_1 \tag{2.18}$$

$$a_2' = -\mu_2 a_2 + \frac{\eta_2 k a_1}{2\omega_2}\sin\gamma_1 - \frac{4\mu_4\omega_2}{3\pi}a_2^2 - \frac{\eta_2 F a_2}{4\omega_2}\sin(\tau_1-\tau_2+2\gamma_1-\gamma_2) \tag{2.19}$$

$$\gamma_1' = -\frac{\eta_1 k}{2\omega_1} + \frac{\eta_2 k}{2\omega_2} + \sigma_2 - \frac{\eta_2 F}{4\omega_2}\cos(\tau_1-\tau_2+2\gamma_1-\gamma_2) + \frac{\eta_1 F}{4\omega_1}\cos\gamma_2 - \frac{3\alpha_1}{8\omega_1}a_1^2$$
$$-\frac{\eta_2 k a_1}{2a_2\omega_2}\cos\gamma_1 + \frac{\eta_1 k a_2}{2a_1\omega_1}\cos\gamma_1 + \frac{3\alpha_2}{8\omega_2}a_2^2 \tag{2.20}$$

$$\gamma_2' = -\frac{\eta_1 k}{\omega_1} + \sigma_1 + \frac{\eta_1 F}{2\omega_1}\cos\gamma_2 - \frac{3\alpha_1}{4\omega_1}a_1^2 + \frac{\eta_1 k a_2}{a_1\omega_1}\cos\gamma_1 \tag{2.21}$$

where

$$\gamma_1 = \sigma_2 T_1 - \beta_1 + \beta_2$$
$$\gamma_2 = \sigma_1 T_1 - 2\beta_1 + \tau_1 \tag{2.22}$$

2.4.2 Equilibrium Solutions and Their Stability

To determine the stability of the solutions of equations (2.15) and (2.16), we introduce the Cartesian transformation

$$A_k = \frac{1}{2}[p_k(T_1) - iq_k(T_1)]e^{(i\nu_k T_1+\frac{1}{2}\tau_k)}, \qquad k = 1,2 \tag{2.23}$$

where

$$\nu_1 = \beta_1' = \frac{1}{2}\sigma_1 \text{ and } \nu_2 = \beta_2' = \frac{1}{2}\sigma_1 - \sigma_2 \tag{2.24}$$

separate real and imaginary parts, and obtain

$$\begin{aligned} p_1' =& -\nu_1 q_1 - \mu_1 p_1 - \frac{1}{2\omega_1}\eta_1 k q_2 + \frac{1}{2\omega_1}\eta_1 k q_1 + \frac{3}{8\omega_1}\alpha_1 p_1^2 q_1 + \frac{3}{8\omega_1}\alpha_1 q_1^3 + \frac{\eta_1 F}{4\omega_1} q_1 \\ & -\frac{4}{3\pi}\mu_3 \omega_1 \sqrt{p_1^2 + q_1^2}\, p_1 \end{aligned} \tag{2.25}$$

$$\begin{aligned} q_1' =& \nu_1 p_1 - \mu_1 q_1 + \frac{1}{2\omega_1}\eta_1 k p_2 - \frac{1}{2\omega_1}\eta_1 k p_1 - \frac{3}{8\omega_1}\alpha_1 p_1^3 - \frac{3}{8\omega_1}\alpha_1 p_1 q_1^2 + \frac{\eta_1 F}{4\omega_1} p_1 \\ & -\frac{4}{3\pi}\mu_3 \omega_1 \sqrt{p_1^2 + q_1^2}\, q_1 \end{aligned} \tag{2.26}$$

$$\begin{aligned} p_2' =& -\nu_2 q_2 - \mu_2 p_2 - \frac{1}{2\omega_2}\eta_2 k q_1 + \frac{1}{2\omega_2}\eta_2 k q_2 + \frac{3}{8\omega_2}\alpha_2 p_2^2 q_2 + \frac{3}{8\omega_2}\alpha_2 q_2^3 + \frac{\eta_2 F}{4\omega_2} q_2 \\ & -\frac{4}{3\pi}\mu_4 \omega_2 \sqrt{p_2^2 + q_2^2}\, p_2 \end{aligned} \tag{2.27}$$

$$\begin{aligned} q_2' =& \nu_2 p_2 - \mu_2 q_2 + \frac{1}{2\omega_2}\eta_2 k p_1 - \frac{1}{2\omega_2}\eta_2 k p_2 - \frac{3}{8\omega_2}\alpha_2 p_2^3 - \frac{3}{8\omega_2}\alpha_2 p_2 q_2^2 + \frac{\eta_2 F}{4\omega_2} p_2 \\ & -\frac{4}{3\pi}\mu_4 \omega_2 \sqrt{p_2^2 + q_2^2}\, q_2 \end{aligned} \tag{2.28}$$

We set the time derivatives in equations (2.25)–(2.28) equal to zero and solve the resulting system of algebraic equations for p_1, q_1, p_2, and q_2 for a specified value of either σ_1, which is a measure of the detuning of the principal parametric resonance, or F, which is a measure of the forcing amplitude. The amplitudes a_1 and a_2 of the responses of the two tails were then calculated from $a_i = \sqrt{p_i^2 + q_i^2}$. Since there is no closed-form solution for the four algebraic equations, we resorted to numerical techniques. Numerical integration of the modulation equations for different sets of initial conditions was used to locate some of the possible solutions for a given σ_1 and F. Then, starting with these solutions, we used a pseudo arclength scheme [60] to trace the branches of the equilibrium solutions by varying either σ_1 or F.

The stability of a particular equilibrium solution is determined by examining the eigenvalues of the Jacobian matrix of the right-hand sides of equations (2.25)–(2.28). If the real part of each eigenvalue of the Jacobian matrix is negative, the corresponding equilibrium solution is asymptotically stable. If the real part of any of the eigenvalues is positive, the corresponding

equilibrium solution is unstable.

2.4.3 Curve Fitting of Amplitude Sweeps

To identify the nonlinear parameters, we held one of the tails completely fixed, set the excitation frequency at 18 Hz, and slowly swept the excitation amplitude. The resulting force-response curve is shown in Figure 2.5. Then we repeated the same test for the left tail. The results are shown in Figure 2.6.

Mathematically, we achieve the uncoupling by setting $k = 0$ in equations (2.15) and (2.16). Then, expressing A_1 in the polar form

$$A_1 = \frac{1}{2} a e^{i\beta} \tag{2.29}$$

setting $k = 0$, and separating real and imaginary parts in equations (2.15), we obtain

$$a' = -\mu_1 a - \frac{4\mu_3}{3\pi}\omega_1 a^2 + \frac{\eta_1 F a}{4\omega_1}\sin\gamma \tag{2.30}$$

$$a\beta' = \frac{3\alpha_1}{8\omega_1}a^3 - \frac{\eta_1 F a}{4\omega_1}\cos\gamma \tag{2.31}$$

where

$$\gamma = \sigma_1 T_1 - 2\beta + \tau_1 \tag{2.32}$$

The equilibrium solutions of equations (2.30)-(2.31) correspond to $a' = 0$ and $\gamma' = 0$. There are two possibilities: $a = 0$ and $a \neq 0$. In the latter case, the equilibrium solutions are given by

$$F\sin\gamma = \Psi a + \Gamma \tag{2.33}$$

$$F\cos\gamma = \Phi a^2 + \Lambda \tag{2.34}$$

where $\Psi = \frac{16\omega_1^2\mu_3}{3\pi\eta_1}$, $\Gamma = \frac{4\omega_1\mu_1}{\eta_1}$, $\Phi = \frac{3\alpha_1}{2\eta_1}$, and $\Lambda = -\frac{2\omega_1\sigma_1}{\eta_1}$. These equations constitute four equations in the four unknowns μ_1, μ_3, α_1, and η_1. From physics, we know that the damping terms must be positive while α_1 must be negative because the tails possess a softening-type nonlinearity. These constrains are enforced in the curve-fitting algorithm.

Squaring and adding equations (2.33) and (2.34) yields

$$F = \sqrt{\Phi^2 a^4 + (\Psi^2 + 2\Phi\Lambda)a^2 + 2\Psi\Gamma a + \Gamma^2 + \Lambda^2} \tag{2.35}$$

A curve-fitting algorithm that uses polynomials will not work in this case because of the radical and the absence of the cubic term. Hence, we used the MATLAB built-in function called *fmins*. To this end, we defined $c_1 = \Phi^2$, $c_2 = (\Psi^2 + 2\Phi\Lambda)$, $c_3 = 2\Psi\Gamma$, and $c_4 = \Gamma^2 + \Lambda^2$. Then, we minimized the error

$$E = \sum_{i=1}^{n} \left(F_i - \left(\sqrt{c_1 a^4 + c_2 a^2 + c_3 a + c_4} \right)_i \right)^2 \tag{2.36}$$

where n is the number of data points. *fmins* then returned a vector containing the coefficients that provide a local minimum near the initial guesses. Knowing the c_i allowed us to solve for Ψ, Γ, Φ, and Λ. Since the equations are nonlinear, they possess several solutions. Imposing the constrains on the signs and demanding that the orders of magnitude of the parameters be consistent with those expected, we eliminated some of these solutions. Moreover, we used the estimated linear damping coefficient as a check on that estimated with the nonlinear scheme. Finally, we determined μ_1, μ_3, α_1, and η_1.

We repeated the procedure for the left tail and identified μ_2, μ_4, α_2, and η_2.

In the experiments, we performed both amplitude and frequency sweeps. However, we only used the amplitude sweeps in the identification. The identified parameters for the right tail are $\zeta_1 = 0.01357$, $\mu_3 = 3.157 \times 10^{-4}\mu\epsilon^{-1}$, $\alpha_1 = -3.675 \times 10^{-2}\frac{1}{s^2\mu\epsilon^2}$, and $\eta_1 = 161.54\frac{1}{gs^2}$. The identified parameters for the left tail are $\zeta_2 = 0.01856$, $\mu_4 = 1.958864 \times 10^{-4}\mu\epsilon^{-1}$, $\alpha_2 = -2.977 \times 10^{-3}\frac{1}{s^2\mu\epsilon^2}$, and $\eta_2 = 275.12\frac{1}{gs^2}$. In Figure 2.5, we show the experimental data and the best fit for the right tail, whereas in Figure 2.6, we show the experimental data and the best fit for the left tail. The agreement is excellent, as expected.

2.5 Identification of Linear Coupling Coefficient

To estimate the linear coupling coefficient k, we note from equations (2.1) and (2.2) that it has two effects. First, the term $-ku_1$ in equation (2.1) and the term $-ku_2$ shift the linear

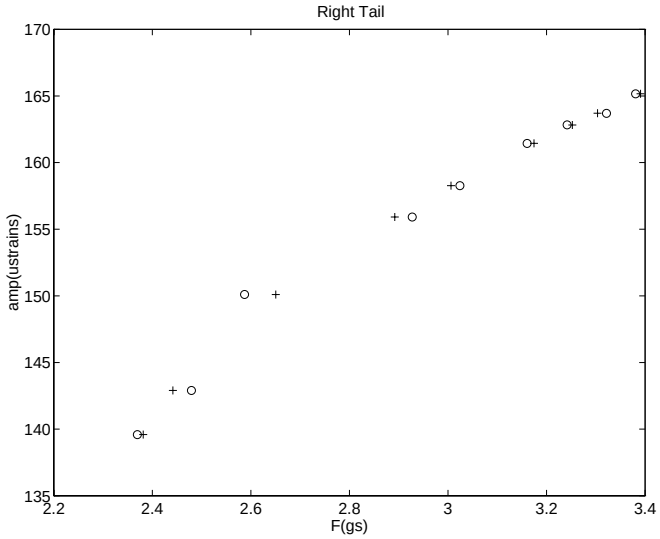

Figure 2.5: Least-square error fit of the experimental data for the right tail

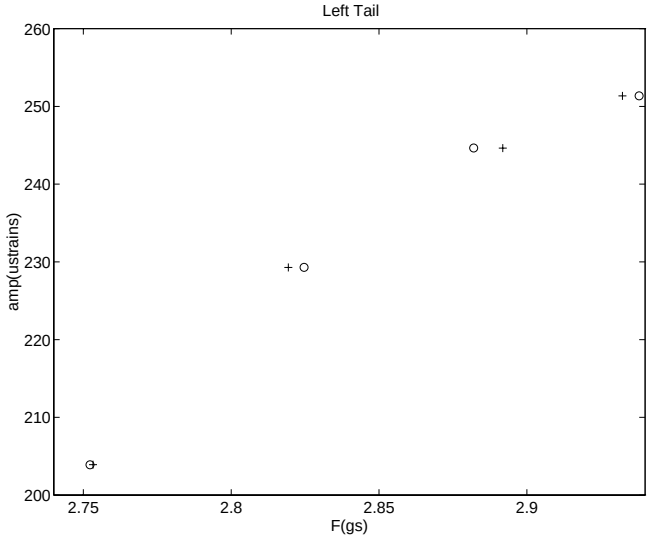

Figure 2.6: Least-squares error fit of the experimental data for the left tail

natural frequencies of the individual tails. Second, the term ku_2 in equation (2.1) and the term ku_1 in equation (2.2) couple the responses of the two tails. The shift in the natural frequencies is small and hence cannot be used to accurately estimate k. On the other hand, the coupling effect is very strong as described below and hence it can be used to accurately estimate k.

We fixed the excitation amplitude and varied the excitation frequency around 18 Hz. For the same excitation amplitude and frequency, we found five possible responses depending on the initial conditions: (a) very small-amplitude motions of both tails, (b) a large-amplitude motion of the right tail accompanied by a small-amplitude motion of the left tail, (c) a large-amplitude motion of the left tail accompanied by a small-amplitude motion of the right tail, (d) a large-amplitude motion involving both tails moving in phase, and (e) a large-amplitude motion involving both tails moving out-of-phase. The coexisting five responses are the result of the nonlinearities. These results point out some of the shortcomings of testing models with one rigid and one flexible tail or even testing only one tail counting on symmetry.

An interesting phenomenon was observed in the response of the scaled model. Fixing the excitation amplitude and frequency and plucking one tail, we observed that the oscillations of the plucked tail decayed with time and the unplucked tail oscillated with a large amplitude. The time traces of an example are shown in Figures 2.7 and 2.8.

By trial and error, we estimated k by comparing experimentally and theoretically obtained force-response curves. We determined force-response curves by using the experimental setup in Figure 2.2. We set the excitation frequency at 18 Hz and the excitation amplitude at $2.5g$. Then, we gave many disturbances to the tails, but the tails remained motionless. We incremented the excitation level and repeated the procedure. When the excitation level was increased to $2.7g$, we found two steady-state motions depending on the initial conditions: an in-phase motion and an out-of-plane motion. We picked one of these responses, recorded the time histories, and then incremented the excitation level. The procedure was repeated until the excitation level reached $3.40g$. Then, we converted the time records to the frequency domain. In Figure 2.9, we show an example of the excitation time history and the resulting

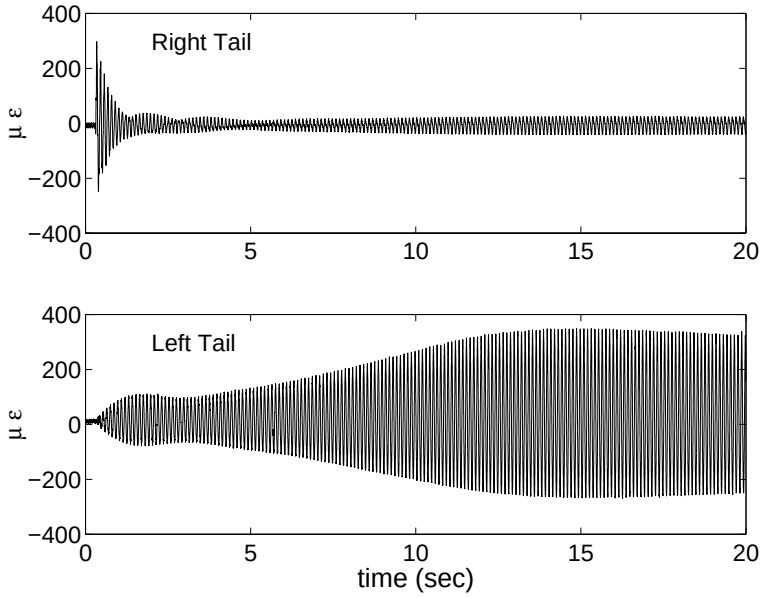

Figure 2.7: Energy transfer (right to left)

in-phase and out-of-phase time histories as well as their corresponding spectra. We extracted the response amplitudes and plotted the results in Figure 2.10 for the case in which the response of the left tail is larger than that of the right tail in one case and the response of the right tail is larger than that of the left tail in another case.

Next, we guessed a value for k, used the identified $\omega_i, \alpha_i, \mu_i$, and η_i, set the excitation frequency at 18 Hz, and chose a set of initial conditions. Then, we integrated the modulation equations (2.25)–(2.28). We varied the initial conditions and the excitation amplitude F until we obtained all nontrivial solutions. Then, we used a pseudo arclength to trace the equilibrium solutions. We varied k until the experimentally and theoretically obtained force-response curves are qualitatively in agreement. In this way, we estimated a value of 87 $(1/sec^2)$ for k. The theoretically obtained force-response curves are shown in Figure 2.11.

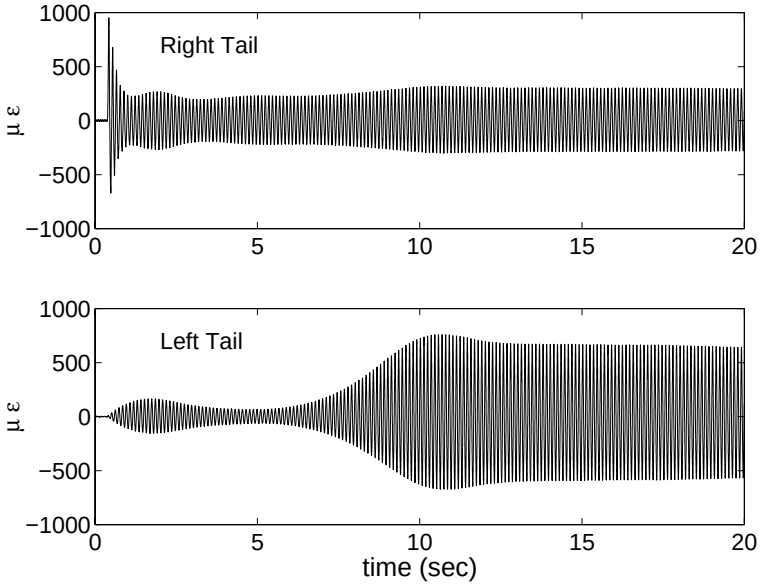

Figure 2.8: Energy transfer (left to right)

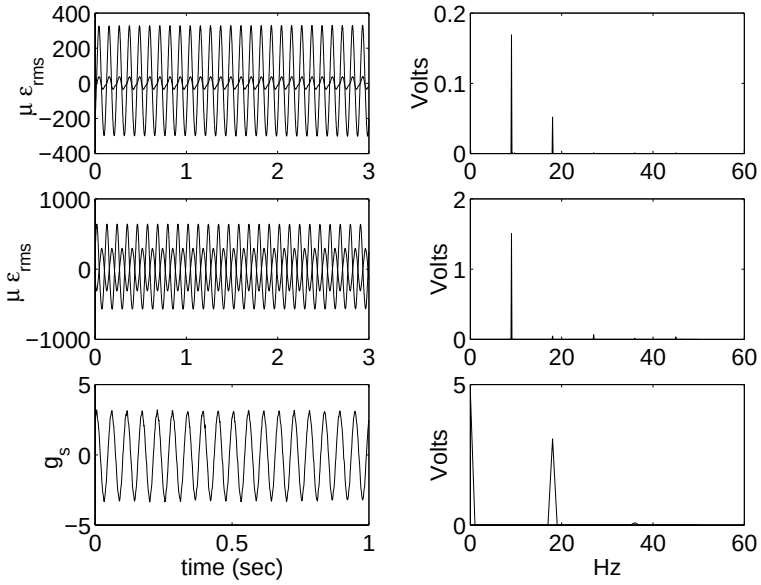

Figure 2.9: Examples of in-phase and out-of-phase motions and the excitation

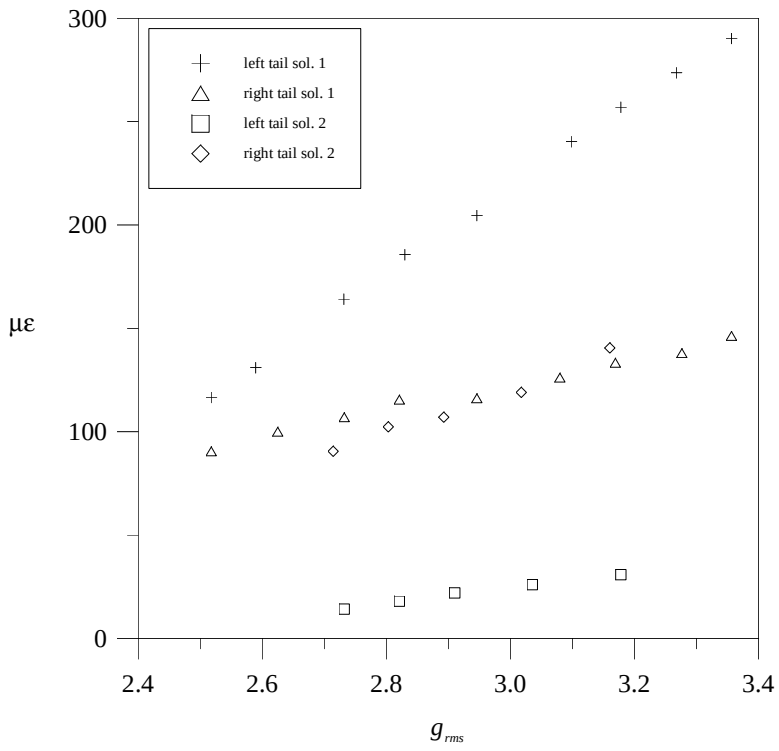

Figure 2.10: Experimentally obtained force-response curves (left tail response is larger than that of right tail) at 18.0 Hz. (Forward Sweep)

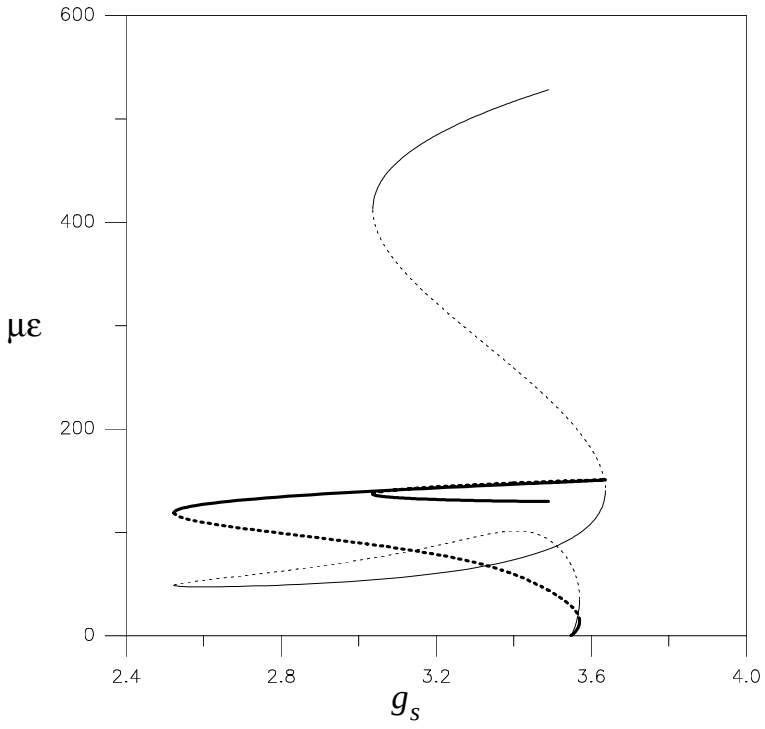

Figure 2.11: Theoretically obtained force-response curve at 18.0 Hz when $k = 87(1/sec^2)$

2.6 Nonlinear Testing

While conducting the experiments, we realized that, as we shake the tails harder, the location of the first natural frequency changed. Also, we realized as we incremented the frequency of excitation, the major peak in the spectrum of the response was exactly half the excitation frequency. This all made us sure that we had to consider nonlinearities in the system. In this work, we focus our attention on the first bending modes of the twin tails and assume that their responses are completely decoupled from those of the two wings, which in this case are directly excited.

To identify the system behavior in general we conducted amplitude and frequency sweeps both in the forward as well as in the backward direction. It is important to note here that, for the force-response curves, the results obtained in the backward sweep are similar to those obtained in the forward sweep. The backbone curves indicate that nonlinearities cannot be neglected and that linear theory is not sufficient to completely predict the dynamic behavior of the structural model.

2.7 Experimental Frequency-Response Curves

Figure 2.12 represents the experimentally obtained frequency-response curves at an excitation level of $3.2g$. The excitation frequency was varied in steps of 0.1 Hz in the frequency range from 15.5 Hz to 18.5 Hz. In the forward sweep, the trivial motion remained stable, although the tails were plucked, until the excitation frequency reached approximately 16.5 Hz. Plucking the tails at this frequency lead to a stable periodic motion for both tails while oscillating in-phase. And from the curve, it is clear that the amplitude of oscillations of the right tail is much larger than that of the left tail. Incrementing the frequency of excitation, the response amplitude of the right tail decreased almost exponentially while the left tail response changed slightly. At a frequency of 17.6 Hz, and without any plucking of the tails, the response of the left tail jumped and became larger than that of the right tail. It is

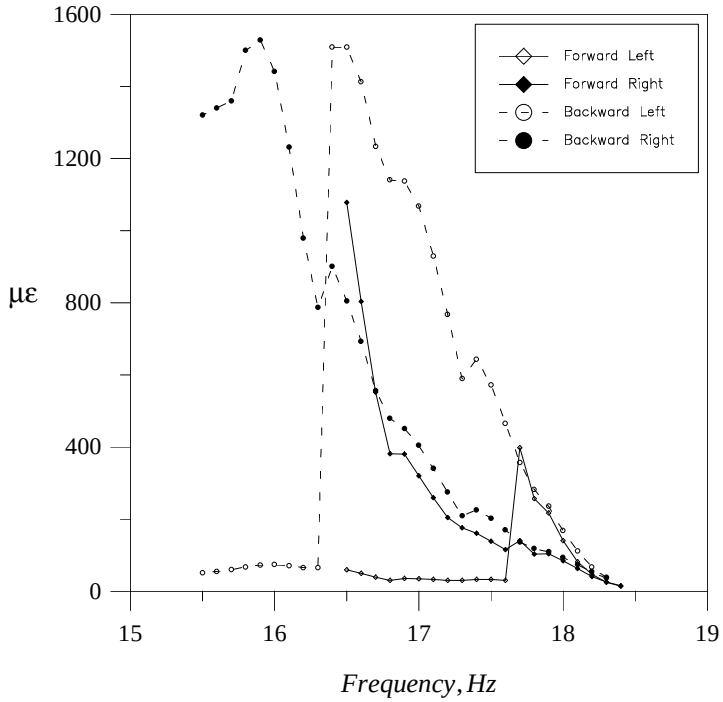

Figure 2.12: Frequency-response curves ($F = 3.2g$)

important to note here that the two tails were oscillating in an out-of-phase fashion. As we kept incrementing the frequency, the response amplitude of the two tails decreased until the oscillations disappeared. At this stage, we started sweeping in the backward direction, again with an increment of 0.1 Hz. As we kept decreasing the excitation frequency, oscillation amplitudes of the tails became larger and larger, with the left-tail amplitude being higher than that of the right tail. The tail oscillations are out of phase. At a frequency of 16.4 Hz, another jump occured and the right-tail response was larger than that of the left tail; the oscillations of the two tails were in-phase. As we reduced the excitation frequency another jump to the trivial response occured at a frequency of approximately 15.5 Hz. It is important to mention that in the frequency range 15.5 Hz to 16.4 Hz, two responses were possible: the trivial response and in-phase response. In the frequency range 16.4 Hz to 17.6 Hz: again two responses were observed: an in-phase and an out-of-phase motions.

Figure 2.13 shows another frequency-response curve but for an excitation amplitude of $2.75g$.

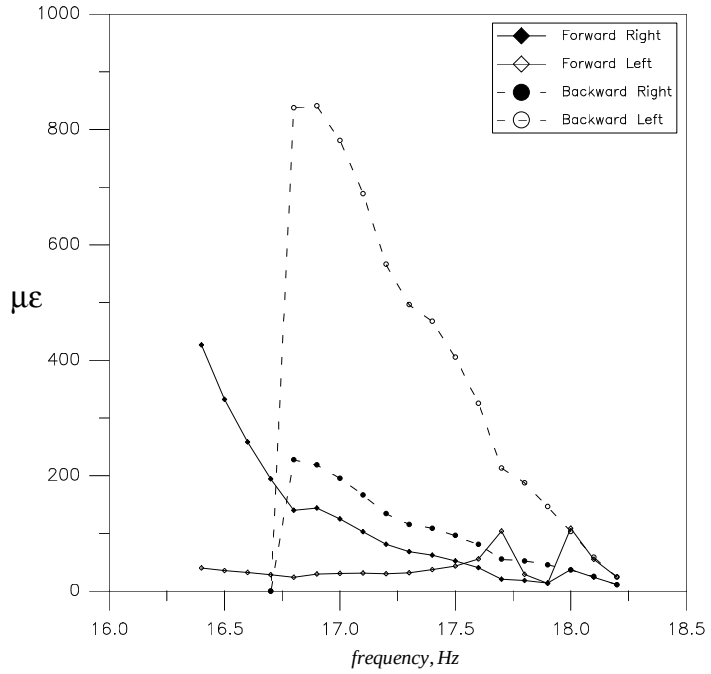

Figure 2.13: Frequency-response curve ($F = 2.75g$)

The main difference between this figure and Figure 2.12 is that, in the backward sweep, the responses of the left and right tails jumped down to the trivial motion at 16.7 Hz, which is even less than the beginning of the forward sweep. Of course, the oscillation amplitudes of the tails are less than those in Figure 2.12 because the excitation level is smaller. An interesting phenomenon occured while we were conducting the experiments. At an excitation frequency of 17.7 Hz, oscillation amplitude of the left tail jumped. This frequency corresponds to the same frequency at which the jump occured in the forward sweep in Figure 2.12. However, the oscillations of the two tails remained in-phase. As the excitation frequency was incremented, the left-tail oscillations jumped down. As the excitation frequency increased beyond 18 Hz, the left-tail response jumped up again and the oscillations of the two tails were out-of-phase, as in the previous case.

Another important branch of responses that we were able to follow is the one shown in Figure 2.14. Here the two tails oscillated in-phase in the region from 16.7 Hz to 17.7 Hz. The excitation amplitude for this curve is $2.75g$. This solution is different from those shown

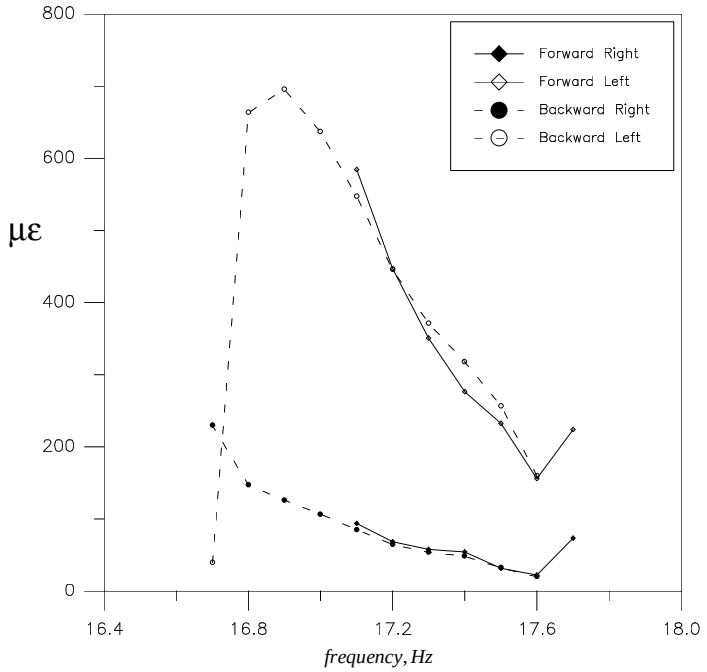

Figure 2.14: Frequency-response curve ($F = 2.75g$) for the in-phase response

in the previous figures. The forward sweep started at a frequency of 17.1 Hz and the response amplitudes of the two tails kept decreasing until the excitation frequency reached 17.7 Hz. Beyond this frequency, the response jumped to another response in which the motion of the left-tail was larger than that of the right tail, but the oscillations of the tails were out-of-phase, similar to the solutions in Figure 2.12. On the backward sweep, this in-phase motion kept increasing until the excitation frequency reached 16.8 Hz. At this frequency, the response jumped to a response in which the motion of the right tail was larger than that of the left tail with the two tails oscillating in-phase. We note that as the excitation amplitude was increased, the response amplitudes of the two tails increased, but the jump locations decreased.

At the end of this section, we note that the theoretically obtained frequency-response-curves are in agreement with those obtained experimentally. These curves will be described in detail, before and after applying control, in the next chapter.

2.8 Experimental Force-Response Curves

Several amplitude sweeps were done for all possible combination of responses. Two of these possible amplitude responses are shown in Figure 2.10. These amplitude sweeps were done for an excitation frequency of 18 Hz. We only show the forward sweeps. The backward sweeps follow their corresponding branches. In this plot, the response of the left tail is larger than that of the right tail in one case, and the response of the right tail is larger than the response of the left tail in the other case. One of the branches corresponds to an in-phase motion while the other one corresponds to an out-of-phase motion. As expected, as we increased the amplitude of oscillations, the response amplitudes of both tails increased.

We theoretically obtained several force-response curves. One of them is shown in Figure 2.11 where the frequency of excitation is 18 Hz. Solid lines are stable, while dashed lines are unstable. At this excitation frequency, two different responses were obtained, a response in the motion of the left tail is larger than that of the right tail and a response in which the motion of the right tail is larger than that of the left tail. If the excitation amplitude is less than $3g$, there is only one response in which oscillation amplitude of the right tail is larger than that of the left tail. Above $3g$, two different responses exist. Other force-response curves were produced at different excitation frequencies where the left-tail response is larger than that of the right tail.

Comparison between the experimental and theoretical response curve show that they are qualitatively similar in the number of existing modes and their locations. However, the experimental response is slightly shifted on the frequency axis. Also, the decaying response obtained theoretically is concave while that obtained experimentally is convex (exponential decay).

2.9 Summary

We used experimental data of a 1/16 structural dynamic scale model of the F-15 aircraft to develop a mathematical model of its twin-tail assembly. The model consists of two oscillators, each of which has linear and quadratic damping terms and a cubic nonlinear term. The two oscillators are coupled linearly. Experimental modal analysis was used to estimate their linear natural frequencies and damping ratios. The model was then excited by a principal parametric resonance (twice one of its natural frequencies). The force-response curves obtained experimentally were compared with those obtained with the method of multiple scales to estimate the nonlinear parameters as well as the linear coupling parameter. Finally, experimental and theoretical frequency-response and force-response curves were obtained. Description of the different responses was presented.

Chapter 3

Cubic Velocity Feedback

3.1 Introduction

Several researchers implemented active control techniques utilizing piezoelectric actuators. Also different control strategies were devised. However, the underlying concept behind all of these strategies is to add electronic damping and thus reduce the vibration level and hence extend the fatigue life of the tails. On the other hand, as it is well-known [61] in the case of parametric excitation, adding damping to the tails will not limit their oscillation amplitudes once a threshold excitation level is exceeded. In fact, adding damping to the tails will only increase the threshold. Consequently, adding damping is not a robust way of controlling the tail vibrations since at high angles of attack the tails are subjected to extremely high excitation levels.

For this reason, we used a nonlinear control law that was developed by Oueini *et al.* [62] to suppress the vibrations of parametrically excited systems. They fedback the cube of the velocity signal to suppress the first-mode vibrations of a cantilever beam. We extended their work by employing a controller for each tail and thus reduced the interaction between the two tails. The maximum response occurs when the excitation frequency is near twice the natural frequency of either of the vertical tails; that is, principal parametric resonance. Thus,

we used the control law to suppress the tail vibrations at that frequency.

3.2 Perturbation Solution

The response of the twin-tail assembly to a principal parametric excitation can be modeled by the following two mass normalized second-order coupled differential equations:

$$\ddot{u}_1 + \omega_1^2 u_1 + 2\epsilon\mu_1\dot{u}_1 + \epsilon\alpha_1 u_1^3 + \epsilon\mu_3\dot{u}_1 \mid \dot{u}_1 \mid -\epsilon k(u_2 - u_1) = \epsilon u_1\eta_1 F\cos(\Omega t + \tau_1) + T_1 \quad (3.1)$$

$$\ddot{u}_2 + \omega_2^2 u_2 + 2\epsilon\mu_2\dot{u}_2 + \epsilon\alpha_2 u_2^3 + \epsilon\mu_4\dot{u}_2 \mid \dot{u}_2 \mid -\epsilon k(u_1 - u_2) = \epsilon u_2\eta_2 F\cos(\Omega t + \tau_2) + T_2 \quad (3.2)$$

where T_1 and T_2 are the control forces. The parameters in equations (3.1) and (3.2) were identified in preceding chapter. We consider a control law given by $T_1 = -\epsilon G_1\dot{u}_1^3$ and $T_2 = -\epsilon G_2\dot{u}_2^3$, where G_1 and G_2 are positive constants.

We use the method of multiple scales [59] to generate a first-order approximate solution of equations (3.1) and (3.2) when $\Omega \approx 2\omega_1$ and $\omega_2 \approx \omega_1$. To this end, we seek a first-order uniform expansion of the solution in the form

$$u_1 = u_{11}(T_0, T_1) + \epsilon u_{12}(T_0, T_1) + \cdots \quad (3.3)$$

$$u_2 = u_{21}(T_0, T_1) + \epsilon u_{22}(T_0, T_1) + \cdots \quad (3.4)$$

where $T_0 = t$ is a fast time scale and $T_1 = \epsilon t$ is a slow time scale. In terms of T_0 and T_1, the time derivatives become

$$\frac{d}{dt} = D_0 + \epsilon D_1 + \cdots$$
$$\frac{d^2}{dt^2} = D_0^2 + 2\epsilon D_0 D_1 + \cdots \quad (3.5)$$

where $D_n = \frac{\partial}{\partial T_n}$. Substituting equations (3.3)–(3.5) into equations (3.1) and (3.2) and equating coefficients of like powers of ϵ yields

$O(\epsilon^0)$:

$$D_0^2 u_{11} + \omega_1^2 u_{11} = 0 \quad (3.6)$$

$$D_0^2 u_{21} + \omega_2^2 u_{21} = 0 \quad (3.7)$$

$O(\epsilon)$:

$$\begin{aligned} D_0^2 u_{12} + \omega_1^2 u_{12} = & -2D_0 D_1 u_{11} - 2\mu_1 D_0 u_{11} + \eta_1 k_1 (u_{21} - u_{11}) - \alpha_1 u_{11}^3 \\ & -\mu_3 D_0 u_{11} \mid D_0 u_{11} \mid + \eta_1 u_{11} F \cos(\Omega t + \tau_1) - G_1 (D_0 u_{11})^3 \end{aligned} \tag{3.8}$$

$$\begin{aligned} D_0^2 u_{22} + \omega_2^2 u_{22} = & -2D_0 D_1 u_{21} - 2\mu_2 D_0 u_{21} + \eta_2 k_2 (u_{11} - u_{21}) - \alpha_2 u_{21}^3 \\ & -\mu_4 D_0 u_{21} \mid D_0 u_{21} \mid + \eta_2 u_{21} F \cos(\Omega t + \tau_2) - G_2 (D_0 u_{21})^3 \end{aligned} \tag{3.9}$$

The general solutions of equations (3.6) and (3.7) can be written as

$$u_{11} = A_1(T_1) e^{i\omega_1 T_0} + \bar{A}_1(T_1) e^{-i\omega_1 T_0} \tag{3.10}$$

$$u_{21} = A_2(T_1) e^{i\omega_2 T_0} + \bar{A}_2(T_1) e^{-i\omega_2 T_0} \tag{3.11}$$

where the $A_i(T_1)$ are determined by eliminating the secular terms from the next-order approximation. Substituting equations (3.10) and (3.11) into equations (3.8) and (3.9) yields

$$\begin{aligned} D_0^2 u_{12} + \omega_1^2 u_{12} = & -2i\omega_1 A_1' e^{i\omega_1 T_0} - 2\mu_1 i\omega_1 A_1 e^{i\omega_1 T_0} + \eta_1 k (A_2 e^{i\omega_2 T_0} - A_1 e^{i\omega_1 T_0}) \\ & -\alpha_1 A_1^3 e^{3i\omega_1 T_0} - 3\alpha_1 A_1^2 \bar{A}_1 e^{i\omega_1 T_0} - \mu_3 [(i\omega_1 A_1 e^{i\omega_1 T_0}) | i\omega_1 A_1 e^{i\omega_1 T_0} |] \\ & + \frac{1}{2}\eta_1 F A_1 e^{i\left[(-\Omega+\omega_1)T_0 - \tau_1\right]} + \frac{1}{2}\eta_1 F A_1 e^{i\left[(\Omega+\omega_1)T_0 + \tau_1\right]}) \\ & -G_1 \Big[- i\omega_1^3 A_1^3 e^{3i\omega_1 T_0} + 3i\omega_1^3 A_1^2 \bar{A}_1 e^{i\omega_1 T_0} \Big] + cc \end{aligned} \tag{3.12}$$

$$\begin{aligned} D_0^2 u_{22} + \omega_2^2 u_{22} = & -2i\omega_2 A_2' e^{i\omega_2 T_0} - 2\mu_2 i\omega_2 A_2 e^{i\omega_2 T_0} + \eta_2 k (A_2 e^{i\omega_2 T_0} - A_2 e^{i\omega_2 T_0}) \\ & -\alpha_2 A_1^3 e^{3i\omega_2 T_0} - 3\alpha_2 A_2^2 \bar{A}_2 e^{i\omega_2 T_0} - \mu_4 [(i\omega_2 A_2 e^{i\omega_2 T_0}) | i\omega_2 A_2 e^{i\omega_2 T_0} |] \\ & + \frac{1}{2}\eta_2 F A_2 e^{i\left[(-\Omega+\omega_2)T_0 - \tau_2\right]} + \frac{1}{2}\eta_2 F A_2 e^{i\left[(\Omega+\omega_2)T_0 + \tau_2\right]}) \\ & -G_2 \Big[- i\omega_2^3 A_2^3 e^{3i\omega_2 T_0} + 3i\omega_2^3 A_2^2 \bar{A}_2 e^{i\omega_2 T_0} \Big] + cc \end{aligned} \tag{3.13}$$

Eliminating the terms that produce secular terms in equations (3.12) and (3.13) gives

$$\begin{aligned} 2i\omega_1 A_1' + 2\mu_1 i\omega_1 A_1 = & \eta_1 k A_2 e^{i\sigma_2 T_1} - \eta_1 k A_1 - 3\alpha_1 A_1^2 \bar{A}_1 \\ & + \frac{1}{2}\eta_1 F(\bar{A}_1) e^{i(\sigma_1 T_1 + \tau_1)} - i\frac{4}{3\pi}\mu_3 \omega_1^2 a_1^2 e^{i\beta_1} - 3G_1 i\omega_1^3 A_1^2 \bar{A}_1 \end{aligned} \tag{3.14}$$

$$\begin{aligned} 2i\omega_2 A_2' + 2\mu_2 i\omega_2 A_2 = & \eta_2 k A_1 e^{-i\sigma_2 T_1} - \eta_2 k A_2 - 3\alpha_2 A_2^2 \bar{A}_2 \\ & + \frac{1}{2}\eta_2 F(\bar{A}_2) e^{i(\sigma_1 T_1 - 2\sigma_2 T_1 + \tau_2)} - i\frac{4}{3\pi}\mu_4 \omega_2^2 a_2^2 e^{i\beta_2} - 3G_2 i\omega_2^3 A_2^2 \bar{A}_2 \end{aligned} \tag{3.15}$$

Rewriting the A_n in terms of polar coordinates as

$$A_n = \frac{1}{2} a_n e^{i\beta_n} \tag{3.16}$$

and separating real and imaginary parts in equations (3.14) and (3.15), we obtain

$$\begin{aligned}
a_1' &= -\mu_1 a_1 + \frac{\eta_1 F a_1}{4\omega_1}\sin\gamma_2 - \frac{4\mu_3\omega_1}{3\pi}a_1^2 + \frac{\eta_1 k a_2}{2\omega_1}\sin\gamma_1 - \frac{3}{8}G_1\omega_1^2 a_1^3 && (3.17)\\
a_2' &= -\mu_2 a_2 + \frac{\eta_2 k a_1}{2\omega_2}\sin\gamma_1 - \frac{4\mu_4\omega_2}{3\pi}a_2^2 - \frac{\eta_2 F a_2}{4\omega_2}\sin\tau_1 - \tau_2 + 2\gamma_1 - \gamma_2 - \frac{3}{8}G_2\omega_2^2 a_2^3 && (3.18)\\
\gamma_1' &= -\frac{\eta_1 k}{2\omega_1} + \frac{\eta_2 k}{2\omega_2} + \sigma_2 - \frac{\eta_2 F}{4\omega_2}\cos(\tau_1 - \tau_2 + 2\gamma_1 - \gamma_2) + \frac{\eta_1 F}{4\omega_1}\cos\gamma_2 \\
&\quad -\frac{3\alpha_1}{8\omega_1}a_1^2 - \frac{\eta_2 k a_1}{2a_2\omega_2}\cos\gamma_1 + \frac{\eta_1 k a_2}{2a_1\omega_1}\cos\gamma_1 + \frac{3\alpha_2}{8\omega_2}a_2^2 && (3.19)\\
\gamma_2' &= -\frac{\eta_1 k}{\omega_1} + \sigma_1 + \frac{\eta_1 F}{2\omega_1}\cos\gamma_2 - \frac{3\alpha_1}{4\omega_1}a_1^2 + \frac{\eta_1 k a_2}{a_1\omega_1}\cos\gamma_1 && (3.20)
\end{aligned}$$

where

$$\begin{aligned}
\gamma_1 &= \sigma_2 T_1 - \beta_1 + \beta_2 \\
\gamma_2 &= \sigma_1 T_1 - 2\beta_1 + \tau_1 && (3.21)
\end{aligned}$$

Rewriting the A_k in terms of Cartesian coordinates

$$A_k = \frac{1}{2}[p_k(T_1) - iq_k(T_1)]e^{(i\nu_k T_1 + \frac{1}{2}\tau_k)}, \qquad k = 1, 2 \tag{3.22}$$

where

$$\begin{aligned}
\nu_1 = \beta_1' &= \frac{1}{2}\sigma_1 \\
\nu_2 = \beta_2' &= \frac{1}{2}\sigma_1 - \sigma_2 && (3.23)
\end{aligned}$$

and separating equations (3.14) and (3.15) into real and imaginary parts, we obtain the modulation equations

$$\begin{aligned}
p_1' =& -\nu_1 q_1 - \mu_1 p_1 - \frac{1}{2\omega_1}\eta_1 k q_2 + \frac{1}{2\omega_1}\eta_1 k q_1 + \frac{3}{8\omega_1}\alpha_1 p_1^2 q_1 \\
&+\frac{3}{8\omega_1}\alpha_1 q_1^3 + \frac{\eta_1 F}{4\omega_1}q_1 - \frac{4}{3\pi}\mu_3\omega_1\sqrt{p_1^2 + q_1^2}\,p_1 - \frac{3}{8}G_1\omega_1^2(p_1^3 + p_1 q_1^2) && (3.24)
\end{aligned}$$

$$
\begin{aligned}
q_1' =& \nu_1 p_1 - \mu_1 q_1 + \frac{1}{2\omega_1}\eta_1 k p_2 - \frac{1}{2\omega_1}\eta_1 k p_1 - \frac{3}{8\omega_1}\alpha_1 p_1^3 \\
& - \frac{3}{8\omega_1}\alpha_1 p_1 q_1^2 + \frac{\eta_1 F}{4\omega_1} p_1 - \frac{4}{3\pi}\mu_3 \omega_1 \sqrt{p_1^2 + q_1^2}\, q_1 - \frac{3}{8} G_1 \omega_1^2 (p_1^2 q_1 + q_1^3) \qquad (3.25) \\
p_2' =& -\nu_2 q_2 - \mu_2 p_2 - \frac{1}{2\omega_2}\eta_2 k q_1 + \frac{1}{2\omega_2}\eta_2 k q_2 + \frac{3}{8\omega_2}\alpha_2 p_2^2 q_2 \\
& + \frac{3}{8\omega_2}\alpha_2 q_2^3 + \frac{\eta_2 F}{4\omega_2} q_2 - \frac{4}{3\pi}\mu_4 \omega_2 \sqrt{p_2^2 + q_2^2}\, p_2 - \frac{3}{8} G_2 \omega_2^2 (p_2^3 + p_2 q_2^2) \qquad (3.26) \\
q_2' =& \nu_2 p_2 - \mu_2 q_2 + \frac{1}{2\omega_2}\eta_2 k p_1 - \frac{1}{2\omega_2}\eta_2 k p_2 - \frac{3}{8\omega_2}\alpha_2 p_2^3 \\
& - \frac{3}{8\omega_2}\alpha_2 p_2 q_2^2 + \frac{\eta_2 F}{4\omega_2} p_2 - \frac{4}{3\pi}\mu_4 \omega_2 \sqrt{p_2^2 + q_2^2}\, q_2 - \frac{3}{8} G_2 \omega_2^2 (p_2^2 q_2 + q_2^3) \qquad (3.27)
\end{aligned}
$$

The performance of the control is evaluated by calculating the equilibrium solutions of equations (3.24)–(3.27) and examining their stability as a function of the parameters F, σ_1, and G_i. We set the time derivatives in equations (3.24)–(3.27) equal to zero and solved the resulting system of algebraic equations for p_1, q_1, p_2, and q_2 for a specified value of either σ_1, which is a measure of the detuning of the principal parametric resonance, or F, which is a measure of the forcing amplitude. The amplitudes a_1 and a_2 of the responses of the two tails were then calculated from $a_i = \sqrt{p_i^2 + q_i^2}$. Since there is no closed-form solution for the four algebraic equations, we resorted to numerical techniques. Numerical integration of the modulation equations for different sets of initial conditions was used to locate some of the possible solutions for a given σ_1 and F. Then, starting with these solutions, we used a pseudo arclength scheme [60] to trace the branches of the equilibrium solutions by varying either σ_1 or F.

The stability of a particular equilibrium solution was determined by examining the eigenvalues of the Jacobian matrix of the right-hand sides of equations (3.24)–(3.27). If the real part of each eigenvalue is negative, the corresponding equilibrium solution is asymptotically stable. If the real part of any of the eigenvalues is positive, the corresponding equilibrium solution is unstable. In the next two sections, we performed the stability analysis and evaluated the control law.

3.3 Theoretical Force-Response Curves

In Figure 3.1, we show typical open- and closed-loop force-response curves. First, we consider the open-loop response. When $F < 2.5\ g$, only the trivial solution exists. In the absence of large disturbances, it is maintained as F is increased. When F reaches $3.55\ g$, the trivial solution loses stability through a subcritical pitchfork bifurcation, and the response amplitude jumps up to the high-amplitude responses in curves (a). A further increase in F leads to a higher response amplitude of the left tail and a lower response amplitude of the right tail. When F is decreased, the response undergoes a saddle-node bifurcation, and the left-tail response jumps down to either another low-amplitude response or the trivial solution. In this region, again the right-tail response amplitude either (a) remains constant (but the phase between the oscillations of the two tails changes) or (b) drops to the trivial solution, depending on the disturbance level.

Second, we consider the response of the closed-loop response. When $G_1 = G_2 = G = 0.01$, the response curves are similar to the uncontrolled response curves. The bifurcations are identical, however, the location of the saddle-node bifurcation is shifted in the case of the right tail and one solution is completely eliminated. On the other hand, for the left tail, the jump-up and jump-down due to the saddle-node bifurcations are eliminated, as shown in curves (b). As the controller gain is further increased, the saddle-node and subcritical pitchfork bifurcations are replaced with one supercritical pitchfork bifurcation at $F = 3.5g$. Additionally, the amplitude of the response is further reduced.

3.4 Theoretical Frequency-Response Curves

In Figure 3.2, we show typical frequency-response curves of the open- and closed-loop system for both the right and left tails. The response amplitudes depend on the value of σ_1 and the system's initial conditions. The solid lines correspond to stable solutions, while the dashed lines correspond to unstable solutions. All of the bifurcations are saddle-node and pitchfork

bifurcations. The latter are approximately at the frequencies 19.0 Hz and 21.6 Hz.

We consider first the open-loop response (curves (a) in Figure 3.2 (i-ii)). The left-tail response is larger than that of the right tail in the frequency range 18.5 till 21.6 Hz. In the frequency range 18.5 Hz till 19.8 Hz, there is another solution where the left-tail response is again larger than the right-tail response. A third solution exists in the frequency range 17.4 Hz to 18.6 Hz where the right-tail response is larger than that of the left tail. We note that the trivial solution loses stability at an excitation frequency of 19.0 Hz through a subcritical pitchfork bifurcation in the forward sweep and at 21.6 Hz in the reverse sweep through a supercritical pitchfork bifurcation.

Next, we consider the response of the closed-loop system. Curves (b-e) show the responses of both the right and left tails as the controller gain is increased. It is clear that, as the controller gain increases, the response amplitudes of the tails decrease. Also, the bandwidth where the different responses occur decreases. For example, in curve(e), the different coexisting responses in the frequency range 17.3 Hz to 19 Hz are completely eliminated. Also, all of the dangerous subcritical bifurcations are changed to safe supercritical bifurcations and hence the jumps are eliminated.

3.5 Experiments

The theoretical analysis was verified by implementing the control strategy on the twin-tail assembly fitted with piezoceramic actuators and strain gages. The assembly was excited vertically, thereby subjecting the first modes of the twin tails to a principal parametric resonance.

3.5.1 Setup and Procedure

The tail deflections were measured with a series of four strain gages. The centers of the gage pairs were 0.9 *cm* and 8.5 *cm* from the top of the aluminum channels. One pair was on the

outside of the right vertical tail; the other pair was on the outside of the left vertical tail. The strain gages were aligned to measure bending moment. Changes in the gages were measured with a strain-gage conditioning amplifier, in a quarter bridge configuration. The actuators used were two patches of the piezoelectric material lead-zirconate-titanate. One patch was installed near the root of each tail. The dimensions of the patches used were $7 \times 3.5 \times .019$ cm.

A series of bolts and several positioning blocks fixed the model to a 250-lb shaker. The shaker excitation was measured with an accelerometer studded to the base. The accelerometer signal was conditioned with an amplifier. The shaker amplifier was driven with a signal generator. The strain-gage signal from the conditioner was fed to the controllers, and the nonlinear control signal was generated, amplified, and sent to the actuators. The responses of the tails and the circuit and the accelerometer signals were monitored using a four-channel signal analyzer and an oscilloscope and collected by a data acquisition computer software. Figure 3.3 shows the experimental setup.

3.5.2 Controller Circuit

A hardware controller circuit was built and used with a low-pass filter to generate the cubic velocity signal out of the strain-gage signal. The essential components of the circuit included operational amplifiers (op-amps), two analog multipliers, and other miscellaneous hardware components. The op-amps were used only as buffers between the input, output signals, and the circuit and thus isolate the circuit from the other high-power components. The analog multipliers were utilized to generate the nonlinear term. A chip was connected to perform high-precision (0.1% typical error) 4-quadrant voltage multiplication according to the following relationship:

$$v_{out} = \frac{v_1 - v_2}{v_3 - v_4} \tag{3.28}$$

where v_{out} is the output voltage of the multiplier and the v_i are the input voltages. Four multipliers were dedicated to the circuit, two for each tail. The remaining circuit components included high-precision potentiometers, metal film resistors, and polystyrene capacitors.

3.5.3 Location of the actuators

The goal was to maximize the control authority that can be generated by the actuator; in our case, it is equivelant to maximizing the resultant forces that the actuator develops. Ideally, more actuators would be placed in the areas of high strain than in areas of low strain. To determine these locations, we glued two strain gages to each tail: one gage at the root and the other at the middle of the tail. Under parametric excitation, we realized that the largest modal response measured by the gage was at the root. Thus we decided to locate the actuators there. It is expected that placing the actuator at any location would stiffen that area and thus reduce the effectiveness of the actuator. However, in our case this was not a problem because the actuator thickness was 1.9 mm. This was confirmed by comparing the force- and frequency-response curves before and after attaching the PZT to the tails. These curves showed that the tail dynamics did not change much. For a full-scale fighter tail under buffet loads, the actuator placement should be optimized for high performance. A good example of such an analysis can be found in reference [46].

3.6 Experimental Frequency-Response Curves

We forced the twin-tail assembly at 3.1 g and conducted forward and reverse frequency sweeps. The acceleration of the shaker head was monitored, and the input voltage driving the shaker head was adjusted to maintain a constant forcing amplitude. In Figures 3.4 and 3.5, we exhibit the open- and closed-loop frequency-response curves for the right and left tails for both the in-phase and out-of-phase responses.

First, we present the open-loop case. Initially, as the forcing frequency was increased, the amplitude remained at zero. When the frequency reached a value close to 19.0 Hz for the in-phase response case and 17.6 Hz for the out-of-phase case, the response jumped up (a subcritical pitchfork bifurcation). We note that, for the in-phase response, the left-tail response is greater than that of the right tail, while for the case of the out-of-phase response, the right tail response is greater than that of the left tail. Further increases in

the excitation frequency lead to a decrease in the amplitudes. When the frequency was approximately 19.5 Hz, the tails stopped oscillating (a supercritical pitchfork bifurcation). Thus, the response remained at zero. In the reverse sweep, the response was similar to that observed during the forward sweep. However, the response amplitude did not experience a jump down at 19.0 Hz in the case of the in-phase response. Instead, a growth rate was observed, leading to a very high response amplitude. A jump down to zero occured at 18.5 Hz (a saddle-node bifurcation). For the case of the out-of-phase response, the forward and reverse sweeps were almost similar except that the jump down of the left-tail response occured at a frequency of 18.5 Hz instead of 19.0 Hz, thereby experiencing a large-amplitude response before undergoing a saddle-node bifurcation and jumping down to the trivial response.

Second, we present the in-phase and out-of-phase frequency-response curves in the closed-loop case . As the frequency was increased, the response remained at zero until the point of subcritical bifurcation where the gain of the controller had to be increased to drive the response to zero. During the reverse sweep, the response amplitude traced the same curve generated during the closed-loop forward sweep. Thus the control law did its job. In fact, we performed another sweep starting with a higher gain and attained a zero-response during the entire sweep.

3.7 Experimental Force-Response Curves

We forced the twin-tail assembly at a constant frequency of 18.6 Hz and conducted forward and reverse sweeps for both the in-phase and out-of-phase responses. From the experiments, the forward and backward sweeps show similar trends, and thus we only show the forward sweeps in Figure 3.6.

First, we describe the open-loop response. As the force was increased, the tails did not oscillate initially. When the forcing amplitude reached approximately 2.85 g in the in-phase case and 2.82 g in the out-of-phase case, the response experienced a jump (a subcritical pitchfork bifurcation) to a high-amplitude response. Further increases in the forcing amplitude lead

to an increase in the response. We note that, at this frequency of excitation, the right-tail response is larger than that of the left tail and vice-versa, depending on the initial condition (the way we pluck the tails).

Second, we examine the closed-loop response. The gains of the controller circuit were chosen to ensure a trivial response of the tails at all excitation levels.

In order to examine the transient characteristics of the control law, we subjected the tails to a forcing level of 3 g and applied control to the worst case scenario of both tails; that is, the right tail was excited at 17.5 Hz and left tail was excited at 18.5 Hz. Figure 3.7 illustrates the two time traces for $G_1 = 1$ and $G_2 = 5G_1$. Clearly, increasing the feedback gain resulted in a better transient performance.

3.8 Summary

A nonlinear control law based on cubic velocity feedback was used to suppress the vibrations of the first bending mode of the twin tails. The method of multiple scales was used to derive four first-order differential equations governing the amplitudes and phases of the response. Then a bifurcation analysis was conducted to examine the stability of the closed-loop system and to investigate the performance of the controller and the effect of the feedback gain on the response. Due to the feedback control law, we found that all of the subcritical pitchfork bifurcations were replaced by safe supercritical ones. The bandwidth of nontrivial responses was reduced, thereby reducing the range of frequencies for which the tails oscillations are high. Also, the oscillation amplitudes of the tails decreased with increasing the gain of the feedback control law. Also, increasing the gain improved the transient performance. To verify the theoretical analysis, we conducted experiments on the structural model of the twin-tail assembly fitted with piezoceramic actuators and used an electronic circuit to generate the cubic velocity feedback signal. Good agreement between theory and experiments was realized.

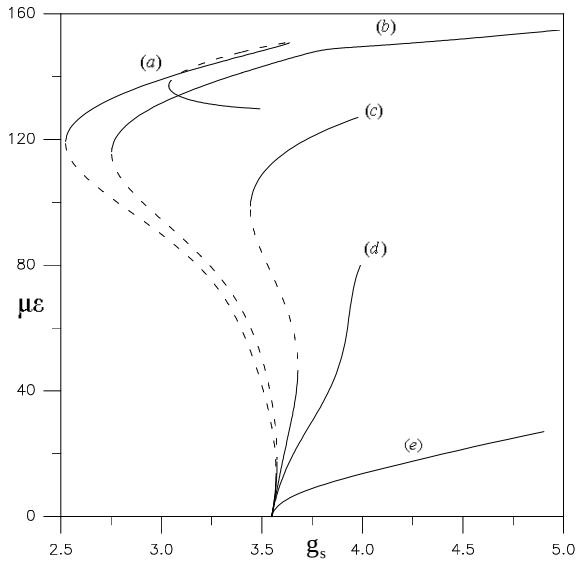

(i) right tail

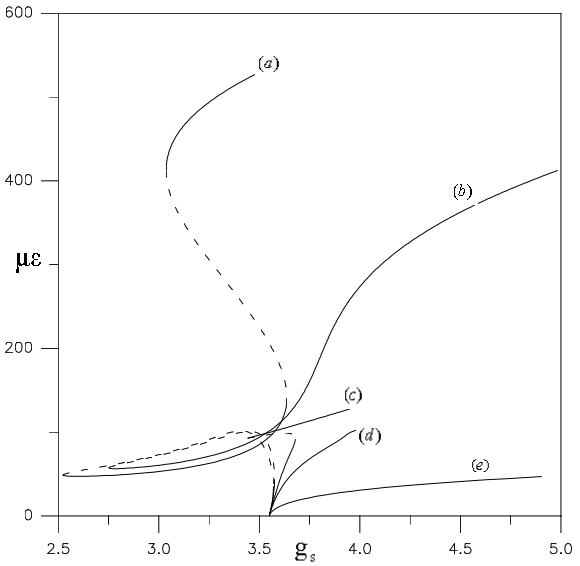

(ii) left tail

Figure 3.1: Effect of varying the feedback gain on the force-response curves of the specified tail (freq=18 Hz): a) G=0, b) G=0.01, c) G=0.05, d) G=0.1, and e) G=1

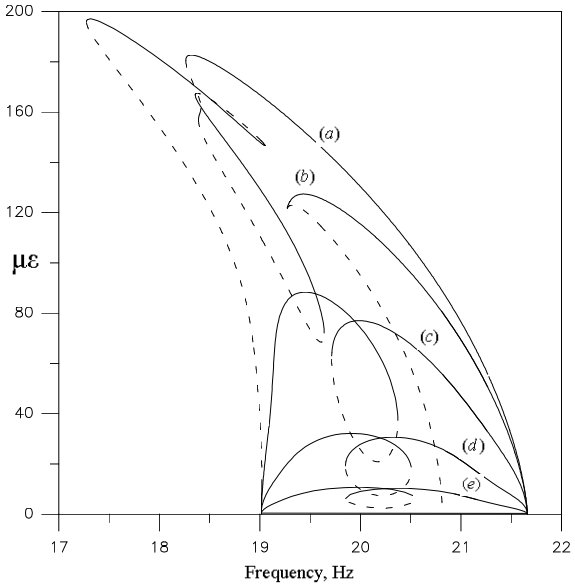

(i) right tail

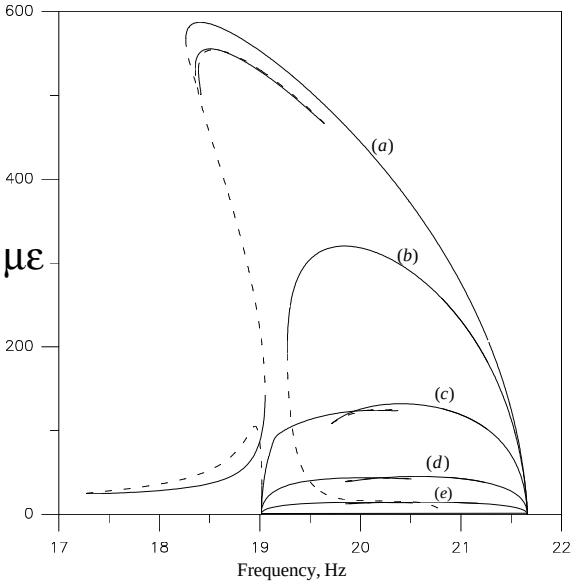

(ii) left tail

Figure 3.2: Effect of varying the feedback gain on the frequency-response curves of the specified tail ($F = 3.2g$): a) G=0, b) G=0.01, c) G=0.1, d) G=1, and e) G=10

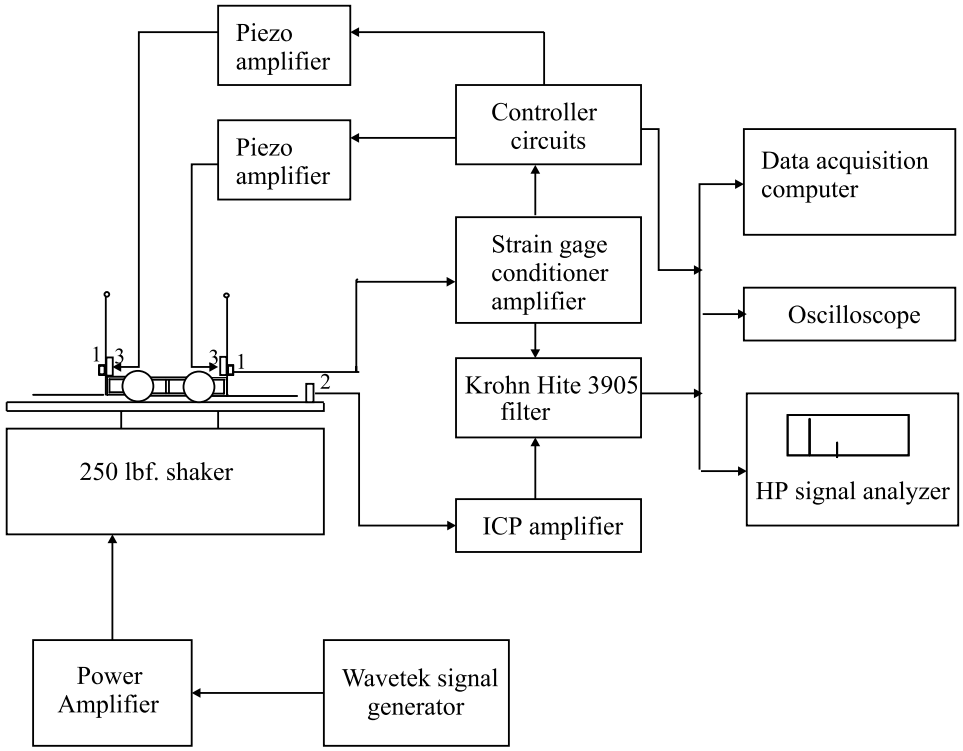

1: Strain gage
2: Accelerometer
3: PZT single sheet

Figure 3.3: Experimental Setup

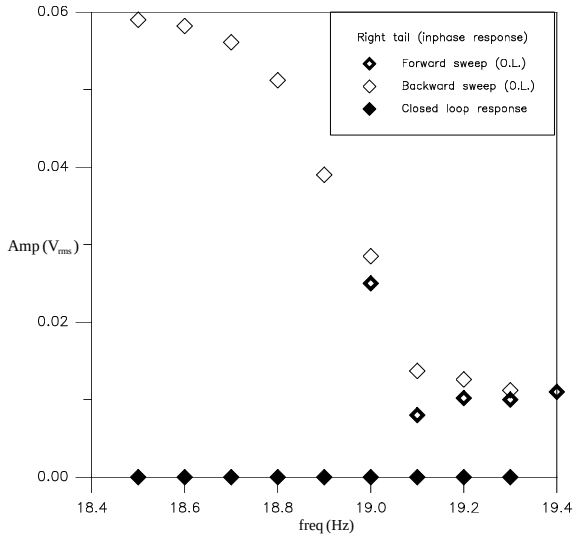

(i) right tail

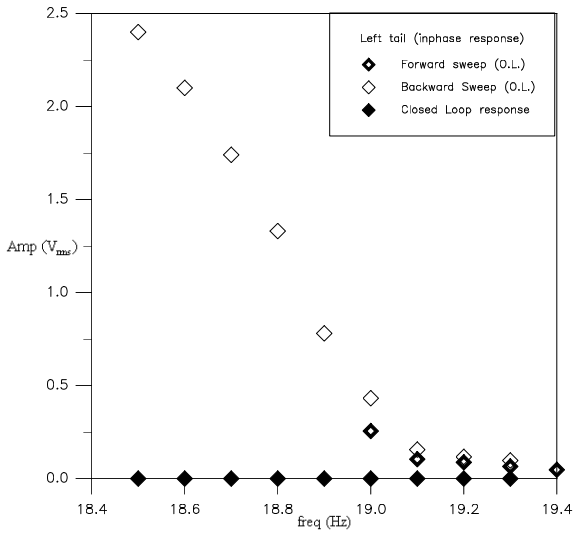

(ii) left tail

Figure 3.4: Frequency-response curves of the in-phase responses before and after control

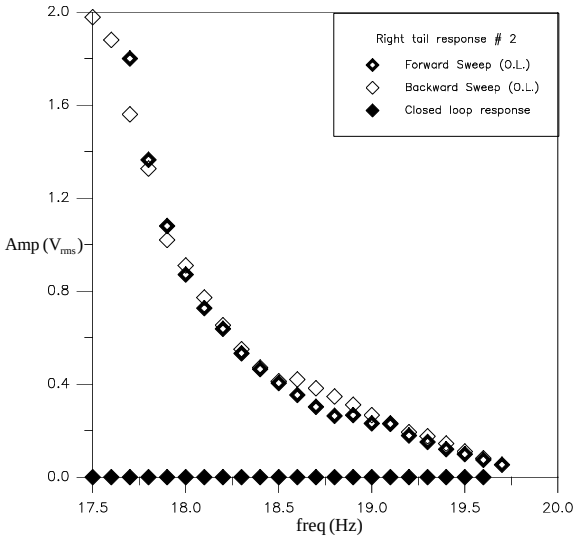

(i) right tail

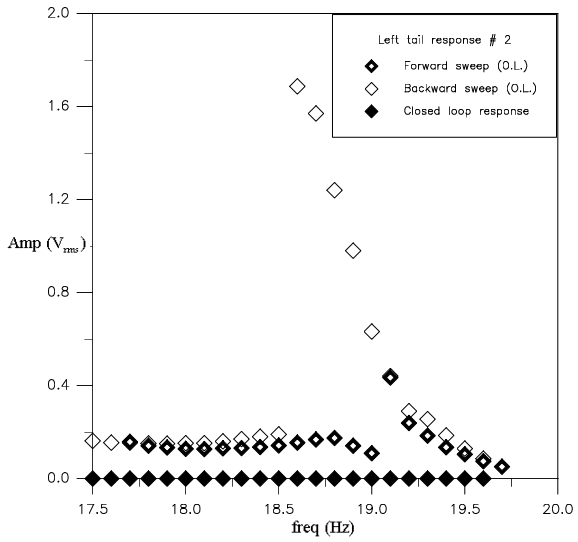

(ii) left tail

Figure 3.5: Frequency-response curves of the out-of-phase responses before and after control

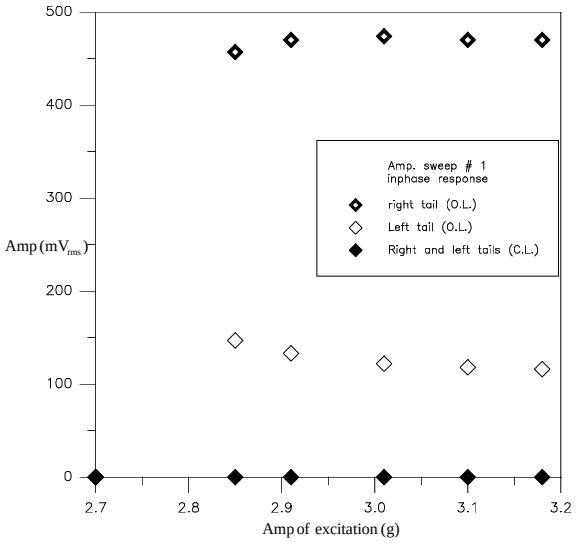

(i) inphase responses

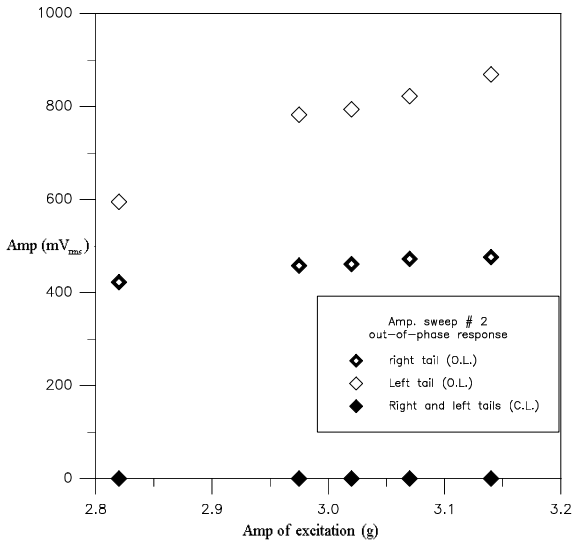

(ii) out-of-phase responses

Figure 3.6: Force-response curves of the tails before and after control

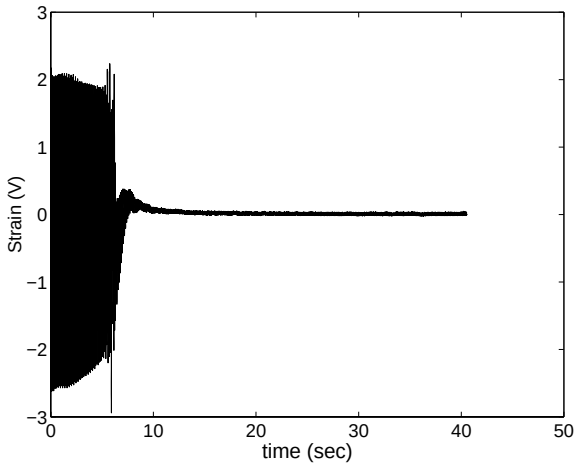

(i) right tail

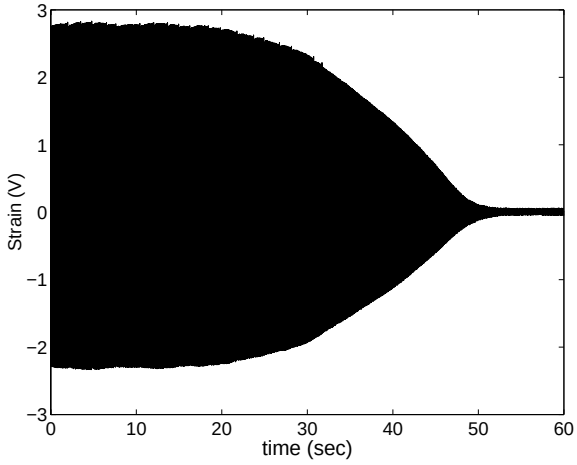

(ii) left tail

Figure 3.7: Time histories of the responses of the tails before and after applying control for different control gains (a) $G_2 = 5G_1$, and (b) $G_1 = 1$

Chapter 4

Neural Network Identification and Control

4.1 Introduction

In aeroelastic investigations of aircraft, the structural behavior of aircraft components is assumed to be linear [2]. However, in reality nonlinearities are present in one form or another. It is always important to develop and verify several techniques to predict flight-vehicle dynamic and aeroelastic behavior to prevent vibration damage and aeroelastic instabilities. One of the available techniques that can be used to solve critical structural problems on fixed-wing aerospace vehicles is neural networks. During the past several years, neural networks have emerged as one of the most active areas in system identification and control of nonlinear systems. Also, neural networks are becoming more and more popular for a variety of applications, including electronics, dynamic modeling of chemical process systems, speech recognition, telecommunications, and transportation. Lisboa [63] summarizes some of the widespread use of neural networks. The reason for the wide variety of applications of neural networks in almost all fields of study is their usefulness in avoiding the complexity involved in directly modeling the system dynamics.

Another interesting application for neural networks is active vibration control of smart structures. The design of controllers to suppress vibrations in smart structures is a challenging problem due to the presence of nonlinearities in the structures and the actuators as well as the limited availability of control forces. One of the main objectives is to deal with imprecise mathematical models due to unmodeled dynamics and hence remove the requirement of having an exact detailed mathematical model for the system, which can be a very time-consuming process. This is where the power of neural networks is stressed; it can identify the system using the true input/output data without any prior model information.

There are several types of neural networks that have evolved over the last decade and half of them have proven to be efficient tools in identifying nonlinear systems. Some of these are Volterra series models, group method of data handling models (GMDH), self-organizing neural networks, and radial basis functions (RBN) [64, 65, 66, 67]. Also, it has been shown that multi-layer perceptrons (MLPs) are universal function approximators [68]. Later this model type has been used to train neurocontrollers to suppress the vibrations of nonlinear smart structures. The linear and nonlinear mapping properties of neural networks have been extensively utilized in the design of multi-layered feedforward neural networks for the implementation of control algorithms [69, 70].

The vibration controller used in this paper is similar to the indirect linear model following control (LMFC) system [71, 72]. It is also similar to the backpropagation-through-time neural controller (BTTNC), which is presented by Chen *et al.* [73]. The BTTNC was used in the active control of structures under strong dynamic loadings. To train the neurocontroller, one needs the difference between the network output and the ideal input to the plant. Since nothing is known about the ideal input, the necessary data must be provided in a different way. It is possible to model the plant by a neural net. After finding an appropriate model, one can train the controller network by backpropagating the error through the plant model. Thus, the present study consists of two steps. First, a model of the plant was trained. After achieving a well performing plant model, we fixed its weights. Second, the plant was replaced by its model. The cascade of both networks was then used to train the neurocontroller.

Only the controller network weights were updated. Here, the overall system is tested and the performance of the network is discussed.

4.2 Backpropagation Neural Network

A prerequisite of the system identification task is to acquire as much information about the plant behavior as possible using input signals that excite the relevant dynamic processes of the structure under consideration. In addition, the signal amplitude has to cover the stationary operating range of interest. In this chapter, we use the backpropagation algorithm to train both the emulator and the controller multilayer perceptron (MLP)networks. An input to the network generates some output; then, the error between the desired output and the network output is used in the backpropagation learning algorithm. Each neuron in the network receives its own error factor and adjusts its weights accordingly. This training process continues until a desirable level of performance is reached. This can be done by specifying the sum-squared error between the network output and the desired target output. That is, the network seeks to minimize the following cost function:

$$E = \sum_{i=1}^{n} (d_i - y_i)^2 \tag{4.1}$$

where d_i is the target output, y_i is the neural network output, and n is the number of input-output training pairs. These forward and backward sweeps are continued until a desirable level of performance is reached. After the network has been sufficiently trained, only the feedforward paths are used. Illustrative examples of the backpropagation algorithm can be found in [51].

4.3 Mathematical Model of the Twin Tails

The problem at hand is to suppress the vibrations of a structural dynamic model (1/16 dynamically scaled) of the twin tails of the F-15 fighter. Figure 2.1 presents a three-dimensional

view of the tail section used to acquire the training and validation data sets and to verify the on-line predictive control scheme.

The equations governing the dynamics of the twin tails are reproduced here for convenience:

$$\begin{aligned} &\ddot{u}_1 + \omega_1^2 u_1 + 2\epsilon\mu_1\dot{u}_1 + \epsilon\alpha_1 u_1^3 + \epsilon\mu_3\dot{u}_1 \mid \dot{u}_1 \mid -\epsilon k(u_2 - u_1) \\ &\quad - \epsilon u_1\eta_1 F\cos(\Omega t + \tau_1) + Kf_1 = 0 \qquad (4.2) \\ &\ddot{u}_2 + \omega_2^2 u_2 + 2\epsilon\mu_2\dot{u}_2 + \epsilon\alpha_2 u_2^3 + \epsilon\mu_4\dot{u}_2 \mid \dot{u}_2 \mid -\epsilon k(u_1 - u_2) \\ &\quad - \epsilon u_2\eta_2 F\cos(\Omega t + \tau_2) + Kf_2 = 0 \qquad (4.3) \end{aligned}$$

where K is a proportionality constant (between volts and $\mu\epsilon$, measured experimentally), and f_1 and f_2 are the control action forces. Having this model facilitated the design of the neural networks for the identification and the control of the system since, instead of collecting real data from an experiment, we used this mathematical model to provide the necessary data for network training purposes.

These two second-order differential equations were transformed into a set of four first-order differential equations so as to make use of the available numerical routines that are specifically used for first-order systems. To this end, we let $x_1(t) = u_1(t)$, $x_2(t) = \dot{u}_1(t)$, $x_3(t) = u_2(t)$ and $x_4(t) = \dot{u}_2(t)$, and thus rewrite equations (4.2) and (4.3) in the following alternate form:

$$\dot{x}(t) = A(t)\,x(t) + n(t) \qquad (4.4)$$

$$y(t) = Cx(t) \qquad (4.5)$$

where

$$\dot{x}(t) = \begin{bmatrix} \dot{x}_1 & \dot{x}_2 & \dot{x}_3 & \dot{x}_4 \end{bmatrix}^T \qquad (4.6)$$

$$A(t) = \begin{bmatrix} 0 & 1 & 0 & 0 \\ -\omega_1^2 - \epsilon\eta_1 k + \epsilon\eta_1 F\cos(\Omega t + \tau_1) & -2\epsilon\mu_1 & \epsilon\eta_1 k & 0 \\ 0 & 0 & 0 & 1 \\ \epsilon\eta_2 k & 0 & -\omega_2^2 - \epsilon\eta_2 k + \epsilon\eta_2 F\cos(\Omega t + \tau_2) & -2\epsilon\mu_2 \end{bmatrix} \qquad (4.7)$$

$$n(t) = \begin{bmatrix} 0 & -\epsilon\alpha_1 x_1^3 - \epsilon\mu_3 x_2 \mid x_2 \mid & 0 & -\epsilon\alpha_2 x_3^3 - \epsilon\mu_4 x_4 \mid x_4 \mid \end{bmatrix}^T \qquad (4.8)$$

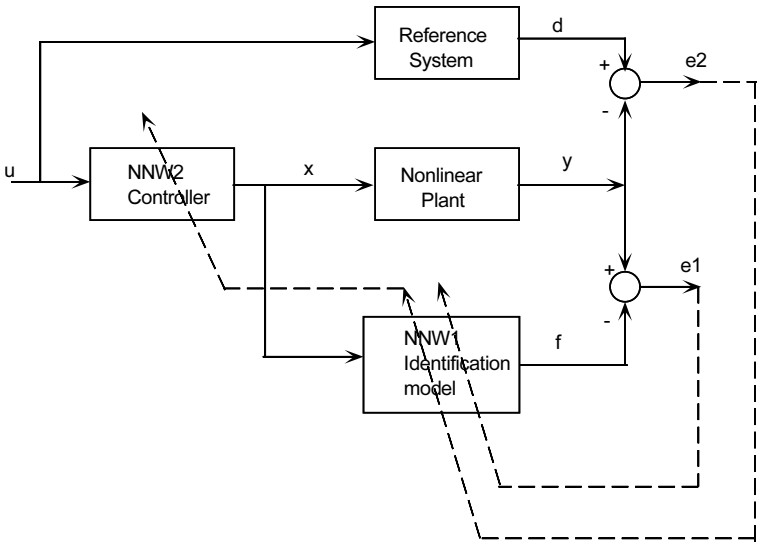

Figure 4.1: Flowchart

It is very important to be able to discretize the system for simulation purposes; thus, a discretization scheme representing a zero-order-hold (ZOH) [74] using the Euler formula (forward rule) was first tried. Also, a bilinear transformation (Tustin) scheme [74] was also tried. Both schemes are considered to be very crude and require a very fast sampling frequency. Finally, a Runge-Kutta integration scheme was used with the period T of integration being specified. In this study, the data sampling period as well as the period T of integration were chosen to be $T = 0.001$ sec. The state vector was updated after every step of integration. The input to the system is f_1 and f_2 and the output is the strain. After discretization of the system, the governing differential equations can be rewritten as difference equations; that is,

$$x(k+1) = \Phi(k)x(k) + n(k) \tag{4.9}$$

$$y(k) = Cx(k) \tag{4.10}$$

4.4 Emulator Neural Network

To suppress vibrations using a neurocontroller, we had to train an emulator neural network first. The emulator learns to predict the response of the tails given the actuation forces. Thus, the emulator can be considered as representing the transfer function from the actuator signal to the sensor reading. This transfer function includes the nonlinear response of the tails as well as the effect of the actuator dynamics in the control loop. The emulator learns this relationship between the input and the output from the past history of the response given the actuation forces. The output $y(k)$ of the plant is a function of the input forcing function $f(k)$. Thus, the neural net requires $f(k)$ to be an input to the network. We chose to have an $f(k)$ as well as two delayed versions of it as inputs to the emulator network. Also, as may be seen from the equations describing the system, the nonlinear plant is of second order. To increase the accuracy of the emulator network, we also fedback the output of the network as inputs to the network; that is, $y(k-1)$ and $y(k-2)$. The emulator was chosen to have two hidden layers. The input layer consisted of five units, which was found to be sufficient for a good model. The output layer had one unit that represented the current strain in the tail. Thus a 5-5-1 MLP was used. Figure 4.1 shows the detailed architecture of the emulator neural network together with the neurocontroller.

Two emulator networks were trained in this study. One network for the right tail, the other for the left tail. To train the network, since nothing is known about the ideal input, one must provide the necessary input data in a different way. A combination of uniformly distributed random data was used as input to the system. All desired values were simulated before the actual training process. In the real training process, the input vector was chosen randomly from the simulated data. The model was trained in one epoch, which was found to be enough. The values of the learning coefficients used in the training epoch were 0.8 and 0.5, respectively. The squashing functions used in the networks were hyperbolic tangent functions. Scaling of the input and output data pairs was necessary, since the effective range of the hyperbolic tangent function used is between -1 and 1. In this paper, usually the largest element in any input vector was used to scale the inputs to the specified range.

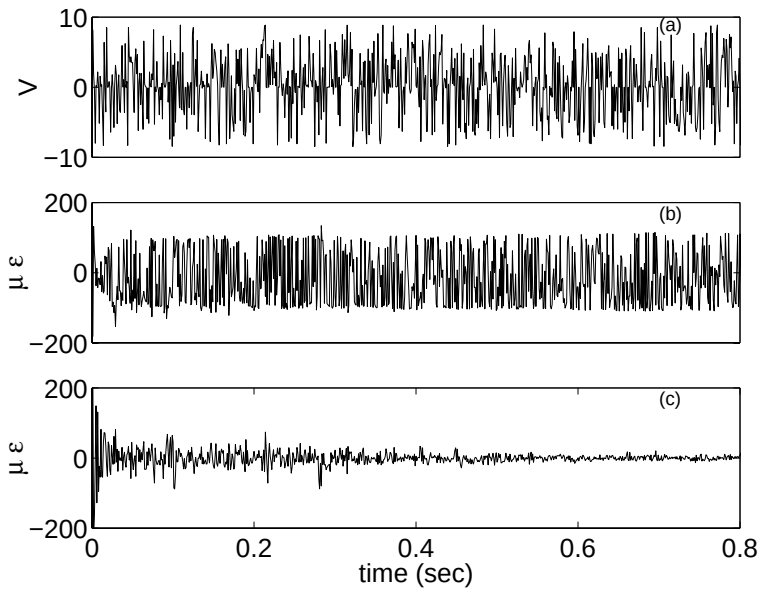

Figure 4.2: Training of the right tail (a) input forcing, (b) tail response, and (c) error between the desired and the network responses

The appropriate scaling factor was used before any neural network simulations. At the end, the output data was then scaled back to recover the original range of values of the signal. Figures 4.2 and 4.3 represent the results of this training for the right and left tails. These plots show the input to the system in volts, the output in microstrains, and the corresponding error between the desired and the actual responses of the network.

4.5 Model Validation

In general, model validation addresses verification of the dynamic model with respect to its prediction accuracy. Model validation is a significant step within the model development procedure. Validation tests ensure adequacy of the generalization of the model to transient and stationary operating states, which were not introduced to the network during its training. Validation signals can be chosen arbitrarily, so that relevant process characteristics in certain ranges can be verified. Figures 4.4 and 4.5 show the output signal from both the model and

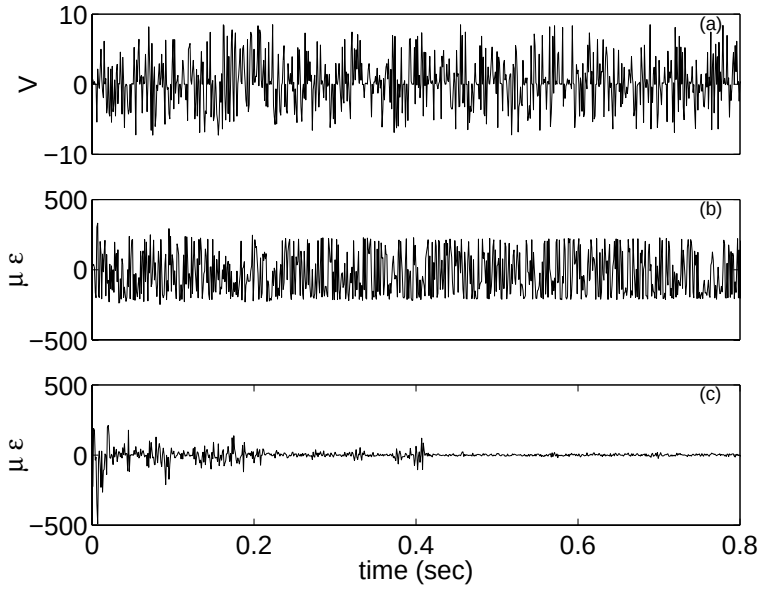

Figure 4.3: Training of the left tail (a) input forcing, (b) tail response, and (c) error between the desired and the network responses

the neural net after fixing the weights for both the right and left tails. The input signal used was provided by a proportional derivative control law and it was used to validate the trained MLP network. We know that such an input signal will not affect the response of the tails since the external disturbance to the system is parametric. This signal possessed different characteristics compared to the signals used for the training.

Clearly, the MLP model neural network identified the dynamics of the twin tails and can predict the system response to a high degree of accuracy. A prime advantage of the MLP neural network is its capability to generate the steady-state characteristics of the dynamic process identified.

4.6 Model Based Control

The second step of the design was to train the controller network, having replaced the plant by its neural network model. Only strain can be measured from the twin tails. Therefore,

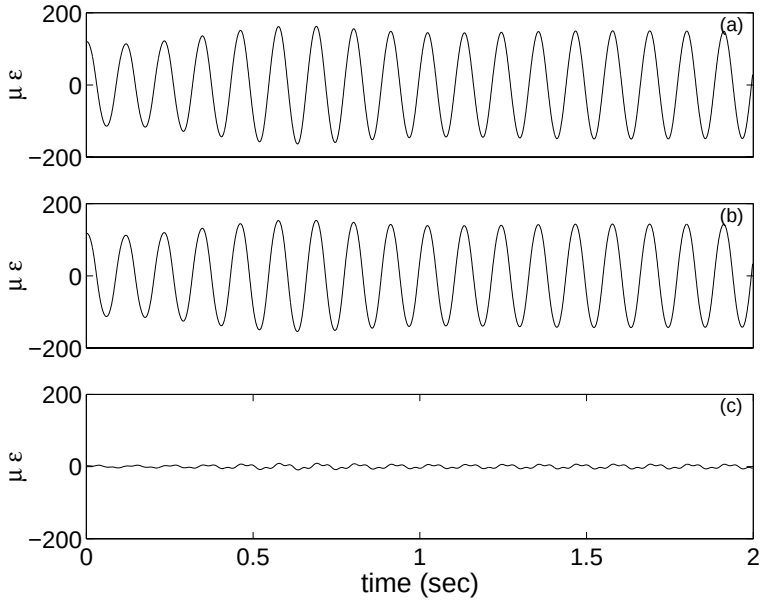

Figure 4.4: Validation of the right-tail neural network: (a) model output signal, (b) neural network output signal , and (c) error between the output of the model and the neural network output

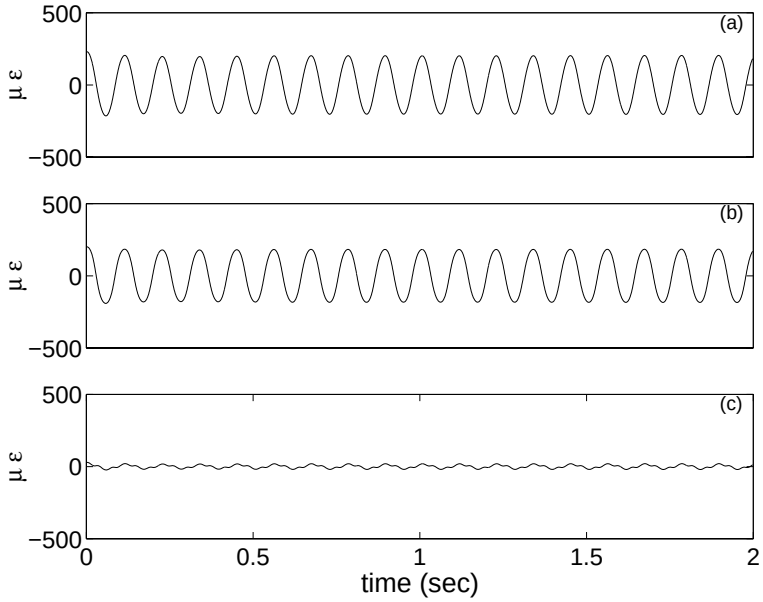

Figure 4.5: Validation of the left-tail neural network: (a) model output signal, (b) neural network output signal , and (c) error between the output of the model and the neural network output

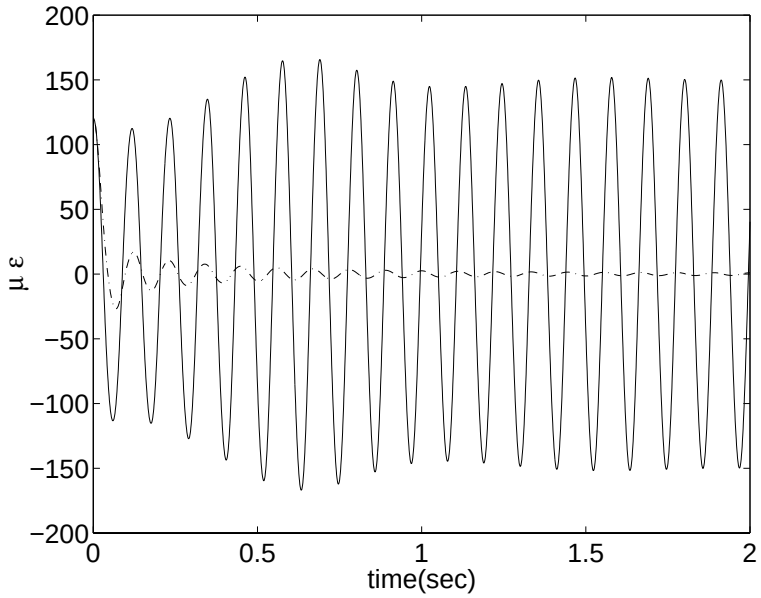

Figure 4.6: Time history of the response of the right tail(-) without control and (-.)with control.

the strain signal was chosen to be the input to the neurocontroller; that is, two delayed versions of it $y(k-1)$ and $y(k-2)$. The outputs of the neurocontroller f_1 and f_2 were used as inputs to the neuroemulator (the plant model). Its output, the strain $y(k)$ of the tail, was computed and the error function e was calculated as the difference between the computed output strain of the neuroemulator and the model reference. The weights of the actuation network were adjusted based on the control command errors computed from the error function backpropagating through the emulator network, which was fixed. This process was done for both tails. The target response for these cases was chosen to be once a second-order oscillator with a high-damping ratio $\zeta = 0.707$ and the same natural frequency as the true system and the other time zero. In both cases, the training process converged quickly, with the model reference being slightly slower than the zero reference. The neurocontroller used was implemented as 2-5-1 MLP. Figures 4.6 and 4.7 display the results of training the cascaded system. From these figures, it is clear that the neurocontroller did a good job in suppressing the steady-state vibrations of both tails.

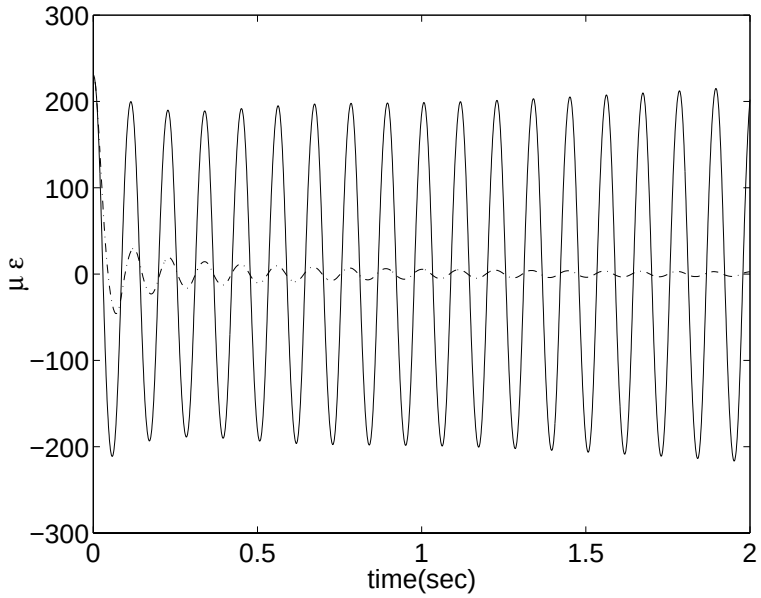

Figure 4.7: Time history of the response of the left tail(-) without control and (-.)with control.

4.7 Generalization of the Neuro-Controller

Since the governing equations of the twin tails are nonlinear, we can expect several steady-state responses coexisting with the trivial response. So the task of any controller in this case would be similar to that of a sliding-mode controller where all what we need is to place the states of the system in the basin of attraction of the trivial response (i.e., the no-vibration case). For these two coupled differential equations, there are three different possible solutions. Two of them are of the same order of magnitude of vibration, but are different in phase, and the third one has a smaller amplitude. Instead of training a neurocontroller for each solution, we tried the solution we had. Although there were many differences in the peak amplitudes of both solutions, the performance of the neurocontroller trained for the first solution was also very good for controlling the lower-amplitude solution, but this was not the case for the other way around, as seen in Figure 4.8. This is expected because, in the second case, the system was operating outside the range of the training region and was thus expected to

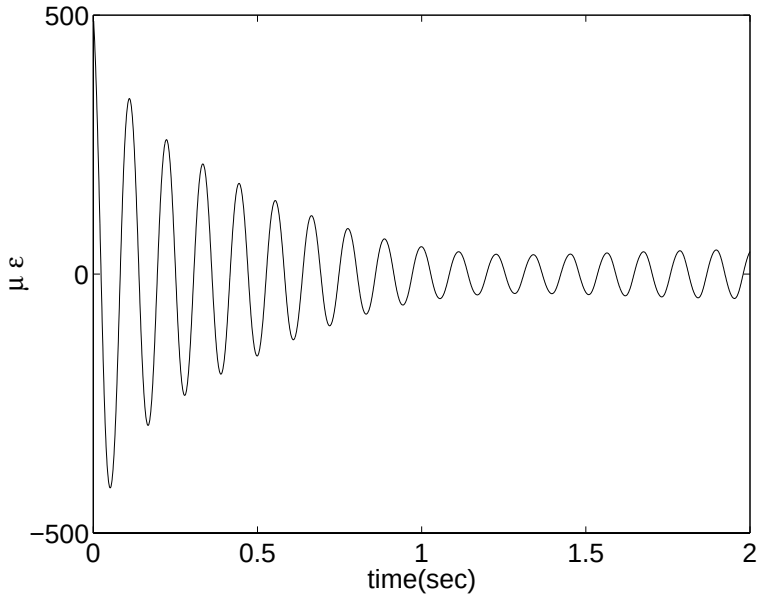

Figure 4.8: Left-tail response after control using the ungeneralized trained neural net

behave badly. Consequently, it is important for the designer to train the networks in the full regions of operation of the structure so that the networks can be generalized. Another issue that was taken into consideration during the design of the networks was that the networks were trained under high-disturbance levels so that lower-disturbance levels could also be controlled through the same trained networks. For this reason the networks were trained assuming a disturbance level of $3.5g$, which was higher than what could be achieved experimentally.

After training the controller, the model was replaced by the true plant again. The system was tested according to the signal flowchart shown in Figure 4.9. Similar plots were realized for the control of the system, which is expected since the neural network behaves similar to the mathematical model of the system.

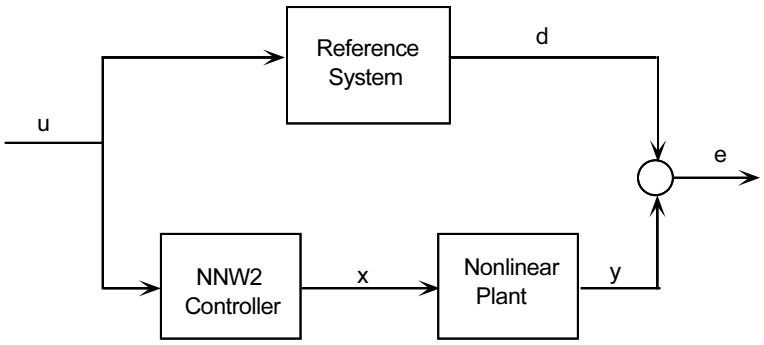

Figure 4.9: Test of the controller

4.8 Summary

This chapter demonstrated that neural networks can accurately identify and control a nonlinear system. To control the system, we first trained a neural network emulator to learn the mapping between the control signal and the response of the tails. Then, the neurocontroller learned how to control the structure with the help of the emulator network, which was used as a gateway to backpropagate the errors between the emulator's output and a reference model. This error was used to modify the weights of the neurocontroller until the system converged to the desired output provided by the reference model.

Part II

External Excitation

Chapter 5

Linear and Nonlinear Feedback Control

In this work, two simple methods of control are used and compared, namely linear and cubic velocity feedback. These control laws can be referred to as state variable feedback. For the case of velocity feedback, the velocity measurements of the tails were determined by a strain measurement (appropriately differentiated). The controller was then designed to provide a signal to the actuator proportional to the measured velocity. The actuator (PZT) was then commanded to provide force to the tails. If we were interested in also changing the stiffness of the tails, we could have also designed a control signal that is proportional to displacement, thereby employing a simple PD control (or position and derivative control). Since the system under consideration is nonlinear, linear control theory cannot predict the system response, and linear tools cannot be used to choose the optimal gains.

Based on the observation that the amplitudes of the post-bifurcation limit cycles for a nonlinear system depend strongly on the nonlinearities, one can effectively limit the size of the limit-cycle vibrations by applying nonlinear feedback control. Also, for a system, such as that considered in [62], a nonlinear feedback can be used to achieve global bifurcation control. We demonstrated that, by feeding back a term proportional to the cube of the tail

velocity, we could suppress the tail responses. We also compared the results of feeding back the linear and nonlinear velocity terms. Because of the interaction between the two tails, it was important to employ a separate controller for each tail to suppress the vibrations of both tails. Finally, we compared the instantaneous power requirements of both techniques.

5.1 Perturbation Solution

The high-amplitude response of the twin-tail assembly to a primary resonance excitation is modeled by the following two mass-normalized second-order coupled differential equations:

$$\ddot{u}_1 + \omega_1^2 u_1 + 2\epsilon\mu_1\dot{u}_1 + \epsilon\alpha_1 u_1^3 + \epsilon\mu_3\dot{u}_1 \mid \dot{u}_1 \mid -\epsilon k(u_2 - u_1) = \epsilon F\cos(\Omega t + \tau_1) + T_1 \tag{5.1}$$

$$\ddot{u}_2 + \omega_2^2 u_2 + 2\epsilon\mu_2\dot{u}_2 + \epsilon\alpha_2 u_2^3 + \epsilon\mu_4\dot{u}_2 \mid \dot{u}_2 \mid -\epsilon k(u_1 - u_2) = \epsilon F\cos(\Omega t + \tau_2) + T_2 \tag{5.2}$$

where $F\cos(\Omega t + \tau_1)$ and $F\cos(\Omega t + \tau_2)$ are the direct excitations, and T_1 and T_2 are the control forces. Let $T_1 = -\epsilon G_1\dot{u}_1^3$ and $T_2 = -\epsilon G_2\dot{u}_2^3$ for the cube of the velocity feedback control and $T_1 = -\epsilon G_3\dot{u}_1$ and $T_2 = -\epsilon G_4\dot{u}_2$ for the velocity feedback control, where G_1, G_2, G_3, and G_4 are positive constants.

We use the method of multiple scales [59] to generate a first-order approximate solution of equations (5.1) and (5.2) when $\Omega \approx \omega_1$ and $\omega_2 \approx \omega_1$. We describe in detail the analysis for the case of nonlinear velocity feedback and then present the results for the linear velocity feedback case. To this end, we seek a first-order uniform expansion of the solution of equations (5.1) and (5.2) in the form

$$u_1 = u_{11}(T_0, T_1) + \epsilon u_{12}(T_0, T_1) + \cdots \tag{5.3}$$

$$u_2 = u_{21}(T_0, T_1) + \epsilon u_{22}(T_0, T_1) + \cdots \tag{5.4}$$

where $T_0 = t$ is a fast time scale and $T_1 = \epsilon t$ is a slow time scale. In terms of T_0 and T_1, the time derivatives become

$$\frac{d}{dt} = D_0 + \epsilon D_1 + \cdots$$

$$\frac{d^2}{dt^2} = D_0^2 + 2\epsilon D_0 D_1 + \cdots \tag{5.5}$$

where $D_n = \frac{\partial}{\partial T_n}$. Substituting equations (5.3)–(5.5) into equations (5.1) and (5.2) and equating coefficients of like powers of ϵ yields

$O(\epsilon^0)$:

$$D_0^2 u_{11} + \omega_1^2 u_{11} = 0 \tag{5.6}$$

$$D_0^2 u_{21} + \omega_2^2 u_{21} = 0 \tag{5.7}$$

$O(\epsilon)$:

$$\begin{aligned} D_0^2 u_{12} + \omega_1^2 u_{12} = & -2D_0 D_1 u_{11} - 2\mu_1 D_0 u_{11} + \eta_1 k(u_{21} - u_{11}) - \alpha_1 u_{11}^3 \\ & -\mu_3 D_0 u_{11} \mid D_0 u_{11} \mid + F\cos(\Omega t + \tau_1) - G_1 (D_0 u_{11})^3 \end{aligned} \tag{5.8}$$

$$\begin{aligned} D_0^2 u_{22} + \omega_2^2 u_{22} = & -2D_0 D_1 u_{21} - 2\mu_2 D_0 u_{21} + \eta_2 k(u_{11} - u_{21}) - \alpha_2 u_{21}^3 \\ & -\mu_4 D_0 u_{21} \mid D_0 u_{21} \mid + F\cos(\Omega t + \tau_2) - G_2 (D_0 u_{21})^3 \end{aligned} \tag{5.9}$$

The general solutions of equations (5.6) and (5.7) can be written as

$$u_{11} = A_1(T_1) e^{i\omega_1 T_0} + \bar{A}_1(T_1) e^{-i\omega_1 T_0} \tag{5.10}$$

$$u_{21} = A_2(T_1) e^{i\omega_2 T_0} + \bar{A}_2(T_1) e^{-i\omega_2 T_0} \tag{5.11}$$

where the $A_i(T_1)$ are determined by eliminating the secular terms from the next-order approximation. Substituting equations (5.10) and (5.11) into equations (5.8) and (5.9) yields

$$\begin{aligned} D_0^2 u_{12} + \omega_1^2 u_{12} = & -2i\omega_1 A_1' e^{i\omega_1 T_0} - 2\mu_1 i\omega_1 A_1 e^{i\omega_1 T_0} + \eta_1 k(A_2 e^{i\omega_2 T_0} - A_1 e^{i\omega_1 T_0}) \\ & -\alpha_1 A_1^3 e^{3i\omega_1 T_0} - 3\alpha_1 A_1^2 \bar{A}_1 e^{i\omega_1 T_0} - \mu_3 [(i\omega_1 A_1 e^{i\omega_1 T_0}) | i\omega_1 A_1 e^{i\omega_1 T_0} |] \\ & + \frac{1}{2} F e^{i(\Omega T_0 + \tau_1)} - G_1 \Big[- i\omega_1^3 A_1^3 e^{3i\omega_1 T_0} + 3i\omega_1^3 A_1^2 \bar{A}_1 e^{i\omega_1 T_0} \Big] + cc \end{aligned} \tag{5.12}$$

$$\begin{aligned} D_0^2 u_{22} + \omega_2^2 u_{22} = & -2i\omega_2 A_2' e^{i\omega_2 T_0} - 2\mu_2 i\omega_2 A_2 e^{i\omega_2 T_0} + \eta_2 k(A_2 e^{i\omega_2 T_0} - A_2 e^{i\omega_2 T_0}) \\ & -\alpha_2 A_1^3 e^{3i\omega_2 T_0} - 3\alpha_2 A_2^2 \bar{A}_2 e^{i\omega_2 T_0} - \mu_4 [(i\omega_2 A_2 e^{i\omega_2 T_0}) | i\omega_2 A_2 e^{i\omega_2 T_0} |] \\ & + \frac{1}{2} F e^{i(\Omega T_0 + \tau_2)} - G_2 \Big[- i\omega_2^3 A_2^3 e^{3i\omega_2 T_0} + 3i\omega_2^3 A_2^2 \bar{A}_2 e^{i\omega_2 T_0} \Big] + cc \end{aligned} \tag{5.13}$$

where *cc* denotes the complex conjugate of the preceding terms. Eliminating the terms that produce secular terms in equations (5.12) and (5.13) yields

$$\begin{aligned} 2i\omega_1 A_1' + 2\mu_1 i\omega_1 A_1 = {} & \eta_1 k A_2 e^{i\sigma_2 T_1} - \eta_1 k A_1 - 3\alpha_1 A_1^2 \bar{A}_1 \\ & + \frac{1}{2} F e^{i(\sigma_1 T_1 + \tau_1)} - i\frac{4}{3\pi}\mu_3 \omega_1^2 a_1^2 e^{i\beta_1} - 3G_1 i\omega_1^3 A_1^2 \bar{A}_1 \qquad (5.14) \\ 2i\omega_2 A_2' + 2\mu_2 i\omega_2 A_2 = {} & \eta_2 k A_1 e^{-i\sigma_2 T_1} - \eta_2 k A_2 - 3\alpha_2 A_2^2 \bar{A}_2 \\ & + \frac{1}{2} F e^{i(\sigma_1 T_1 - \sigma_2 T_1 + \tau_2)} - i\frac{4}{3\pi}\mu_4 \omega_2^2 a_2^2 e^{i\beta_2} - 3G_2 i\omega_2^3 A_2^2 \bar{A}_2 \qquad (5.15) \end{aligned}$$

Rewriting the A_n in terms of polar coordinates as

$$A_n = \frac{1}{2} a_n e^{i\beta_n} \qquad (5.16)$$

and separating real and imaginary parts in equations (5.14) and (5.15), we obtain

$$\begin{aligned} a_1' &= \frac{F}{2\omega_1}\sin\gamma_1 - \mu_1 a_1 - \frac{3}{8}G_1\omega_1^2 a_1^3 + \frac{\eta_1 k a_2}{2\omega_1}\sin\gamma_2 - \frac{4\mu_3\omega_1}{3\pi}a_1^2 \qquad (5.17) \\ a_2' &= -\frac{F}{2\omega_2}\sin(\tau_1 - \tau_2 - \gamma_1 + \gamma_2) - \frac{\eta_2 k a_1}{2\omega_2}\sin\gamma_2 - \mu_2 a_2 - \frac{3}{8}G_2\omega_2^2 a_2^3 - \frac{4\mu_4\omega_2}{3\pi}a_2^2 \qquad (5.18) \\ \gamma_1' &= \sigma_1 - \frac{\eta_1 k}{2\omega_1} + \frac{F}{2\omega_1 a_1}\cos\gamma_1 - \frac{3\alpha_1}{8\omega_1}a_1^2 + \frac{\eta_1 k a_2}{2\omega_1 a_1}\cos\gamma_2 \qquad (5.19) \\ \gamma_2' &= \sigma_2 - \frac{\eta_1 k}{2\omega_1} + \frac{\eta_2 k}{2\omega_2} + \frac{F}{2\omega_1 a_1}\cos\gamma_1 - \frac{3\alpha_1}{8\omega_1}a_1^2 - \frac{F}{2\omega_2 a_2}\cos(\tau_1 - \tau_2 - \gamma_1 + \gamma_2) \\ & \quad - \frac{\eta_2 k a_1}{2\omega_2 a_2}\cos\gamma_2 + \frac{\eta_1 k a_2}{2\omega_1 a_1}\cos\gamma_2 + \frac{3\alpha_2}{8\omega_2}a_2^2 \qquad (5.20) \end{aligned}$$

where

$$\begin{aligned} \gamma_1 &= \sigma_1 T_1 + \tau_1 - \beta_1 \\ \gamma_2 &= \sigma_2 T_1 - \beta_1 + \beta_2 \qquad (5.21) \end{aligned}$$

Rewriting the A_k in terms of Cartesian coordinates as

$$A_k = \frac{1}{2}[p_k(T_1) - iq_k(T_1)]e^{(i\nu_k T_1 + \frac{1}{2}\tau_k)}, \qquad k = 1, 2 \qquad (5.22)$$

where

$$\nu_1 = \sigma_1, \nu_2 = \sigma_1 - \sigma_2 \qquad (5.23)$$

and separating real and imaginary parts in equations (5.14) and (5.15), we obtain

$$\begin{aligned} p_1' =& -\mu_1 p_1 - \frac{3}{8}G_1\omega_1^2 p_1^3 + \frac{1}{2\omega_1}\eta_1 k q_1 - \nu_1 q_1 + \frac{3}{8\omega_1}\alpha_1 p_1^2 q_1 - \frac{3}{8}G_1\omega_1^2 p_1 q_1^2 + \frac{3}{8\omega_1}\alpha_1 q_1^3 \\ & -\frac{1}{2\omega_1}\eta_1 k q_2 - \frac{4}{3\pi}\mu_3\omega_1\sqrt{p_1^2+q_1^2}\,p_1 \end{aligned} \tag{5.24}$$

$$\begin{aligned} q_1' =& \frac{F}{2\omega_1} - \frac{1}{2\omega_1}\eta_1 k p_1 + \nu_1 p_1 - \frac{3}{8\omega_1}\alpha_1 p_1^3 + \frac{1}{2\omega_1}\eta_1 k p_2 - \mu_1 q_1 - \frac{3}{8}G_1\omega_1^2 p_1^2 q_1 \\ & -\frac{3}{8\omega_1}\alpha_1 p_1 q_1^2 - \frac{3}{8}G_1\omega_1^2 q_1^3 \end{aligned} \tag{5.25}$$

$$\begin{aligned} p_2' =& -\mu_2 p_2 - \frac{3}{8}G_2\omega_2^2 (p_2^3 + \frac{1}{2\omega_1}\eta_2 k q_1 - 4k\eta_2 q_2 - \nu_2 q_2 + \frac{3}{8\omega_2}\alpha_2 p_2^2 q_2 - \frac{3}{8}G_2\omega_2^2 p_2 q_2^2 \\ & +\frac{3}{8\omega_2}\alpha_2 q_2^3 - \frac{4}{3\pi}\mu_3\omega_1\sqrt{p_1^2+q_1^2}\,p_1 \end{aligned} \tag{5.26}$$

$$\begin{aligned} q_2' =& \frac{F}{2\omega_2} + \frac{1}{2\omega_2}\eta_2 k p_1 - \frac{1}{2\omega_2}\eta_2 k p_2 + \nu_2 p_2 - \frac{3}{8\omega_2}\alpha_2 p_2^3 - \mu_2 q_2 - \frac{3}{8}G_2\omega_2^2 p_2^2 q_2 \\ & -\frac{3}{8\omega_2}\alpha_2 p_2 q_2^2 - \frac{3}{8}G_2\omega_2^2 q_2^3 \end{aligned} \tag{5.27}$$

The performance of the control law was evaluated by calculating the equilibrium solutions of equations (5.24)–(5.27) and examining their stability as a function of the parameter σ_1 and the gains G_1 and G_2. Thus, we set the time derivatives in equations (5.24)–(5.27) equal to zero and solved the resulting system of algebraic equations for p_1, q_1, p_2, and q_2 for a specified value of one of the parameters. The amplitudes a_1 and a_2 of the responses of the two tails were then calculated from $a_i = \sqrt{p_i^2 + q_i^2}$. Since there is no closed-form solution for the four algebraic equations, we resorted to numerical techniques. Numerical integration of the modulation equations for different sets of initial conditions was used to locate some of the possible solutions for a given σ_1 and F. Then, starting with these solutions, we used a pseudo arclength scheme [60] to trace the branches of the equilibrium solutions by varying either σ_1 or F.

The stability of a particular equilibrium solution was determined by examining the eigenvalues of the Jacobian matrix of the right-hand sides of equations (5.24)–(5.27). If the real part of each eigenvalue is negative, the corresponding equilibrium solution is asymptotically stable. If the real part of any of the eigenvalues is positive, the corresponding equilibrium solution is unstable. In the next two sections, we perform the stability analysis and evaluate

the control law.

5.2 Theoretical Frequency-Response Curves

In Figure 5.1, we show frequency-response curves for the open-loop case for various levels of the excitation amplitude. The amplitude of the response depends on the detuning and amplitude of the excitation. Solid lines correspond to stable solutions, while dashed lines correspond to unstable solutions. All of the bifurcations are of the saddle-node type. For the right tail, it is clear that, as the amplitude of excitation increases, the frequency-response curves bend away from the linear curves, resulting in multivalued regions. The multivaluedness is responsible for jumps. The left tail has multivalued responses in the region between 6-8 Hz. We note here that, as the forcing amplitude increases, the nonlinearity will dominate the response. In fact according to [44], twin-tail aircraft are often subjected to high-intensity buffet loads that produce accelerations in excess of $450g$ at the tip of the vertical tail during maneuvers at high angles of attack.

Figures 5.2 and 5.3 show the responses of the closed-loop system as the feedback gain is increased for both control strategies. It is clear that, as the controller gain increases, the response amplitudes of both tails decrease. The multivaluedness of the response in the frequency range from 5 Hz to 7 Hz has been eliminated. Thus, the jumps are eliminated.

5.3 Theoretical Force-Response Curves

In Figures 5.4 and 5.5, we show the open- and closed-loop amplitude response curves for both linear and nonlinear velocity feedback. Curves (a) in both figures represent the open-loop response. It is clear from the figures that, as the excitation amplitude increases, the response amplitudes of both tails increase. We note the difference in response amplitudes of the two tails. For example, for an excitation amplitude of $2g$, the right-tail amplitude is $\approx 140\mu\epsilon$ while that of the left tail is $\approx 200\mu\epsilon$.

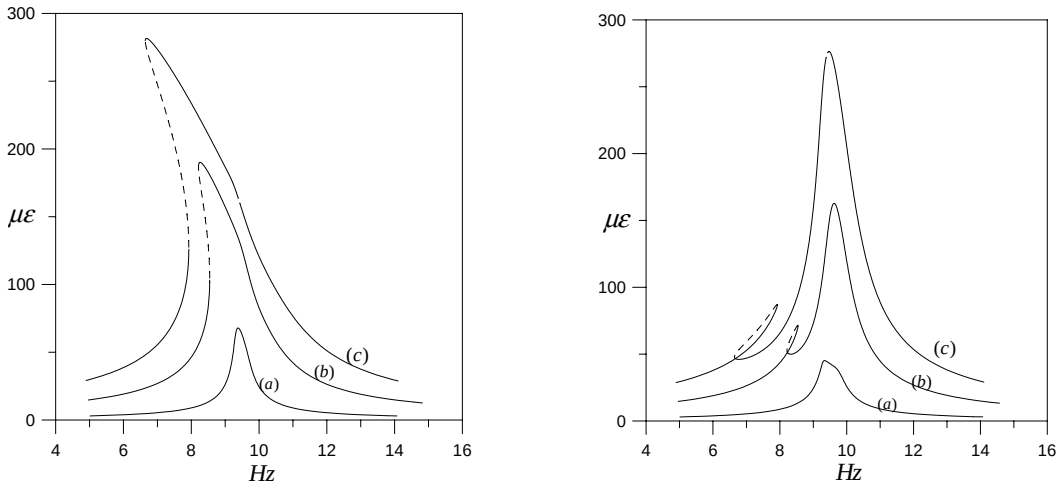

(i) right tail (ii) left tail

Figure 5.1: Effect of varying the excitation amplitude on the frequency-response curves of both tails: a) F=0.33g, b) F=1.65g, and c) F=3.3g

In Figure 5.1, curves (b) and (c) represent the closed-loop response obtained with both techniques. It is clear that the linear velocity feedback changed the system response to be linear. This is manifested by the straight line responses of both tails. On the other hand, the responses of both tails with the cubic velocity feedback is nonlinear.

5.4 Power Requirements

The present results indicate that both control techniques lead to similar dynamic responses. One performance metric that is considered as a criterion to select a control strategy is the power requirement. To this end, we apply both techniques to a simple second-order oscillator and compare the instantaneous power requirements. Thus, we consider

$$\ddot{u} + u_1 + 2\mu_1\dot{u} + T = F\cos(\Omega t) \tag{5.28}$$

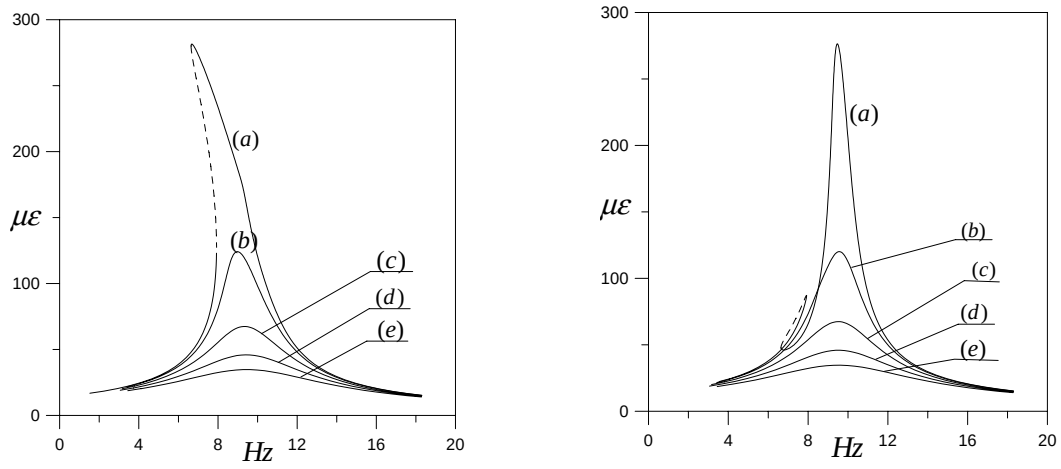

(i) right tail (ii) left tail

Figure 5.2: Effect of varying the damping ratios on the frequency-response curves: a) $G_{3,4}$=0, b) $G_{3,4}$=5, c) $G_{3,4}$=11, d) $G_{3,4}$=17, and e) $G_{3,4}$=23

where $T = G_l\dot{u}$ for the linear velocity feedback case and $T = G_n\dot{u}^3$ for the nonlinear velocity feedback case.

Using the method of multiple scales [59], we obtain the following modulation equations for the amplitude and phase:

$$a_1' = \frac{1}{2}F\sin\gamma_1 - \mu_1 a_1 - \frac{1}{2}G_l a_1 \tag{5.29}$$

$$a_1\gamma_1' = \frac{1}{2}F\cos\gamma_1 + \sigma_1 a \tag{5.30}$$

for the velocity feedback case and

$$a_2' = \frac{1}{2}F\sin\gamma_2 - \mu_2 a_2 - \frac{3}{8}G_n a_2^3 \tag{5.31}$$

$$a_2\gamma_2' = \frac{1}{2}F\cos\gamma_2 + \sigma_2 a \tag{5.32}$$

for the cubic velocity feedback case. We set the time derivatives in equations (5.29) and (5.30) equal to zero and solve the resulting system of algebraic equations for a_1 for a specified value of σ_1, which is a measure of the detuning. After some mathematical manipulation, the

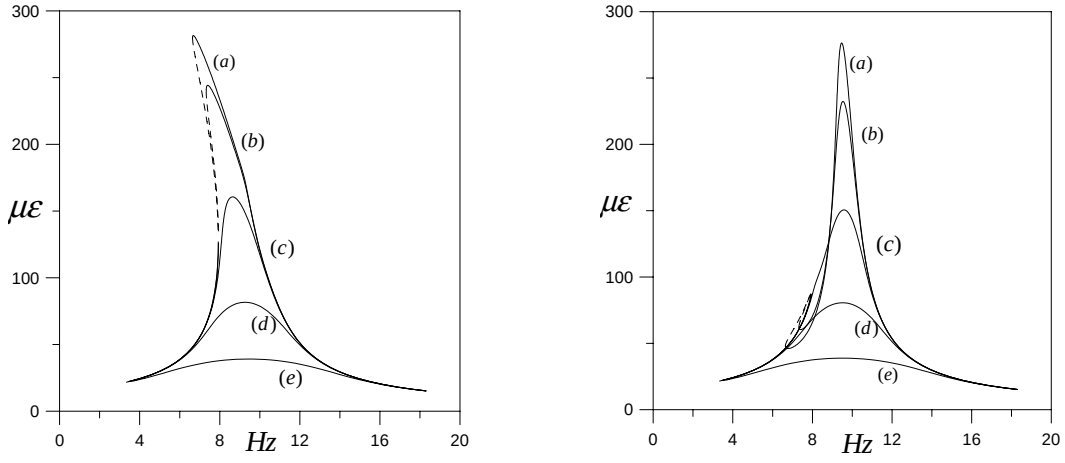

(i) right tail (ii) left tail

Figure 5.3: Effect of varying the gains on the frequency-response curves: a) $G_{1,2}$=0 , b) $G_{1,2}$=0.01, c) $G_{1,2}$=0.1, d) $G_{1,2}$=1, and e) $G_{1,2}$=10

amplitude a_1 of the response is given by

$$a_1^2 \;=\; \frac{F^2}{4\sigma^2 + (2\mu_1 + G_l)^2} \tag{5.33}$$

At perfect resonance (i.e., $\sigma = 0$) and for the open-loop case (i.e., no feedback gain $G_l = 0$), $a_{ol} = F/2\mu$, where a_{ol} is the open-loop response amplitude. Given the required reduction in the response amplitude, we specify $a_{cl} = K a_{ol}$, where $K < 1$. To achieve this, we find that

$$G_l \;=\; \left(\frac{1}{K} - 1\right) 2\mu \tag{5.34}$$

Applying a similar analysis to equations (5.31) and (5.32), we obtain

$$G_n \;=\; \frac{64\mu^3}{3K^3F^2}\left(\frac{1-K}{2}\right) \tag{5.35}$$

From equation (5.34), we note that G_l is only a function of K and μ. However, $a_{cl} = KF/2\mu$. Therefore, for a fixed closed-loop response, the larger the excitation amplitude is, the smaller the value of K is, which means a larger value of G_l. Thus G_l is an implicit function of F.

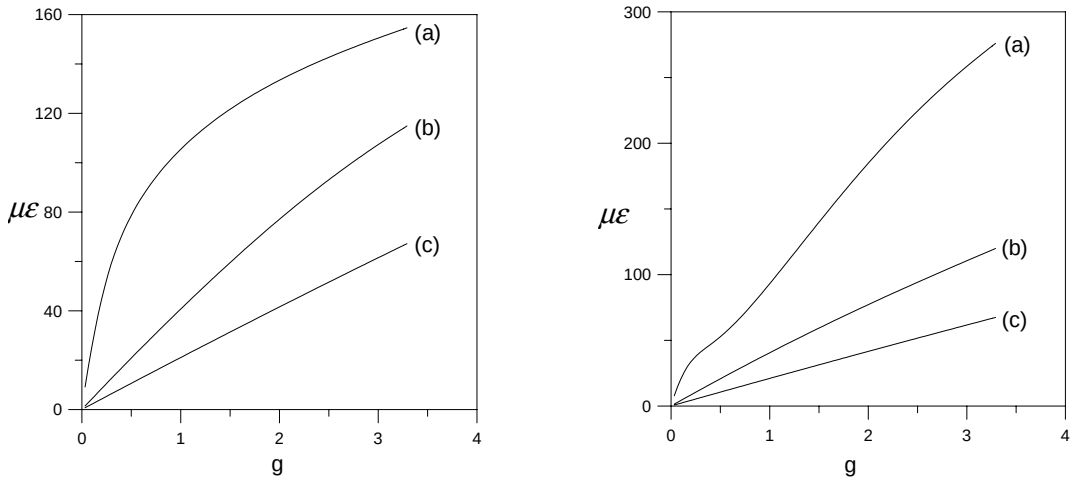

(i) Right tail (ii) Left tail

Figure 5.4: Effect of varying the damping ratios on the force-response curves for linear velocity feedback control: a) $G_{3,4} = 0$, (b) $G_{3,4} = 5$, and (c) $G_{3,4} = 11$

Assuming the response to be a single tone, we find that $u = a\cos t$. If the actuators are made of piezoceramics, then the voltage signals are given by

$$V_1 = G_l \dot{u} \quad \text{and} \quad V_2 = G_n \dot{u}^3. \tag{5.36}$$

The instantaneous power is defined by

$$P_i = V_i I_i \quad \text{for} \quad i = 1 \text{ and } 2. \tag{5.37}$$

Here, V_i is the control voltage, and the resulting current I_i is given by

$$I_i = C \frac{dV_i}{dt}, \tag{5.38}$$

where C is the effective capacitance of the actuators. Substituting equations (5.36) into equations (5.37) and (5.38), we obtain, after trigonometric manipulations,

$$P_1 = \frac{C}{2} G_l^2 a^2 \sin(2t) \quad \text{and} \quad P_2 = \frac{C\, G_n^2\, a^6}{16} \left[\frac{15}{2} \sin 2t - 6 \sin 4t + \frac{3}{2} \sin 6t \right]. \tag{5.39}$$

where P_1 and P_2 are the powers required to suppress the vibrations of the system under the linear velocity and cubic velocity feedback control laws, respectively. Figure 5.6 shows the

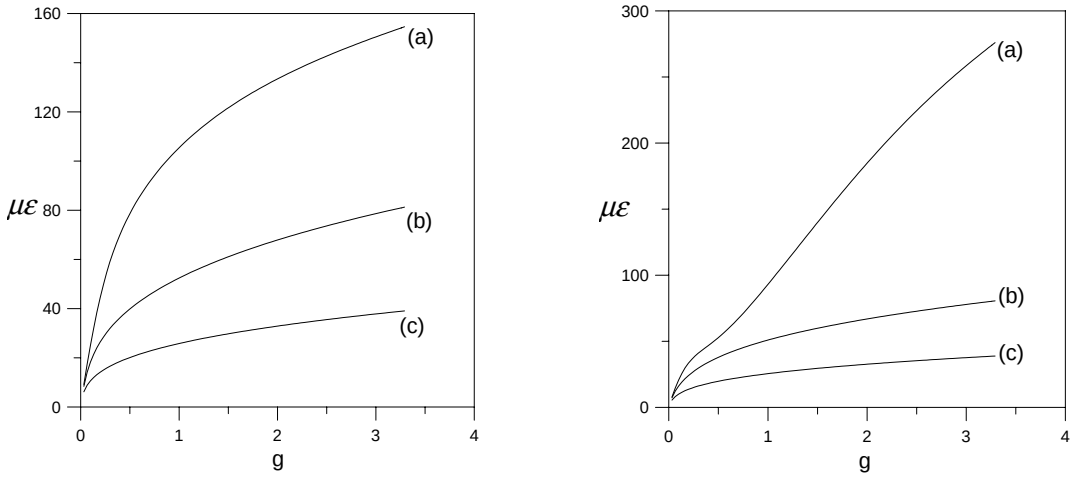

(i) Right tail (ii) Left tail

Figure 5.5: Effect of varying the gain on the force-response curves for nonlinear velocity feedback control: a) $G_{1,2} = 0$, (b) $G_{1,2} = 1$, and (c) $G_{1,2} = 10$

instantaneous power calculated from equation (5.39). It is clear that the power requirement of the cubic velocity feedback is greater than that of the linear velocity feedback. We show later that this conclusion is in agreement with the experimental results obtained for the structural model of the F-15 tail section.

5.5 Experiments

5.5.1 Experimental Setup

To test the control methods, we built a digital control system using the SIMULINK modeling software [75] and a dSPACE controller [76] in a personal computer. The SIMULINK software was used to build the control block diagram, and then the dSPACE real-time workshop was used to generate a C-code from the SIMULINK model. The C-code was then connected by the dSPACE real-time interface to the dSPACE real-time hardware system.

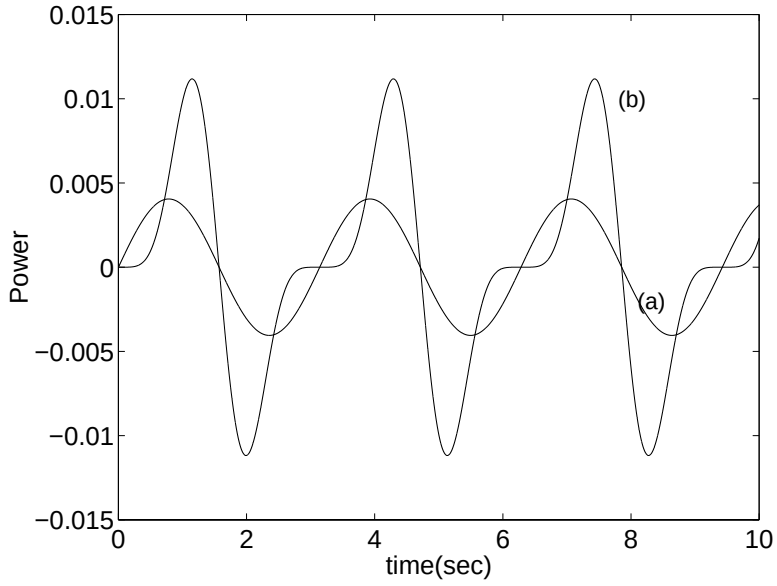

Figure 5.6: Time traces of the instantaneous power when K=0.1, μ=0.01, and F=0.1: a) linear velocity feedback and b) cubic velocity feedback

5.5.2 Setup and Procedure

Figure 5.7 shows the experimental setup. The tail deflections are measured with a series of four strain gages. The centers of the gage pairs were 0.9 *cm* and 8.5 *cm* from the top of the aluminum channels. One pair was placed on the outside of the right vertical tail; the other pair was placed on the outside of the left vertical tail. The strain gages were aligned to measure the bending moments. Changes in the gages were measured with a strain-gage conditioning amplifier in a quarter bridge configuration. The actuators were two patches of piezoelectric made from lead-zirconate-titanate. One patch was placed near the root of each tail. The dimensions of the patches were $7 \times 3.5 \times .019$ *cm*.

A series of bolts and several positioning blocks were used to fix the model. Two PZT patches were placed on the inner sides of the tails for control. Two other PZT patches were placed on the outer sides of the tails to provide the external excitation. We used PZT materials, instead of a shaker, to excite the two tails so as to avoid changing their stiffnesses and dampings.

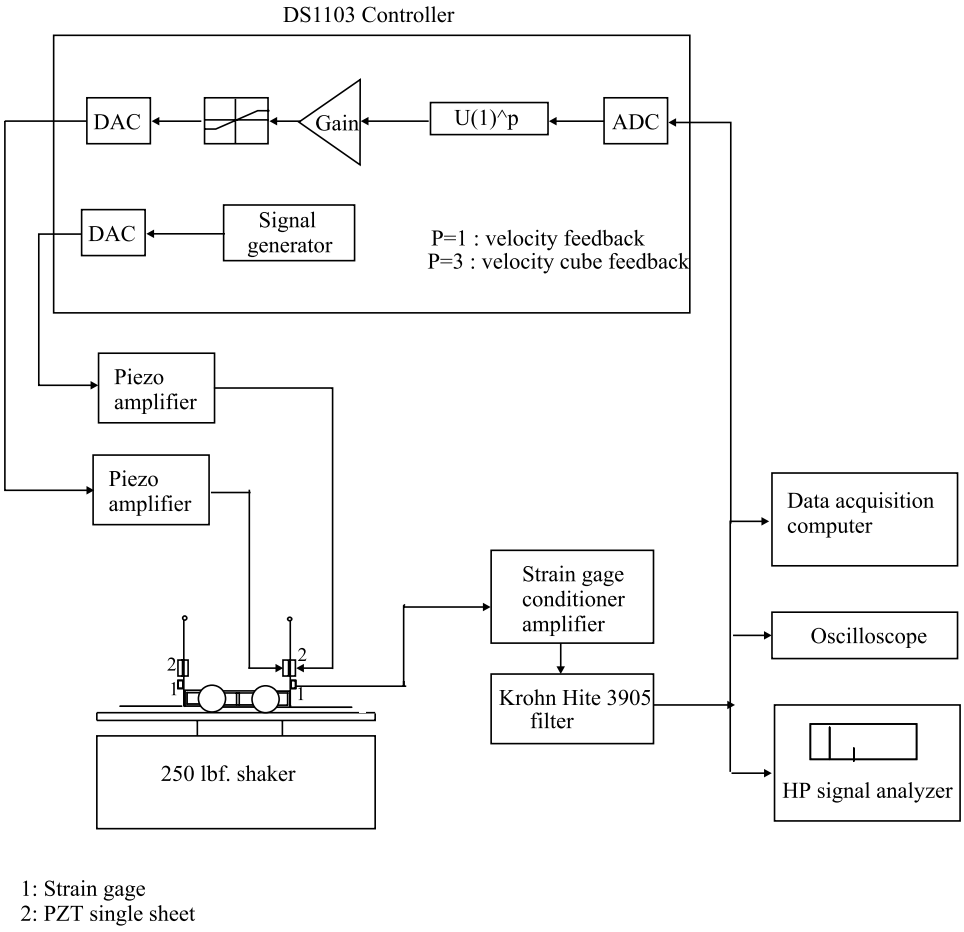

Figure 5.7: Experimental setup

The responses of the tails and the controller signals were monitored using a four-channel signal analyzer and an oscilloscope. They were also collected by a data acquisition computer software. The strain-gage signal from the conditioner was fed to the controllers, and the control signal was generated, amplified, and sent to the actuators. The velocity signal was generated using three techniques. The first was implemented using the derivative block available from the SIMULINK library. The second was implemented by integrating the strain-gage signal and then taking care of the amplitude and changing the sign. Both techniques were not stable even using a Runge-Kutta integrator scheme with the data sam-

pling period $T = 0.0005$. Thus, we used a low-pass filter to generate the velocity signal by adjusting the corner frequency of the filter and checking the signal on the oscilloscope. The difference between the approximate and the true derivative of the signal is a gain of a value equal to the natural frequency, which was taken in consideration later in the model.

5.5.3 Experimental Results

The maximum tail vibration achieved with the PZT actuators was $0.33V \approx 62\mu\epsilon$, which is in the linear response range of the tails (refer to Figure 5.1). However, the results can be generalized to the full nonlinear system because the mathematical model describing the dynamics of the tails is fairly accurate. Figure 5.8 shows the time history and the FFT of the open-loop response of the right tail. Similar results were obtained for the left tail. Figures 5.9 and 5.11 show the steady-state closed-loop response of the right tail. We used both techniques to obtain the same closed-loop response, namely 0.16 V, which represents approximately a 50% reduction in the tail response. Figures 5.10 and 5.12 show the control signals required to achieve this response with both techniques. The maximum voltage required was 0.35 V using the linear velocity and 0.6 V using the cube of the velocity. Also, we note that, for the case of the cube of the velocity feedback, several harmonics were present, which might not be convenient for the driving amplifier. Unlike vibration absorbers, the responses of the tails cannot be reduced to a minimum before saturation of the actuators. Using a larger feedback gain, one can reduce the transient time required to reach the steady state and at the same time reduce the steady-state amplitudes. However, since the control force is generated by the tail vibration itself, the controller vibration amplitude can never approach zero.

5.6 Summary

Two simple control laws were used to suppress the vibrations of the first bending modes of the 1/16 structural dynamic model of an F-15 twin tails assembly when subjected to

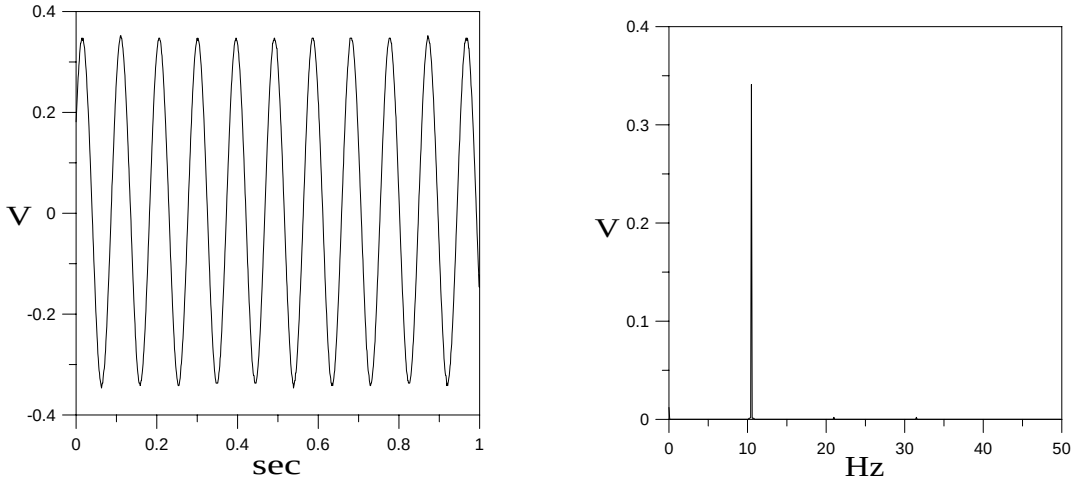

(i) time domain (ii) frequency domain

Figure 5.8: Open-loop response of the right tail

primary resonance excitations. The dynamics of the first flexural modes of the twin tails were modeled by two second-order nonlinear coupled ordinary-differential equations. The method of multiple scales was used to derive four first-order differential equations governing the amplitudes and phases of the response. Then, a bifurcation analysis was conducted to examine the stability of the closed-loop system and investigate the performance of the control laws. The feedback control eliminated all multiple responses. The amplitudes of oscillation of the tails decreased as the feedback gain was increased. Also, a parametric investigation was carried out to study the effect of changing the feedback gain. To verify the theoretical analysis, we performed experiments with the structural model of the twin-tail assembly fitted with piezoceramic actuators. We implemented the control laws using a digital signal processing (DSP) device. Good agreement between theory and experiments was found. To compare the power requirements between the two control techniques, we implemented them on a simple system. The analysis shows that the linear velocity feedback control uses less power than the cubic velocity feedback control.

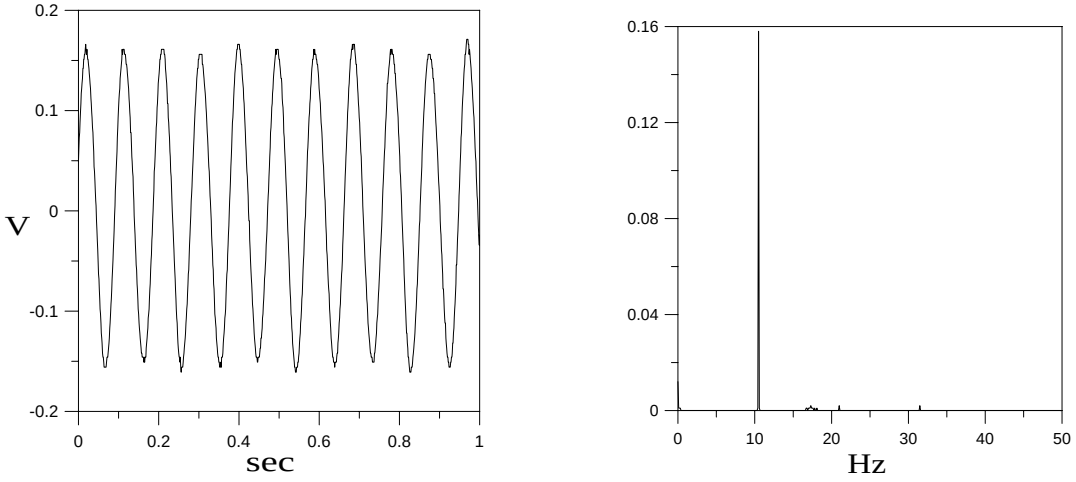

(i) time domain (ii) frequency domain

Figure 5.9: Response of the right tail with linear velocity feedback

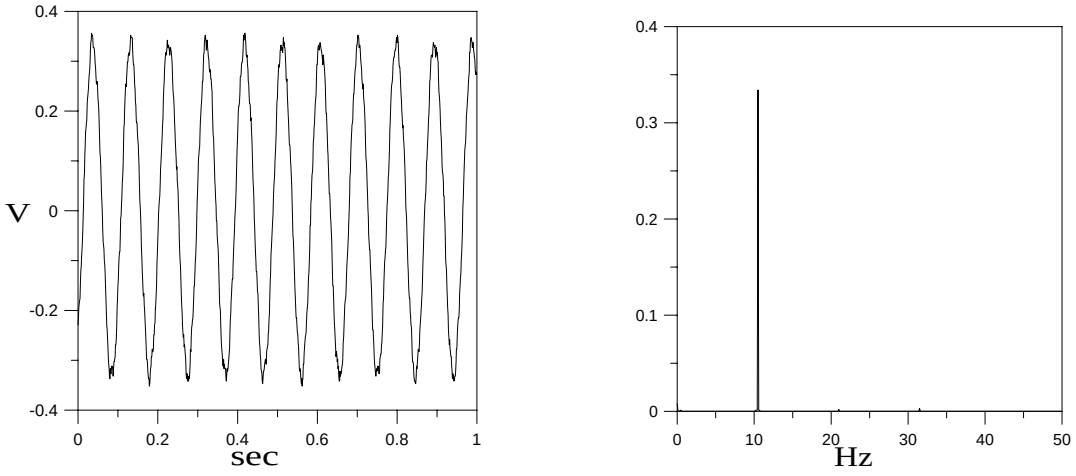

(i) time domain (ii) frequency domain

Figure 5.10: Control signal of the linear velocity feedback technique

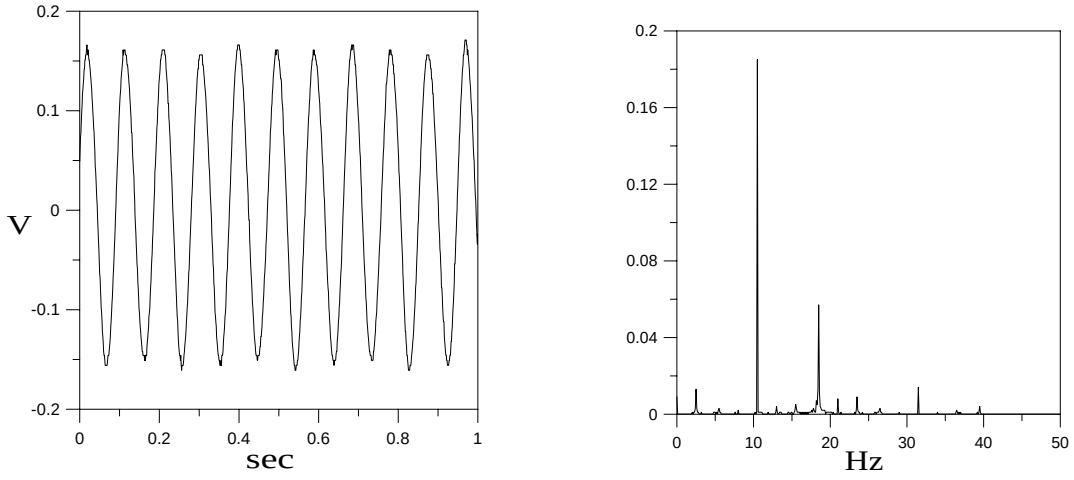

(i) time domain (ii) frequency domain

Figure 5.11: Response of the right tail with cubic velocity feedback

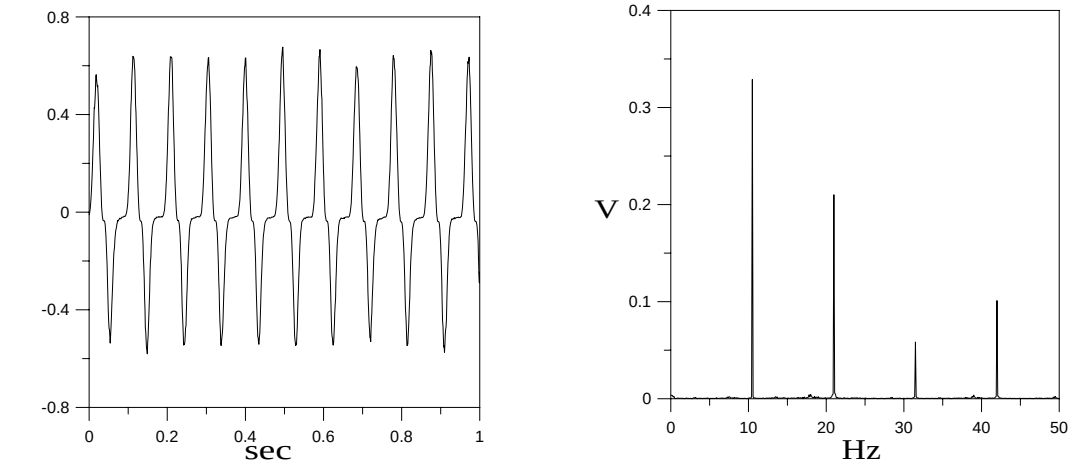

(i) time domain (ii) frequency domain

Figure 5.12: Control signal of the cubic velocity feedback technique

Chapter 6

Positive Position Feedback Control

From a structural point of view, the tail can be approximated by a cantilevered beam, and one can find examples of various active control schemes for this type of element in the literature. Our goal is to enhance the damping of targeted vibration modes. As an alternative to state variable feedback, many authors have suggested the use of second-order compensation in the feedback loop. There exist robust and efficient methods for this type of control, such as the positive position feedback of Goh and Caughey [77] and the active vibration absorber of Juang and Phan [78]. Second-order compensators have been proposed to provide loop-shaping control of structures using collocated sensor-actuator pairs. In these approaches, the compensator is used to increase the damping of a targeted structural mode in a fashion analogous to a mechanical vibration absorber.

The effect of a filter (compensator, absorber) tuned to the first mode only influences the first mode, the remaining modes are unchanged, especially for well separated modes of a system. For this particular case, this means that any disturbance to the rest of the modes will need additional damping. If we wanted to add damping to one of these modes, however, we could simply add an additional filter tuned to the correct mode to do the job.

In this chapter, we investigate the influence of two PPF filters on the response of the two tails of the scaled structural dynamic model. The advantages of PPF control lie in the

fact that the actuator dynamics are ignorable, it is based on physical quantities that can be measured accurately (i.e., the system natural frequencies), and it is amenable to strain-based actuation, which makes it an excellent choice for smart structure applications. We describe and demonstrate the roles of the filter parameters and the feedback gain on the response of the twin tails.

6.1 Theoretical Development

The closed-loop response of the twin tails to a primary resonance excitation can be modeled by two mass-normalized second-order coupled differential equations, while the dynamics of the two filters can be modeled by two second-order differential equations. The first filter targets the response of the right tail, while the second filter targets the response of the left tail. The governing equations can be written as

$$\ddot{u}_1 + \omega_1^2 u_1 + 2\epsilon\mu_1\dot{u}_1 + \epsilon\alpha_1 u_1^3 + \epsilon\mu_3\dot{u}_1 \mid \dot{u}_1 \mid -\epsilon k(u_2 - u_1) = \epsilon F\cos(\Omega t + \tau_1) + \epsilon\rho_1 u_3 \quad (6.1)$$

$$\ddot{u}_2 + \omega_2^2 u_2 + 2\epsilon\mu_2\dot{u}_2 + \epsilon\alpha_2 u_2^3 + \epsilon\mu_4\dot{u}_2 \mid \dot{u}_2 \mid -\epsilon k(u_1 - u_2) = \epsilon F\cos(\Omega t + \tau_2) + \epsilon\rho_2 u_4 \quad (6.2)$$

$$\ddot{u}_3 + 2\epsilon\zeta_3\dot{u}_3 + \omega_3^2 u_3 = \epsilon\rho_3 u_1 \quad (6.3)$$

$$\ddot{u}_4 + 2\epsilon\zeta_4\dot{u}_4 + \omega_4^2 u_4 = \epsilon\rho_4 u_2 \quad (6.4)$$

where u_3 and u_4 denote the filters coordinates, ω_3 and ω_4 are the frequencies of the filters, ζ_3 and ζ_4 are the linear damping coefficients. A collocated strain measurement is available, and thus we use $\rho_1 = G_1\omega_1^2$, $\rho_2 = G_2\omega_2^2$, $\rho_3 = \omega_3^2$, and $\rho_4 = \omega_4^2$, where G_1 and G_2 are feedback gains.

We use the method of multiple scales [59] to generate a first-order approximate solution of equations (6.1)–(6.4) when $\Omega \approx \omega_1$, $\omega_2 \approx \omega_1$, $\omega_3 \approx \omega_1$ and $\omega_4 \approx \omega_2$. To this end, we seek a first-order uniform expansion of the solution of equations (6.1)–(6.4) in the form

$$u_i = u_{i1}(T_0, T_1) + \epsilon u_{i2}(T_0, T_1) + \cdots \quad i = 1, 2, \ldots, 4 \quad (6.5)$$

$T_0 = t$ is a fast time scale and $T_1 = \epsilon t$ is a slow time scale. In terms of T_0 and T_1, the time derivatives become

$$\frac{d}{dt} = D_0 + \epsilon D_1 + \cdots$$
$$\frac{d^2}{dt^2} = D_0^2 + 2\epsilon D_0 D_1 + \cdots \tag{6.6}$$

where $D_n = \frac{\partial}{\partial T_n}$. Substituting equations (6.5) and (6.6) into equations (6.1)–(6.4) and equating coefficients of like powers of ϵ yields

$O(1)$:

$$D_0^2 u_{i1} + \omega_i^2 u_{i1} = 0 \quad i = 1, 2, \ldots, 4 \tag{6.7}$$

$O(\epsilon)$:

$$\begin{aligned} D_0^2 u_{12} + \omega_1^2 u_{12} &= -2D_0 D_1 u_{11} - 2\mu_1 D_0 u_{11} + \eta_1 k_1 (u_{21} - u_{11}) - \alpha_1 u_{11}^3 + \rho_1 u_{31} \\ &\quad -\mu_3 D_0 u_{11} \mid D_0 u_{11} \mid + F\cos(\Omega T_0 + \tau_1) \qquad (6.8) \\ D_0^2 u_{22} + \omega_2^2 u_{22} &= -2D_0 D_1 u_{21} - 2\mu_2 D_0 u_{21} + \eta_2 k_2 (u_{11} - u_{21}) - \alpha_2 u_{21}^3 + \rho_2 u_{41} \\ &\quad -\mu_4 D_0 u_{21} \mid D_0 u_{21} \mid + F\cos(\Omega T_0 + \tau_2) \qquad (6.9) \\ D_0^2 u_{32} + \omega_3^2 u_{32} &= -2D_0 D_1 u_{31} - 2\zeta_3 D_0 u_{31} + \rho_3 u_{11} \qquad (6.10) \\ D_0^2 u_{42} + \omega_4^2 u_{42} &= -2D_0 D_1 u_{41} - 2\zeta_4 D_0 u_{41} + \rho_4 u_{21} \qquad (6.11) \end{aligned}$$

The general solutions of equations **??**O1ppf) can be written as

$$u_{j1} = A_j(T_1) e^{i\omega_j T_0} + \bar{A}_j(T_1) e^{-i\omega_j T_0} \quad j = 1, 2, \ldots, 4 \tag{6.12}$$

where the $A_j(T_1)$ are determined by eliminating the secular terms at the next-level of approximation. Substituting equations (6.12) into equations (6.8)–(6.11) yields

$$\begin{aligned} D_0^2 u_{12} + \omega_1^2 u_{12} &= -2i\omega_1 A_1' e^{i\omega_1 T_0} - 2\mu_1 i\omega_1 A_1 e^{i\omega_1 T_0} + \eta_1 k (A_2 e^{i\omega_2 T_0} - A_1 e^{i\omega_1 T_0}) - \alpha_1 A_1^3 e^{3i\omega_1 T_0} \\ &\quad -3\alpha_1 A_1^2 \bar{A}_1 e^{i\omega_1 T_0} - \mu_3 [(i\omega_1 A_1 e^{i\omega_1 T_0}) | i\omega_1 A_1 e^{i\omega_1 T_0} |] + \frac{1}{2} F e^{i(\Omega T_0 + \tau_1)} \\ &\quad +\rho_1 A_3 e^{i\omega_3 T_0} + cc \qquad (6.13) \\ D_0^2 u_{22} + \omega_2^2 u_{22} &= -2i\omega_2 A_2' e^{i\omega_2 T_0} - 2\mu_2 i\omega_2 A_2 e^{i\omega_2 T_0} + \eta_2 k (A_2 e^{i\omega_2 T_0} - A_2 e^{i\omega_2 T_0}) - \alpha_2 A_1^3 e^{3i\omega_2 T_0} \end{aligned}$$

$$-3\alpha_2 A_2^2 \bar{A}_2 e^{i\omega_2 T_0} - \mu_4[(i\omega_2 A_2 e^{i\omega_2 T_0})|i\omega_2 A_2 e^{i\omega_2 T_0}|] + \frac{1}{2}Fe^{i(\Omega T_0+\tau_2)}$$
$$+\rho_2 A_4 e^{i\omega_4 T_0} + cc \tag{6.14}$$

$$D_0^2 u_{32} + \omega_3^2 u_{32} = \rho_3 A_1 e^{i\omega_1 T_0} - 2i\omega_3\zeta_3 A_3 e^{i\omega_3 T_0} - 2i\omega_3 A_3' e^{i\omega_3 T_0} + cc \tag{6.15}$$

$$D_0^2 u_{42} + \omega_4^2 u_{42} = \rho_4 A_2 e^{i\omega_2 T_0} - 2i\zeta_4\omega_4 A_4 e^{i\omega_4 T_0} - 2i\omega_4 A_4' e^{i\omega_4 T_0} + cc \tag{6.16}$$

where cc denotes the complex conjugate of the preceding terms. Eliminating the terms that produce secular terms in equations (6.13)–(6.16) yields

$$2i\omega_1 A_1' + 2\mu_1 i\omega_1 A_1 = \eta_1 k A_2 e^{i\sigma_2 T_1} - \eta_1 k A_1 - 3\alpha_1 A_1^2 \bar{A}_1 + \rho_1 A_3 e^{i\delta_1 T_1}$$
$$+\frac{1}{2}Fe^{i(\sigma_1 T_1+\tau_1)} - i\frac{4}{3\pi}\mu_3\omega_1^2 a_1^2 e^{i\beta_1} \tag{6.17}$$

$$2i\omega_2 A_2' + 2\mu_2 i\omega_2 A_2 = \eta_2 k A_1 e^{-i\sigma_2 T_1} - \eta_2 k A_2 - 3\alpha_2 A_2^2 \bar{A}_2 + \rho_2 A_4 e^{i\delta_2 T_1}$$
$$+\frac{1}{2}Fe^{i(\sigma_1 T_1-\sigma_2 T_1+\tau_2)} - i\frac{4}{3\pi}\mu_4\omega_2^2 a_2^2 e^{i\beta_2} \tag{6.18}$$

$$2i\omega_3 A_3' + 2\zeta_3 i\omega_3 A_3 = \rho_3 A_1 e^{-i\delta_1 T_1} \tag{6.19}$$

$$2i\omega_4 A_4' + 2\zeta_4 i\omega_4 A_4 = \rho_4 A_2 e^{-i\delta_2 T_1} \tag{6.20}$$

Rewriting the A_n in terms of polar coordinates as

$$A_n = \frac{1}{2}a_n e^{i\beta_n} \tag{6.21}$$

and separating real and imaginary parts in equations (6.17)–(6.20), we obtain

$$a_1' = \frac{F}{2\omega_1}\sin\gamma_1 - \mu_1 a_1 - \frac{3}{8}G_1\omega_1^2 a_1^3 + \frac{\eta_1 k a_2}{2\omega_1}\sin\gamma_2 - \frac{4\mu_3\omega_1}{3\pi}a_1^2 + \frac{\rho_1 a_3}{2\omega_1}\sin\gamma_3 \tag{6.22}$$

$$a_2' = -\frac{F}{2\omega_2}\sin(\tau_1-\tau_2-\gamma_1+\gamma_2) - \frac{\eta_2 k a_1}{2\omega_2}\sin\gamma_2 - \mu_2 a_2 - \frac{3}{8}G_2\omega_2^2 a_2^3 - \frac{4\mu_4\omega_2}{3\pi}a_2^2$$
$$+\frac{\rho_2 a_4}{2\omega_2}\sin\gamma_4 \tag{6.23}$$

$$a_3' = -\frac{\rho_3 a_1}{2\omega_3}\sin\gamma_3 - \zeta_3 a_3 \tag{6.24}$$

$$a_4' = -\frac{\rho_4 a_2}{2\omega_4}\sin\gamma_4 - \zeta_4 a_4 \tag{6.25}$$

$$\gamma_1' = \sigma_1 - \frac{\eta_1 k}{2\omega_1} + \frac{F}{2\omega_1 a_1}\cos\gamma_1 - \frac{3\alpha_1}{8\omega_1}a_1^2 + \frac{\eta_1 k a_2}{2\omega_1 a_1}\cos\gamma_2 + \frac{\rho_1 a_3}{2\omega_1 a_1}\cos\gamma_3 \tag{6.26}$$

$$\gamma_2' = \sigma_2 - \frac{\eta_1 k}{2\omega_1} + \frac{\eta_2 k}{2\omega_2} + \frac{F}{2\omega_1 a_1}\cos\gamma_1 - \frac{3\alpha_1}{8\omega_1}a_1^2 - \frac{F}{2\omega_2 a_2}\cos(\tau_1-\tau_2-\gamma_1+\gamma_2)$$
$$-\frac{\eta_2 k a_1}{2\omega_2 a_2}\cos\gamma_2 + \frac{\eta_1 k a_2}{2\omega_1 a_1}\cos\gamma_2 + \frac{3\alpha_2}{8\omega_2}a_2^2 + \frac{\rho_1 a_3}{2\omega_1 a_1}\cos\gamma_3 - \frac{\rho_2 a_4}{2\omega_2 a_2}\cos\gamma_4 \tag{6.27}$$

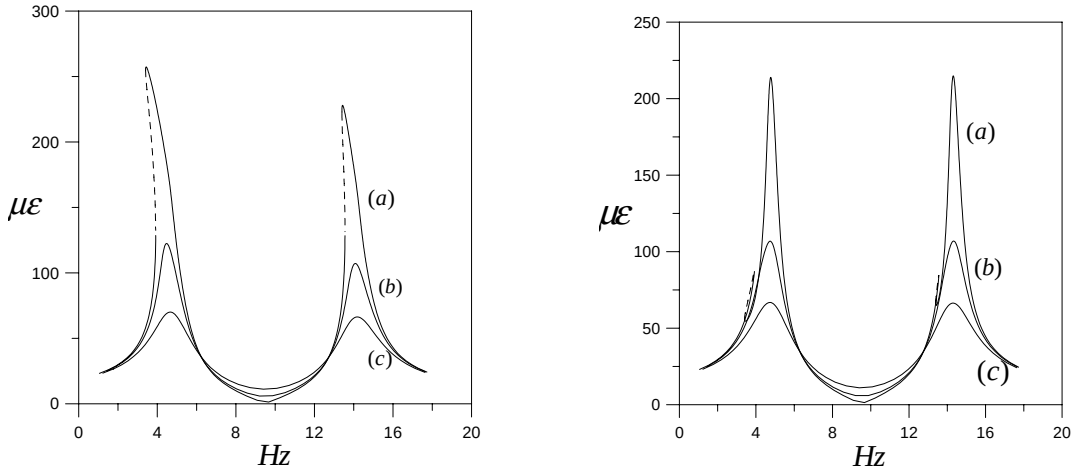

(i) right-tail response

(ii) left-tail response

Figure 6.1: Effect of varying the damping ratios of the two absorbers on the frequency-response curves of the two tails while fixing the values of the frequencies of the two absorbers ($\sigma_3 = \sigma_4 = 0$, $F = 3.3g$): a) $\zeta_{3,4} = 0.01$, b) $\zeta_{3,4} = 0.1$, and c) $\zeta_{3,4} = 0.2$.

$$\begin{aligned}\gamma_3' &= \delta_1 - \frac{k\eta_1}{2\omega_1} + \frac{F}{2\omega_1 a_1}\cos\gamma_1 - \frac{3\alpha_1}{8\omega_1}a_1^2 + \frac{\eta_1 k a_2}{2\omega_1 a_1}\cos\gamma_2 - \frac{\rho_3 a_1}{2\omega_3 a_3}\cos\gamma_3 \\ &\quad + \frac{\rho_1 a_3}{2\omega_1 a_1}\cos\gamma_3 \qquad (6.28)\\ \gamma_4' &= \delta_2 - frack\eta_2 2\omega_2 + \frac{F}{2\omega_2 a_2}\cos(\tau_1 - \tau_2 - \gamma_1 + \gamma_2) + \frac{k\eta_2 a_1}{2\omega_2 a_2}\cos\gamma_2 - \frac{3\alpha_2 a_2^2}{8\omega_2} \\ &\quad - \frac{\rho_4 a_2}{2\omega_4 a_4}\cos\gamma_4 + \frac{\rho_2 a_4}{2\omega_2 a_2}\cos\gamma_4 \qquad (6.29)\end{aligned}$$

where

$$\begin{aligned}&\gamma_1 = \sigma_1 T_1 + \tau_1 - \beta_1,\ \gamma_2 = \sigma_2 T_1 - \beta_1 + \beta_2 \\ &\gamma_3 = \delta_1 T_1 - \beta_1 + \beta_3,\ \gamma_4 = \delta_2 T_1 - \beta_2 + \beta_4 \qquad (6.30)\end{aligned}$$

Rewriting the A_k in terms of Cartesian coordinates as

$$A_k = \frac{1}{2}[p_k(T_1) - iq_k(T_1)]e^{(i\nu_k T_1 + \frac{\tau_k}{2})}, \qquad k = 1, \cdots, 4 \qquad (6.31)$$

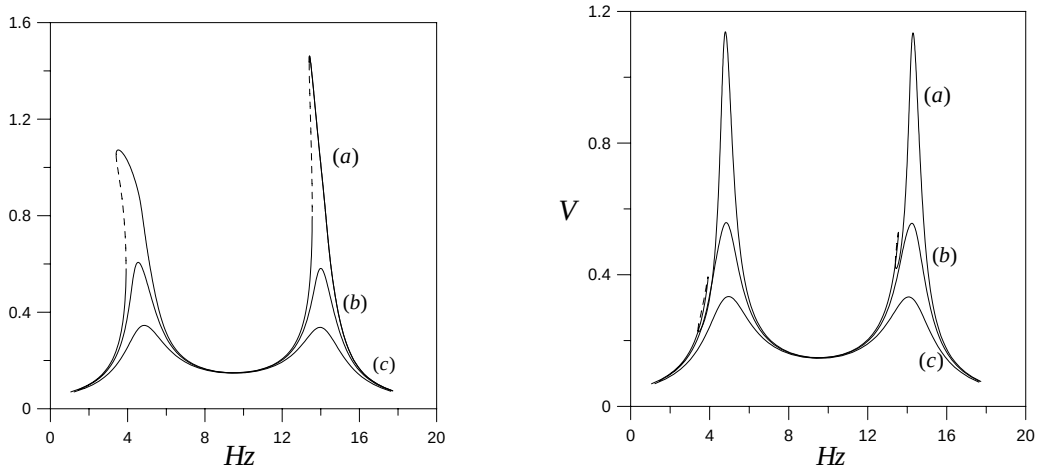

(i) right-tail absorber response

(ii) left-tail absorber response

Figure 6.2: Effect of varying the damping ratios of the two absorbers on their frequency-response curves while fixing their frequencies($\sigma_3 = \sigma_4$=0, F=3.3g): a) $\zeta_{3,4}$=0.01, b) $\zeta_{3,4}$=0.1, and c) $\zeta_{3,4}$=0.2.

where

$$\nu_1 = \sigma_1,\ \nu_2 = \sigma_1 - \sigma_2,\ \nu_3 = -\delta_1 + \sigma_1,\ \nu_4 = -\delta_2 + \sigma_1 - \sigma_2 \tag{6.32}$$

and separating the real and imaginary parts in equations (6.17)–(6.20), we obtain

$$\begin{aligned} p_1' =& -\mu_1 p_1 + \frac{1}{2\omega_1}\eta_1 k q_1 - \nu_1 q_1 + \frac{3}{8\omega_1}\alpha_1 p_1^2 q_1 + \frac{3}{8\omega_1}\alpha_1 q_1^3 \\ & -\frac{1}{2\omega_1}\eta_1 k q_2 - \frac{4}{3\pi}\mu_3\omega_1\sqrt{p_1^2+q_1^2}\,p_1 - \frac{\rho_1}{2\omega_1}q_3 \end{aligned} \tag{6.33}$$

$$\begin{aligned} q_1' =& \frac{1}{2\omega_1}F - \frac{1}{2\omega_1}\eta_1 k p_1 + \nu_1 p_1 - \frac{3}{8\omega_1}\alpha_1 p_1^3 + \frac{1}{2\omega_1}\eta_1 k p_2 - \mu_1 q_1 \\ & -\frac{4}{3\pi}\mu_3\omega_1\sqrt{p_1^2+q_1^2}\,q_1 - \frac{3}{8\omega_1}\alpha_1 p_1 q_1^2 + \frac{\rho_1}{2\omega_1}p_3 \end{aligned} \tag{6.34}$$

$$\begin{aligned} p_2' =& -\mu_2 p_2 + \frac{1}{2\omega_1}\eta_2 k q_1 - 4k\eta_2 q_2 - \nu_2 q_2 + \frac{3}{8\omega_2}\alpha_2 p_2^2 q_2 \\ & +\frac{3}{8\omega_2}\alpha_2 q_2^3 - \frac{4}{3\pi}\mu_3\omega_1\sqrt{p_1^2+q_1^2}\,p_1 - \frac{\rho_2}{2\omega_2}q_4 \end{aligned} \tag{6.35}$$

$$q_2' = \frac{1}{2\omega_2}F + \frac{1}{2\omega_2}\eta_2 k p_1 - \frac{1}{2\omega_2}\eta_2 k p_2 + \nu_2 p_2 - \frac{3}{8\omega_2}\alpha_2 p_2^3 - \mu_2 q_2 - \frac{4}{3\pi}\mu_4\omega_2\sqrt{p_2^2+q_2^2}\,q_2 - \frac{3}{8\omega_2}\alpha_2 p_2 q_2^2 + \frac{\rho_2}{2\omega_2}p_4 \tag{6.36}$$

$$p_3' = -\zeta_3 p_3 - \frac{\rho_3}{2\omega_3}q_1 - \nu_3 q_3 \tag{6.37}$$

$$q_3' = \frac{\rho_3}{2\omega_3}p_1 + \nu_3 p_3 - \zeta_3 q_3 \tag{6.38}$$

$$p_4' = -\zeta_4 p_4 - \frac{\rho_4}{2\omega_4}q_2 - \nu_4 q_4 \tag{6.39}$$

$$q_4' = \frac{\rho_4}{2\omega_4}p_2 + \nu_4 p_4 - \zeta_4 q_4 \tag{6.40}$$

The performance of the control was evaluated by calculating the equilibrium solutions of equations (6.33)–(6.40) and examining their stability as a function of the frequency of excitation and the gains G_i. Thus, we set the time derivatives in equations (6.33)–(6.40) equal to zero and solved the resulting system of algebraic equations for the p_i and q_i for a specified value of one of the parameters. The amplitudes a_1, a_2, a_3, and a_4 of the responses of the two tails and the two filters were then calculated from $a_i = \sqrt{p_i^2 + q_i^2}$. Since there is no closed-form solution for the eight algebraic equations, we resorted to numerical techniques. Numerical integration of the modulation equations for different sets of initial conditions was used to locate some of the possible solutions for a given frequency and amplitude of excitation. Then, starting with these solutions, we used a pseudo-arclength scheme [60] to trace the branches of the equilibrium solutions by varying the excitation frequency.

The stability of a particular equilibrium solution was determined by examining the eigenvalues of the Jacobian matrix of the right-hand sides of equations (6.33)–(6.40). If the real part of each eigenvalue is negative, the corresponding equilibrium solution is asymptotically stable. If the real part of any of the eigenvalues is positive, the corresponding equilibrium solution is unstable. In the next two sections, we present the stability analysis and evaluation of the control law.

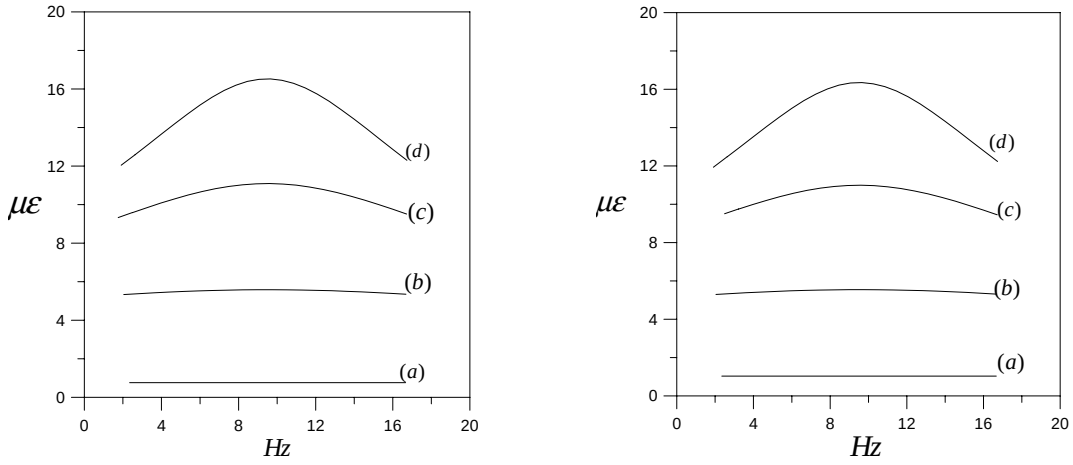

(i) right-tail response

(ii) left-tail response

Figure 6.3: Effect of varying the damping ratios of the two absorbers on the frequency-response curves of the two tails (F=3.3g): a) $\zeta_{3,4}$=0.01, b) $\zeta_{3,4}$=0.1, c) $\zeta_{3,4}$=0.2 , and d) $\zeta_{3,4}$=0.3.

6.2 Theoretical Frequency-Response Curves

In Figure 5.1, we show frequency-response curves for the open-loop case for various levels of the excitation amplitude. In the next two sections, we assume that the excitation amplitude is 3.3g (i.e., we operate on curve (c) in Figure 5.1).

6.2.1 Effect of varying the damping and the feedback gain

In the classic analysis, the system is treated as undamped with viscous damping in the absorber only. By varying the damping, the resonant response can be reduced at the expense of a decreased narrowband vibration suppression. Thus, the effect of absorber damping is to reduce the required stroke (especially at resonance) with reduced suppression bandwidth (frequency range) and depth (system response level). As the damping is increased, the broadband response increases. Thus it is possible to divide vibration absorbers into two

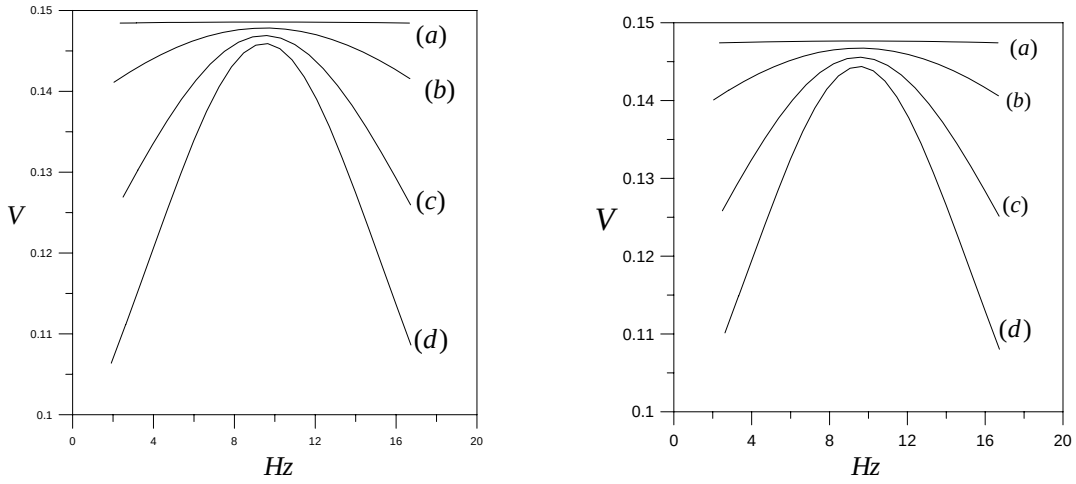

(i) right-tail absorber response

(ii) left-tail absorber response

Figure 6.4: Effect of varying the damping ratios of the two absorbers on their frequency-response curves (F=3.3 g): a) $\zeta_{3,4}$=0.01, b) $\zeta_{3,4}$=0.1, c) $\zeta_{3,4}$=0.2, and d) $\zeta_{3,4}$=0.3.

classes, narrowband absorbers with small vibration damping and broadband absorbers with larger damping. Given a fixed linear coupling, narrowband problems are those in which the excitation lies between the two resonant peaks. The effect of damping on the vibration absorber is to reduce the required stroke length at the cost of reduced suppression band. If the damping is too high, the suppression band is eliminated. Such a device is still useful for broadband applications. In our analysis, we need to get the best of the two absorbers, that is small vibration which is a characteristic of the narrowband absorber but applied on a broadband frequency range.

Figures 6.1 and 6.2 show the frequency-response curves of the two tails and the two absorbers. Here, the frequency of each absorber is set equal to the natural frequency of the first mode of the corresponding tail. In these figures, curves for different values of the damping ratios of the two absorbers are plotted. It is clear that, as the damping is increased, the resonant response is reduced at the expense of increasing the response amplitude. If the damping is decreased, the response amplitudes of the tails and the absorbers increase, which might set a

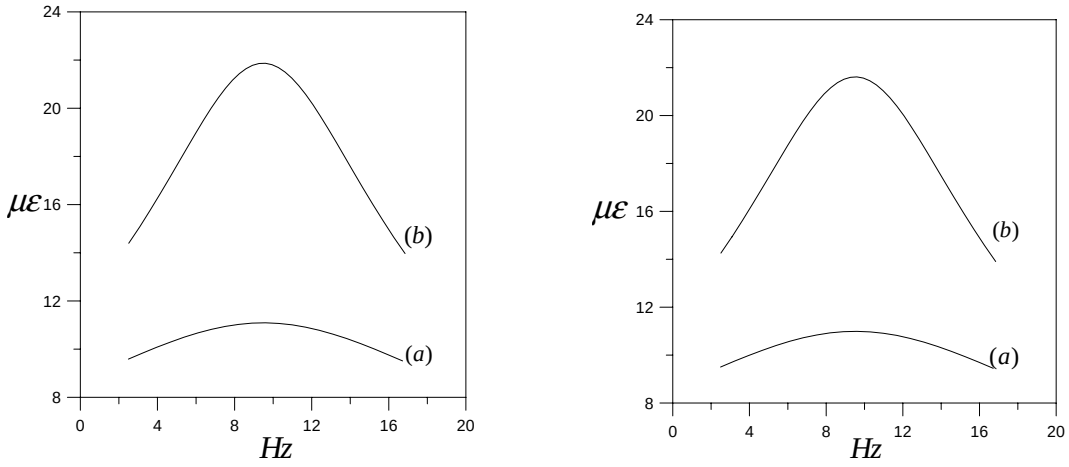

(i) right-tail response

(ii) left-tail response

Figure 6.5: Effect of varying the feedback gain on the frequency-response curves of the two tails while fixing the values of the frequencies of the two absorbers ($\zeta_{3,4}$=0.2, F=3.3g): a) G=1 and b) G=0.5.

limitation on the operation of the actuator, especially during a frequency sweep. Thus there is this tradeoff between the amplitude response of the tails and the possibility of saturating the absorbers.

To eliminate the introduction of unwanted absorber damping, Hollkamp and Starchville [79] used a linear self-tuning PZT absorber. They used a computer that senses the frequency of the structure and, through a motor driven potentiometer, adjusts the shunt's frequency to optimize the absorber performance. Oueini *et al.* [80], on the other hand, developed a code that automated the implementation of the absorber by the use of a digital signal processing (DSP) board that tracks the plant's frequency of oscillation. If this is the case, then resorting to an absorber with low damping is preferable since the response amplitudes of the tails will be minimum.

Figures 6.3 and 6.4 show frequency-response curves of the two tails and the two absorbers with the frequencies of the absorbers being automatically tuned to the excitation frequency.

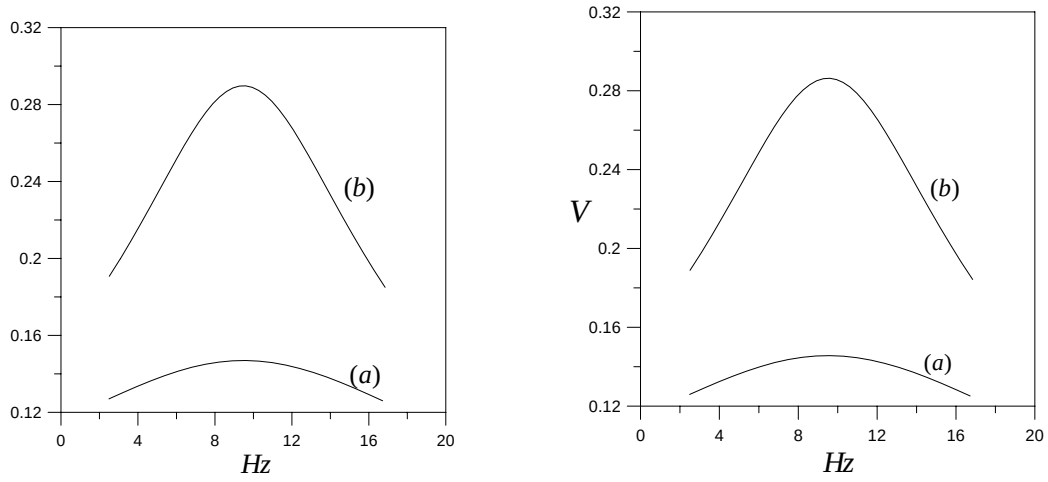

(i) right-tail absorber response

(ii) left-tail absorber response

Figure 6.6: Effect of varying the feedback gain on the frequency-response curves of the two absorbers while fixing the values of their frequencies ($\zeta_{3,4}$=0.2, F=3.3g): a) G=1 and b) G=0.5.

To theoretically implement this, for example for the right tail, we set $\Omega = \omega_1 + \sigma_1$ and $\omega_3 = \omega_1 + \sigma_3$, where Ω is the excitation frequency, ω_1 is the natural frequency of the right tail, and ω_3 is the frequency of the absorber. The latter is tuned to the response frequency of the first mode of the right tail. If we set $\sigma_3 = \sigma_1$ (i.e., the absorber frequency is equal to the excitation frequency) during a frequency sweep, we obtain Figure 6.3 (i). A similar analysis was done for the left tail. We note that σ_2 is fixed and is equal to $\omega_2 - \omega_1 = 0.085$Hz.

Figures 6.5 and 6.6 show the effect of varying the feedback gain on the responses of the tails and the absorbers. These figures were obtained for a damping ratio $\zeta_{3,4} = 0.2$ while the frequencies of the absorbers being tuned to the excitation frequency (i.e., $\Omega = \omega_3$). As the gain increases, the responses of the tails and the absorbers decrease. However, from the experiments, we found that, although this is true, the system lost stability when the gain increases beyond a threshold value. Thus, one should be careful in selecting the feedback gains so as not to destabilize the system.

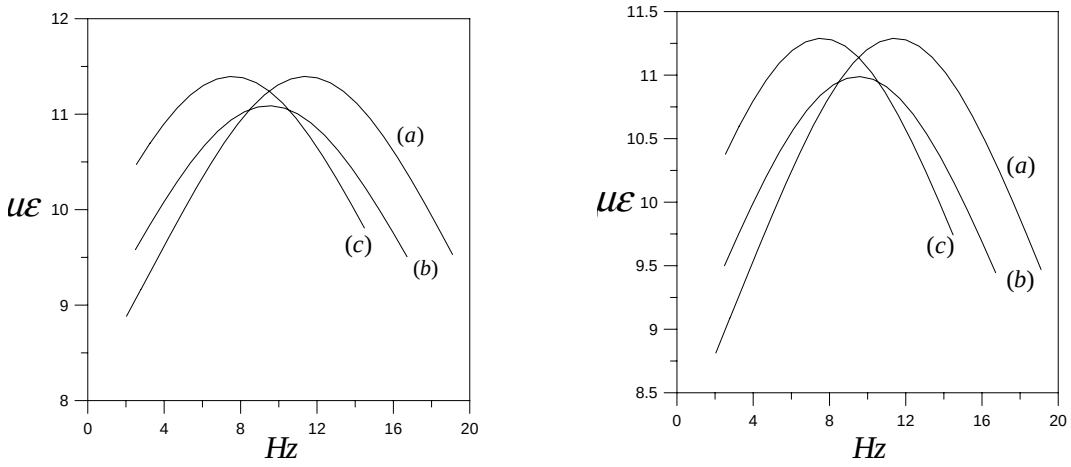

(i) right tail (ii) left tail

Figure 6.7: Effect of detuning the absorber frequency on the frequency-response curves of the two tails while fixing the values of the frequencies of the two absorbers(F=3.3 g): a) $w_{3,4} = \Omega - 2$, b) $w_{3,4} = \Omega$, and c) $w_{3,4} = \Omega + 2$

Figures 6.7 and 6.8 show the effect of detuning the absorber's frequency from the tails' natural frequencies. As can be seen the responses of the tails degrade when $\omega_{abs} = \Omega \pm 2$. We also expect this behavior to keep degrading as the detuning is increased. Thus the implementation of the technique was rendered very effective by tuning the frequency of the absorber equal to the frequency of oscillation of the tail.

6.3 Theoretical Force-Response Curves

Figure 6.9 shows the closed-loop response of the PPF filter. It is clear that the response amplitudes in this case are much less than those presented in the preceding chapter. However, this happens at the expense of complicating the system by doubling the equations of motion. A second assumption used to produce these curves is the presence of a fast frequency-detection algorithm. These make the implementation of this technique more demanding

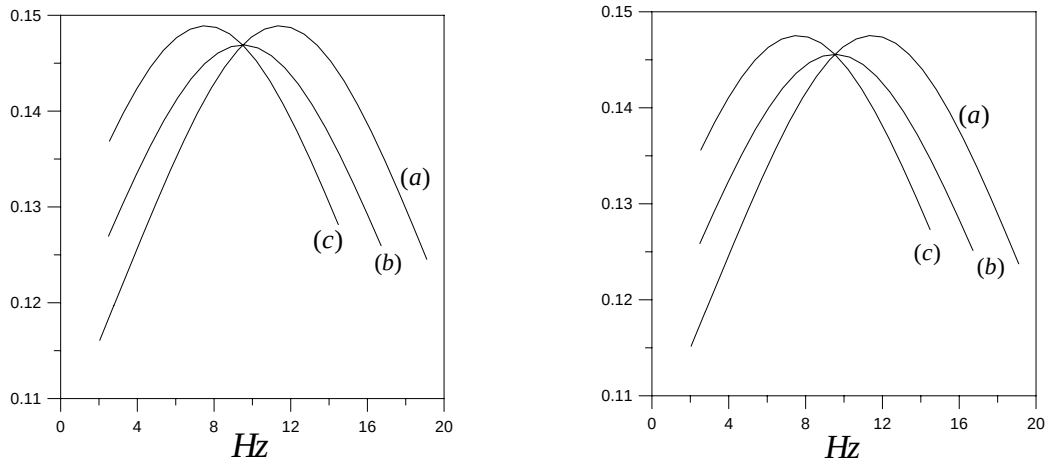

(i) right tail absorber

(ii) left tail absorber

Figure 6.8: Effect of detuning the two absorber frequencies on their frequency-response curves while fixing their frequency values (F=3.3 g): a) $w_{3,4} = \Omega - 2$, b) $w_{3,4} = \Omega$, and c) $w_{3,4} = \Omega + 2$

than the feedback control laws discussed in the preceding chapter. Final comment is that as the damping ratios of the absorbers increase, the response amplitudes of the tails increase, in agreement with the development of the positive position feedback filter (PPF) by Fanson and Caughey [81]. We also note that the response amplitude depend on the forcing level F.

6.4 Experimental Results

Figure 6.10 shows the experimental setup. The maximum tail vibration achieved with the PZT actuators was $0.33V \approx 62\mu\epsilon$, which is in the linear response range of the tails (refer to Figure 5.1). Figures 5.8 and 6.11 show the time histories and the FFT of the open- and closed-loop responses of the right tail. Similar results were obtained for the left tail. It is clear that the amplitudes of the responses are reduced by almost 10 times.

Using a larger feedback gain, one can reduce the transient time required to reach steady state and at the same time reduce the steady-state amplitudes. However, since the control

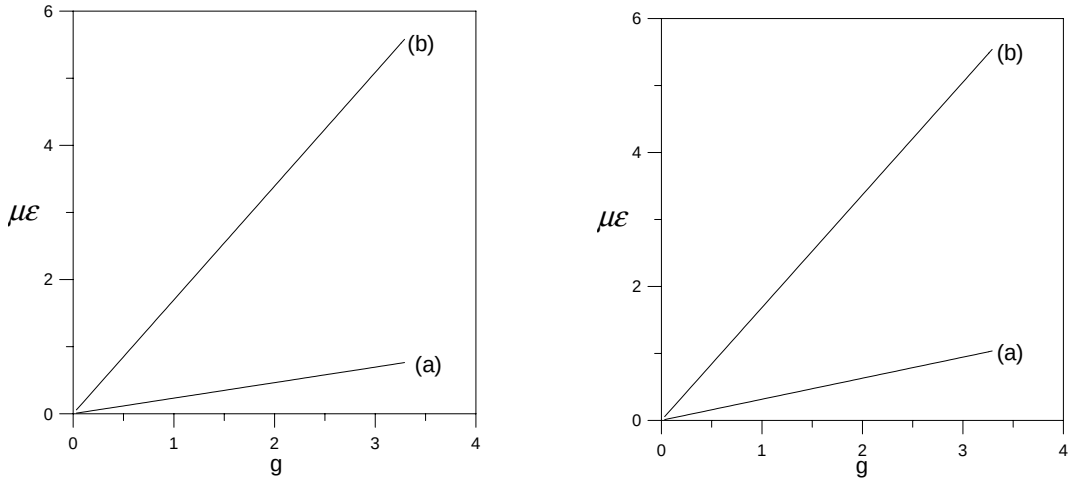

(i) right tail (ii) left tail

Figure 6.9: Effect of varying the damping ratios of the two absorbers on the force-response curves of the two tails ($freq$=9.135Hz):: a) $\zeta_{3,4}$=0.01, b) $\zeta_{3,4}$=0.1.

force is generated by the tail vibration itself, the controller vibration amplitude can never approach zero. In fact, the system loses stability when the gain increases beyond a certain value. Figure 6.12 shows the control signal sent to the power amplifier, which in turn was sent to the PZT actuators. In this figure, the system is actually on the verge of instability. Increasing the feedback gain slightly would increase the modulation of the control signal, which would destabilize system.

6.5 Summary

A positive position-feedback control was used to suppress the vibrations of the first bending modes of the twin tails when subjected to primary resonance excitations. The dynamics of the first flexural modes of the twin tails were modeled by two second-order coupled nonlinear ordinary-differential equations. A filter was coupled linearly to each of the tails. The method of multiple scales was used to derive eight first-order differential equations governing the

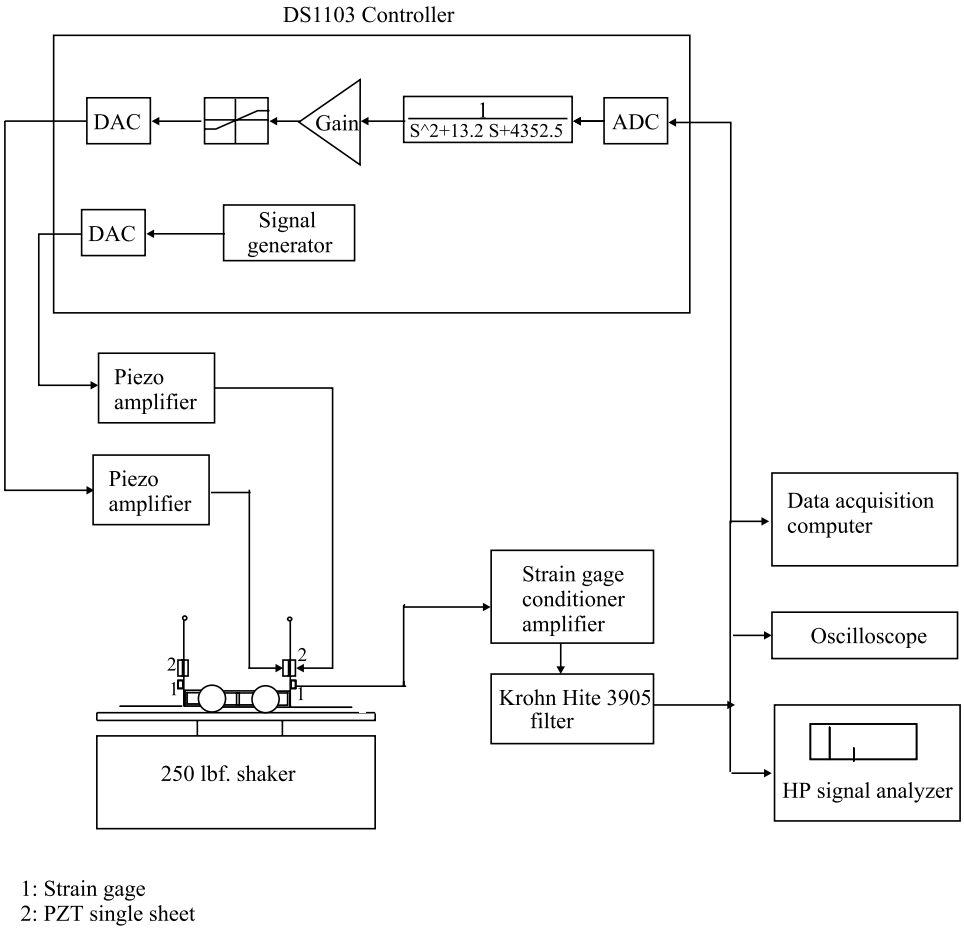

Figure 6.10: Experimental setup.

amplitudes and phases of the response. Then a bifurcation analysis was conducted to examine the stability of the closed-loop system and investigate the performance of the control law. The control eliminated all multiple responses. The amplitudes of oscillation of the tails decreased significantly. Once the absorbers' frequencies properly tuned, the control scheme possesses a wide suppression bandwidth. Also, a parametric investigation was carried out to investigate the effect of changing the damping ratios of the absorbers and the value of the feedback gain on the response. To verify the theoretical analysis, we carried out experiments on the structural model of the twin-tail assembly fitted with piezoceramic actuators. We

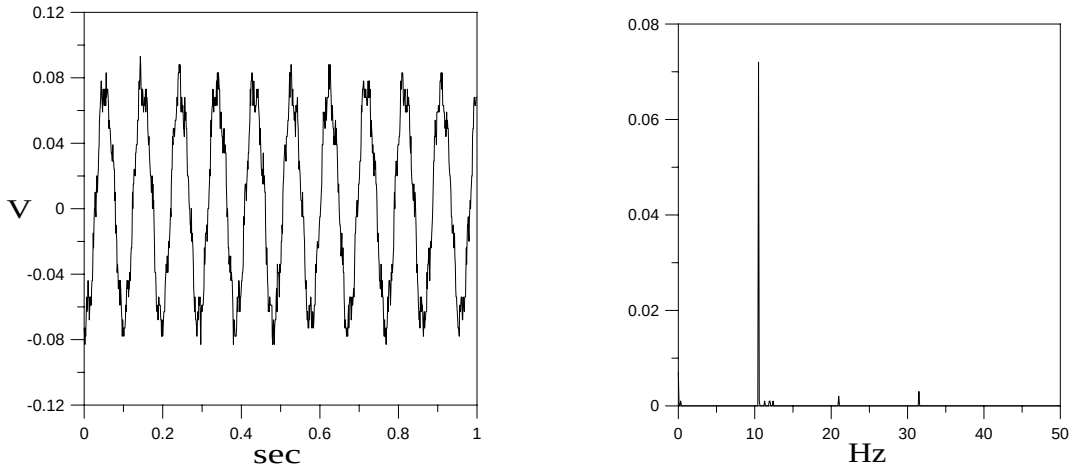

(i) time domain

(ii) frequency domain

Figure 6.11: Response of the closed-loop system of the right tail with linear absorber ($\zeta_{3,4} = 0.1$)

implemented the absorber using a digital signal processing (DSP) device. Good agreement between theory and experiments was found.

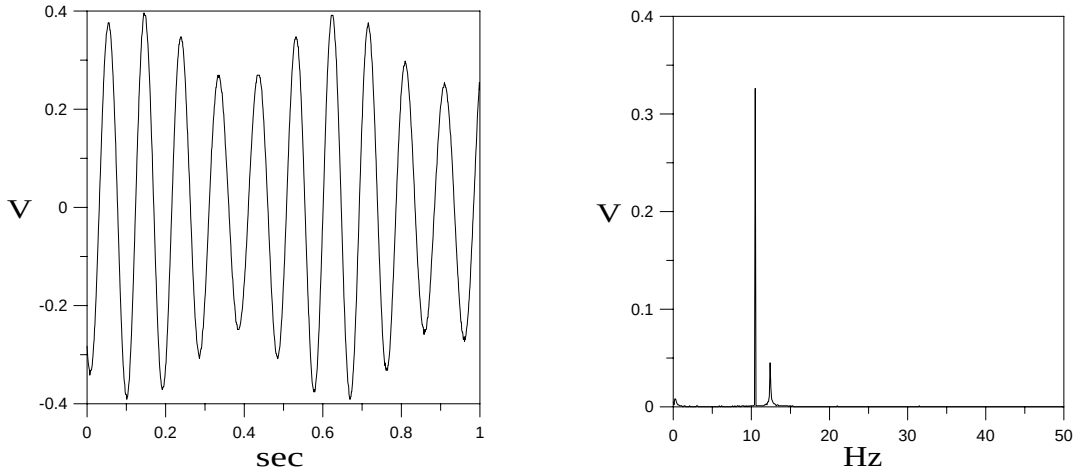

(i) time domain

(ii) frequency domain

Figure 6.12: Control signal.

Chapter 7

Saturation-Based Control

7.1 Introduction

In weakly nonlinear systems, internal resonances may occur if the linear natural frequencies are commensurate or nearly commensurate, and internal resonances provide coupling and energy exchange among the vibration modes. If two natural frequencies of a system with quadratic nonlinearities are in the ratio 2:1, there exists a saturation phenomenon [61]. When the system is excited at a frequency near the higher natural frequency, the structure responds at the frequency of excitation and the amplitude of the response increases linearly with the excitation amplitude. However, when the high-frequency modal amplitude reaches a critical value, this mode saturates and all additional energy added to the system by increasing the excitation amplitude overflows into the low-frequency mode. The critical amplitude at which the energy is transferred to the low-frequency mode depends on the damping in the low-frequency mode and the detuning between the encounter frequency and twice the natural frequency of the low-frequency mode. The smaller these two quantities are, the smaller the critical amplitude is. Although saturation was discovered in the context of ship motions, it appears in other nonlinear systems. Haddow, Barr, and Mook [82] found saturation in an L-shaped structure governed by equations having quadratic terms. In the course of their

experiments, they were able to virtually eliminate the motion in the directly excited mode by carefully tuning the natural frequencies and by reducing the damping of the structure by using spring steel. They suggested exploiting the phenomenon as a vibration absorber.

Golnaraghi [83] was the first to introduce the use of internal resonance in nonlinear control to control free vibrations. He used a second-order controller coupled to a vibration system via quadratic or cubic terms. Tuer, Golnaraghi, and Wang [84] introduced a second-order oscillator in their analysis to act as the controller. Oueini and Golnaraghi [85] then introduced an electrical circuit as the tuned additional mode and provided experimental active control of the free vibrations of a cantilevered beam.

For forced vibrations, Oueini, Nayfeh, and Pratt [86] exploited the saturation phenomenon to design and implement a nonlinear vibration absorber. Pai *et al.* [87] used PZT patches, the nonlinear saturation phenomenon, and internal resonances to control the steady-state and transient vibrations of a cantilever beam . They came up with the idea that a hybrid controller consisting of a saturation controller and a linear position-feedback controller is robust and efficient in controlling steady-state and transient vibrations. Finally, Hall [88] applied saturation control to an aeroelastic wing. The saturation-control technique is similar to that of the positive position feedback control [81] in that a tuned second-order compensator circuit is used to suppress oscillatory motion, but the controller is coupled to the system nonlinearly rather than linearly. In this Chapter, we use the saturation control to the two degree-of-freedom model of the twin-tail assembly of the F-15.

7.2 Theoretical Development

The closed-loop response of the twin tails to a primary resonance excitation can be modeled by two mass-normalized second-order coupled differential equations, while the dynamics of the two filters can be modeled by two second-order differential equations. The first filter targets the response of the right tail, while the second filter targets the response of the left

tail. The governing equations can be written as

$$\ddot{u}_1 + \omega_1^2 u_1 + 2\epsilon\mu_1\dot{u}_1 + \epsilon\alpha_1 u_1^3 + \epsilon\mu_3\dot{u}_1 \mid \dot{u}_1 \mid -\epsilon k(u_2 - u_1) = \epsilon F\cos(\Omega t + \tau_1) + \epsilon\rho_1 u_3^2 \quad (7.1)$$

$$\ddot{u}_2 + \omega_2^2 u_2 + 2\epsilon\mu_2\dot{u}_2 + \epsilon\alpha_2 u_2^3 + \epsilon\mu_4\dot{u}_2 \mid \dot{u}_2 \mid -\epsilon k(u_1 - u_2) = \epsilon F\cos(\Omega t + \tau_2) + \epsilon\rho_2 u_4^2 \quad (7.2)$$

$$\ddot{u}_3 + \omega_3^2 u_3 + 2\epsilon\zeta_3\dot{u}_3 = \epsilon\rho_3 u_1 u_3 \quad (7.3)$$

$$\ddot{u}_4 + \omega_4^2 u_4 + 2\epsilon\zeta_4\dot{u}_4 = \epsilon\rho_4 u_2 u_4 \quad (7.4)$$

where u_3 and u_4 denote the filter coordinates, ω_3 and ω_4 are the frequencies of the filters, ζ_3 and ζ_4 are the linear damping coefficients. We use $\rho_1 = 4G_1\omega_1$, $\rho_2 = 4G_2\omega_2$, $\rho_3 = 4\omega_3$, and $\rho_4 = 4\omega_4$, where G_1 and G_2 are feedback gains.

We use the method of multiple scales [59] to generate a first-order approximate solution of equations (7.1)–(7.4) when $\Omega \approx \omega_1$, $\omega_2 \approx \omega_1$, $\omega_3 \approx \omega_1$ and $\omega_4 \approx \omega_2$. To this end, we seek a first-order uniform expansion of the solution of equations (7.1)–(7.4) in the form

$$u_i = u_{i1}(T_0, T_1) + \epsilon u_{i2}(T_0, T_1) + \cdots \quad i = 1, 2, \ldots, 4 \quad (7.5)$$

$T_0 = t$ is a fast time scale and $T_1 = \epsilon t$ is a slow time scale. In terms of T_0 and T_1, the time derivatives become

$$\frac{d}{dt} = D_0 + \epsilon D_1 + \cdots$$

$$\frac{d^2}{dt^2} = D_0^2 + 2\epsilon D_0 D_1 + \cdots \quad (7.6)$$

where $D_n = \frac{\partial}{\partial T_n}$. Substituting equations (7.5) and (7.6) into equations (7.1)–(7.4) and equating coefficients of like powers of ϵ yields

$O(1)$:

$$D_0^2 u_{i1} + \omega_i^2 u_{i1} = 0 \quad i = 1, 2, \ldots, 4 \quad (7.7)$$

$O(\epsilon)$:

$$D_0^2 u_{12} + \omega_1^2 u_{12} = -2D_0 D_1 u_{11} - 2\mu_1 D_0 u_{11} + \eta_1 k_1(u_{21} - u_{11}) - \alpha_1 u_{11}^3$$

$$-\mu_3 D_0 u_{11} \mid D_0 u_{11} \mid + F\cos(\Omega t + \tau_1) + \rho_1 u_{31}^2 \tag{7.8}$$

$$D_0^2 u_{22} + \omega_2^2 u_{22} = -2D_0 D_1 u_{21} - 2\mu_2 D_0 u_{21} + \eta_2 k_2 (u_{11} - u_{21}) - \alpha_2 u_{21}^3$$
$$-\mu_4 D_0 u_{21} \mid D_0 u_{21} \mid + F\cos(\Omega t + \tau_2) + \rho_2 u_{41}^2 \tag{7.9}$$

$$D_0^2 u_{32} + \omega_3^2 u_{32} = -2D_0 D_1 u_{31} - 2\zeta_3 D_0 u_{31} + \rho_3 u_{11} u_{31} \tag{7.10}$$

$$D_0^2 u_{42} + \omega_4^2 u_{42} = -2D_0 D_1 u_{41} - 2\zeta_4 D_0 u_{41} + \rho_4 u_{21} u41 \tag{7.11}$$

The general solutions of equations (7.7) can be written as

$$u_{j1} = A_j(T_1) e^{i\omega_j T_0} + \bar{A}_j(T_1) e^{-i\omega_j T_0} \quad j = 1, 2, \ldots, 4 \tag{7.12}$$

where the $A_j(T_1)$ are determined by eliminating the secular terms at the next-level of approximation. Substituting equations (7.12) into equations (7.8)–(7.11) yields

$$D_0^2 u_{12} + \omega_1^2 u_{12} = -2i\omega_1 A_1' e^{i\omega_1 T_0} - 2\mu_1 i\omega_1 A_1 e^{i\omega_1 T_0} + \eta_1 k(A_2 e^{i\omega_2 T_0} - A_1 e^{i\omega_1 T_0})$$
$$-\alpha_1 A_1^3 e^{3i\omega_1 T_0} - 3\alpha_1 A_1^2 \bar{A}_1 e^{i\omega_1 T_0} - \mu_3[(i\omega_1 A_1 e^{i\omega_1 T_0}) | i\omega_1 A_1 e^{i\omega_1 T_0}|]$$
$$+\frac{F}{2} e^{i(\Omega T_0 + \tau_1)} + \rho_1 A_3^2 e^{2i\omega_3 T_0} + \rho_1 A_3 \bar{A}_3 + cc \tag{7.13}$$

$$D_0^2 u_{22} + \omega_2^2 u_{22} = -2i\omega_2 A_2' e^{i\omega_2 T_0} - 2\mu_2 i\omega_2 A_2 e^{i\omega_2 T_0} + \eta_2 k(A_2 e^{i\omega_2 T_0} - A_2 e^{i\omega_2 T_0})$$
$$-\alpha_2 A_1^3 e^{3i\omega_2 T_0} - 3\alpha_2 A_2^2 \bar{A}_2 e^{i\omega_2 T_0} - \mu_4[(i\omega_2 A_2 e^{i\omega_2 T_0}) | i\omega_2 A_2 e^{i\omega_2 T_0}|]$$
$$+\frac{F}{2} e^{i(\Omega T_0 + \tau_2)} + \rho_2 A_4^2 e^{2i\omega_4 T_0} + \rho_2 A_4 \bar{A}_4 + cc \tag{7.14}$$

$$D_0^2 u_{32} + \omega_3^2 u_{32} = \rho_3 A_1 A_3 e^{i(\omega_1 + \omega_3) T_0} - 2i\omega_3 A_3 \zeta_3 e^{i\omega_3 T_0} - 2i\omega_3 A_3' e^{i\omega_3 T_0}$$
$$+\rho_3 A_1 \bar{A}_3 e^{i(\omega_1 - \omega_3) T_0} + cc \tag{7.15}$$

$$D_0^2 u_{42} + \omega_4^2 u_{42} = \rho_4 A_2 A_4 e^{i(\omega_2 + \omega_4) T_0} - 2i\omega_4 A_4 \zeta_4 e^{i\omega_4 T_0} - 2i\omega_4 A_4' e^{i\omega_4 T_0}$$
$$+\rho_4 A_2 \bar{A}_4 e^{i(\omega_2 - \omega_4) T_0} + cc \tag{7.16}$$

where *cc* denotes the complex conjugate of the preceding terms. Eliminating the terms that produce secular terms in equations (7.13)–(7.16) yields

$$2i\omega_1 A_1' + 2\mu_1 i\omega_1 A_1 = \eta_1 k A_2 e^{i\sigma_2 T_1} - \eta_1 k A_1 - 3\alpha_1 A_1^2 \bar{A}_1 + \rho_1 A_3^2 e^{-i\delta_1 T_1}$$
$$+\frac{1}{2} F e^{i(\sigma_1 T_1 + \tau_1)} - i\frac{4}{3\pi} \mu_3 \omega_1^2 a_1^2 e^{i\beta_1} \tag{7.17}$$
$$2i\omega_2 A_2' + 2\mu_2 i\omega_2 A_2 = \eta_2 k A_1 e^{-i\sigma_2 T_1} - \eta_2 k A_2 - 3\alpha_2 A_2^2 \bar{A}_2 + \rho_2 A_4^2 e^{-i\delta_2 T_1}$$

$$+\frac{1}{2}Fe^{i(\sigma_1 T_1-\sigma_2 T_1+\tau_2)}-i\frac{4}{3\pi}\mu_4\omega_2^2 a_2^2 e^{i\beta_2} \tag{7.18}$$

$$2i\omega_3 A_3' + 2\zeta_3 i\omega_3 A_3 = \rho_3 A_1 \bar{A}_3 e^{i\delta_1 T_1} \tag{7.19}$$

$$2i\omega_4 A_4' + 2\zeta_4 i\omega_4 A_4 = \rho_4 A_2 \bar{A}_4 e^{i\delta_2 T_1} \tag{7.20}$$

Rewriting the A_n in terms of polar coordinates as

$$A_n = \frac{1}{2}a_n e^{i\beta_n} \tag{7.21}$$

and separating real and imaginary parts in equations (7.17) and (7.20), we obtain

$$a_1' = \frac{F}{2\omega_1}\sin\gamma_1 - \mu_1 a_1 + \frac{\eta_1 k a_2}{2\omega_1}\sin\gamma_2 - \frac{4\mu_3\omega_1}{3\pi}a_1^2 + \frac{\rho_1 a_3^2}{4\omega_1}\sin\gamma_3 \tag{7.22}$$

$$a_2' = -\frac{F}{2\omega_2}\sin(\tau_1-\tau_2-\gamma_1+\gamma_2) - \frac{\eta_2 k a_1}{2\omega_2}\sin\gamma_2 - \mu_2 a_2 - \frac{4\mu_4\omega_2}{3\pi}a_2^2 + \frac{\rho_2 a_4^2}{4\omega_2}\sin\gamma_4 \tag{7.23}$$

$$a_3' = -\frac{\rho_3 a_1 a_3}{4\omega_3}\sin\gamma_3 - \zeta_3 a_3 \tag{7.24}$$

$$a_4' = -\frac{\rho_4 a_2 a_4}{4\omega_4}\sin\gamma_4 - \zeta_4 a_4 \tag{7.25}$$

$$\gamma_1' = \sigma_1 - \frac{\eta_1 k}{2\omega_1} + \frac{F}{2\omega_1 a_1}\cos\gamma_1 - \frac{3\alpha_1}{8\omega_1}a_1^2 + \frac{\eta_1 k a_2}{2\omega_1 a_1}\cos\gamma_2 + \frac{\rho_1 a_3^2}{4\omega_1 a_1}\cos\gamma_3 \tag{7.26}$$

$$\gamma_2' = \sigma_2 - \frac{\eta_1 k}{2\omega_1} + \frac{\eta_2 k}{2\omega_2} + \frac{F}{2\omega_1 a_1}\cos\gamma_1 - \frac{3\alpha_1}{8\omega_1}a_1^2 - \frac{F}{2\omega_2 a_2}\cos(\tau_1-\tau_2-\gamma_1+\gamma_2) - \frac{\eta_2 k a_1}{2\omega_2 a_2}\cos\gamma_2 + \frac{\eta_1 k a_2}{2\omega_1 a_1}\cos\gamma_2 + \frac{3\alpha_2}{8\omega_2}a_2^2 + \frac{\rho_1 a_3^2}{4\omega_1 a_1}\cos\gamma_3 - \frac{\rho_2 a_4^2}{4\omega_2 a_2}\cos\gamma_4 \tag{7.27}$$

$$\gamma_3' = -\delta_1 - \frac{k\eta_1}{2\omega_1} + \frac{F}{2\omega_1 a_1}\cos\gamma_1 - \frac{3\alpha_1}{8\omega_1}a_1^2 + \frac{\eta_1 k a_2}{2\omega_1 a_1}\cos\gamma_2 - \frac{\rho_3 a_1}{2\omega_3}\cos\gamma_3 + \frac{\rho_1 a_3^2}{4\omega_1 a_1}\cos\gamma_3 \tag{7.28}$$

$$\gamma_4' = -\delta_2 - \frac{k\eta_2}{2\omega_2} + \frac{F}{2\omega_2 a_2}\cos(\tau_1-\tau_2-\gamma_1+\gamma_2) + \frac{k\eta_2 a_1}{2\omega_2 a_2}\cos\gamma_2 - \frac{3\alpha_2 a_2^2}{8\omega_2} - \frac{\rho_4 a_2}{2\omega_4}\cos\gamma_4 + \frac{\rho_2 a_4^2}{4\omega_2 a_2}\cos\gamma_4 \tag{7.29}$$

where

$$\gamma_1 = \sigma_1 T_1 + \tau_1 - \beta_1,\ \gamma_2 = \sigma_2 T_1 - \beta_1 + \beta_2$$
$$\gamma_3 = -\delta_1 T_1 - \beta_1 + 2\beta_3,\ \gamma_4 = -\delta_2 T_1 - \beta_2 + 2\beta_4 \tag{7.30}$$

7.3 Performance of the control law

The performance of the control technique was evaluated by calculating the equilibrium solutions of equations (7.17)–(7.20) and examining their stability as a function of the parameters F and σ_1 and the gains ρ_i. To determine the stability of the solutions of equations (7.17)–(7.20). We introduce the Cartesian transformation and separate the real and imaginary parts in equations (7.17)–(7.20), and obtain

$$A_k = \frac{1}{2}[p_k(T_1) - iq_k(T_1)]e^{(i\nu_k T_1 + \frac{\tau_k}{2})}, \qquad k = 1, 2 \tag{7.31}$$

where

$$\nu_1 = \sigma_1,\ \nu_2 = \sigma_1 - \sigma_2,\ \nu_3 = \frac{1}{2}\delta_1 + \sigma_1,\ \nu_4 = \frac{1}{2}\delta_2 + \sigma_1 - \sigma_2$$

and obtain

$$\begin{aligned}
p_1' =& -\mu_1 p_1 + \frac{1}{2\omega_1}\eta_1 k q_1 - \nu_1 q_1 + \frac{3}{8\omega_1}\alpha_1 p_1^2 q_1 + \frac{3}{8\omega_1}\alpha_1 q_1^3 - \frac{1}{2\omega_1}\eta_1 k q_2 - \frac{4}{3\pi}\mu_3\omega_1\sqrt{p_1^2+q_1^2}\,p_1 \\
& - \frac{\rho_1}{2\omega_1}p_3 q_3 \qquad (7.32)\\
q_1' =& \frac{1}{2\omega_1}F - \frac{1}{2\omega_1}\eta_1 k p_1 + \nu_1 p_1 - \frac{3}{8\omega_1}\alpha_1 p_1^3 + \frac{1}{2\omega_1}\eta_1 k p_2 - \mu_1 q_1 - \frac{4}{3\pi}\mu_3\omega_1\sqrt{p_1^2+q_1^2}\,q_1 \\
& - \frac{3}{8\omega_1}\alpha_1 p_1 q_1^2 + \frac{\rho_1}{4\omega_1}p_3^2 - \frac{\rho_1}{4\omega_1}q_3^2 \qquad (7.33)\\
p_2' =& -\mu_2 p_2 + \frac{1}{2\omega_1}\eta_2 k q_1 - 4k\eta_2 q_2 - \nu_2 q_2 + \frac{3}{8\omega_2}\alpha_2 p_2^2 q_2 \\
& + \frac{3}{8\omega_2}\alpha_2 q_2^3 - \frac{4}{3\pi}\mu_3\omega_1\sqrt{p_1^2+q_1^2}\,p_1 - \frac{\rho_2}{2\omega_2}p_4 q_4 \qquad (7.34)\\
q_2' =& \frac{1}{2\omega_2}F + \frac{1}{2\omega_2}\eta_2 k p_1 - \frac{1}{2\omega_2}\eta_2 k p_2 + \nu_2 p_2 - \frac{3}{8\omega_2}\alpha_2 p_2^3 - \mu_2 q_2 - \frac{4}{3\pi}\mu_4\omega_2\sqrt{p_2^2+q_2^2}\,q_2 \\
& - \frac{3}{8\omega_2}\alpha_2 p_2 q_2^2 + \frac{\rho_2}{4\omega_2}p_4^2 - \frac{\rho_2}{4\omega_2}q_4^2 \qquad (7.35)\\
p_3' =& -\zeta_3 p_3 - \frac{\rho_3}{4\omega_3}p_3 q_1 - \nu_3 q_3 + \frac{\rho_3}{4\omega_3}p_1 q_3 \qquad (7.36)\\
q_3' =& \nu_3 p_3 + \frac{\rho_3}{4\omega_3}p_1 p_3 - \zeta_3 q_3 + \frac{\rho_3}{4\omega_3}q_1 q_3 \qquad (7.37)\\
p_4' =& -\zeta_4 p_4 - \frac{\rho_4}{4\omega_4}p_4 q_2 - \nu_4 q_4 + \frac{\rho_4}{4\omega_4}p_2 q_4 \qquad (7.38)\\
q_4' =& \nu_4 p_4 + \frac{\rho_4}{4\omega_4}p_2 p_4 - \zeta_4 q_4 + \frac{\rho_4}{4\omega_4}q_2 q_4 \qquad (7.39)
\end{aligned}$$

The performance of the control was evaluated by calculating the equilibrium solutions of equations (7.32)–(7.39) and examining their stability as a function of the frequency of excitation and the gains ρ_i. Thus, we set the time derivatives in equations (7.32)–(7.39) equal to zero and solved the resulting system of algebraic equations for the p_i and q_i for a specified value of one of the parameters. The amplitudes a_1, a_2, a_3, and a_4 of the responses of the two tails and the two filters were then calculated from $a_i = \sqrt{p_i^2 + q_i^2}$. Since there is no closed-form solution for the eight algebraic equations, we resorted to numerical techniques. Numerical integration of the modulation equations for different sets of initial conditions was used to locate some of the possible solutions for a given frequency and amplitude of excitation. Then, starting with these solutions, we used a pseudo-arclength scheme [60] to trace the branches of the equilibrium solutions by varying the excitation frequency.

The stability of a particular equilibrium solution was determined by examining the eigenvalues of the Jacobian matrix of the right-hand sides of equations (7.32)–(7.39). If the real part of every eigenvalue is negative, the corresponding equilibrium solution is asymptotically stable. If the real part of any of the eigenvalues is positive, the corresponding equilibrium solution is unstable. In the next two sections, we present the stability analysis and evaluation of the control law.

7.4 Theoretical Frequency-Response Curves

Figure 5.1 shows frequency-response curves for the open-loop case for various levels of the excitation amplitude. In the next two sections, we assume that the excitation amplitude is $3.3g$, (i.e., we operate on curve (c) in Figure 5.1).

Figures 7.1 and 7.2 show frequency-response curves of the two tails and the two absorbers. The frequencies of the absorbers were automatically tuned one-half the excitation frequency. To theoretically implement this, for example for the right tail, we set $\Omega = \omega_1 + \sigma_1$ and $2\omega_3 = \omega_1 - \sigma_3$, where Ω is the excitation frequency, ω_1 is the natural frequency of the right tail, and ω_3 is the frequency of the absorber. The latter is tuned to the response frequency

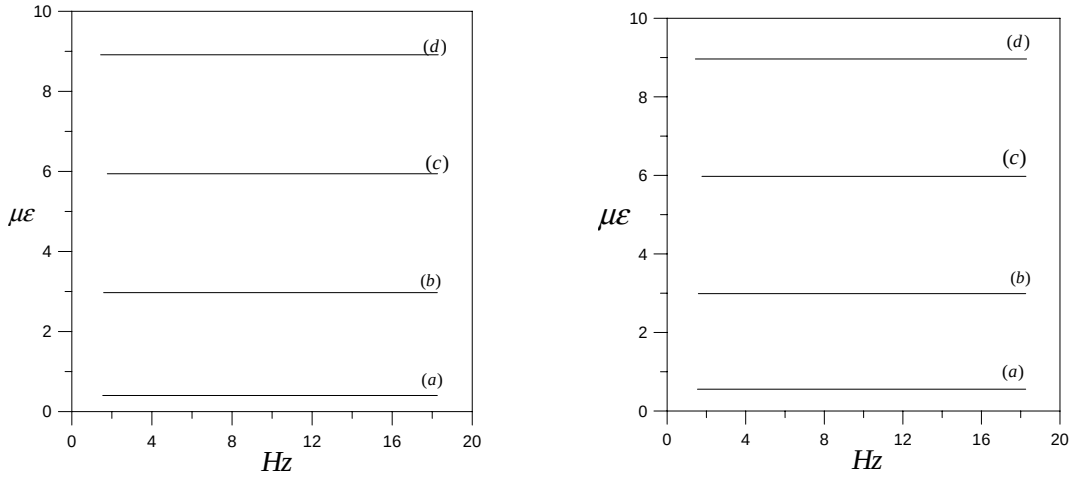

(i) right tail (ii) left tail

Figure 7.1: Effect of varying the damping ratios of the two absorbers on the frequency-response curves of the two tails (F=3.3g, G_i = 1): a) $\zeta_{3,4}$=0.01, b) $\zeta_{3,4}$=0.1, c) $\zeta_{3,4}$=0.2 , and d) $\zeta_{3,4}$=0.3.

of the first mode of the right tail. If we set $\sigma_3 = \sigma_1$ (i.e., twice the absorber frequency is equal to the excitation frequency) during a frequency sweep, we obtain Figure 7.1 (i). A similar analysis was done for the left tail (Figure 7.1 (ii)). We note that σ_2 is fixed to be to $\omega_2 - \omega_1 = 0.085$Hz.

Figures 7.3 and 7.4 show the effect of varying the feedback gain on the responses of the tails and the absorbers. These figures were obtained while tuning the frequencies of the absorbers to be equal to one-half the excitation frequency (i.e., $\omega_3 = \omega_4 = \frac{1}{2}\Omega$) and a damping ratio $\zeta_{3,4} = 0.2$. As the gain was increased, the responses of the tails and the absorbers decreased. However, since the control force was generated by the tail vibration itself, the controller vibration amplitude can never approach zero.

Figures 7.5 and 7.6 show the effect of detuning the absorbers' frequency away from one-half the excitation frequency. As can be seen, the response of the tails degrade when $\omega_{abs} = \frac{1}{2}\Omega - 2$. We also expect the behavior to keep degrading the more the detuning is. Thus the

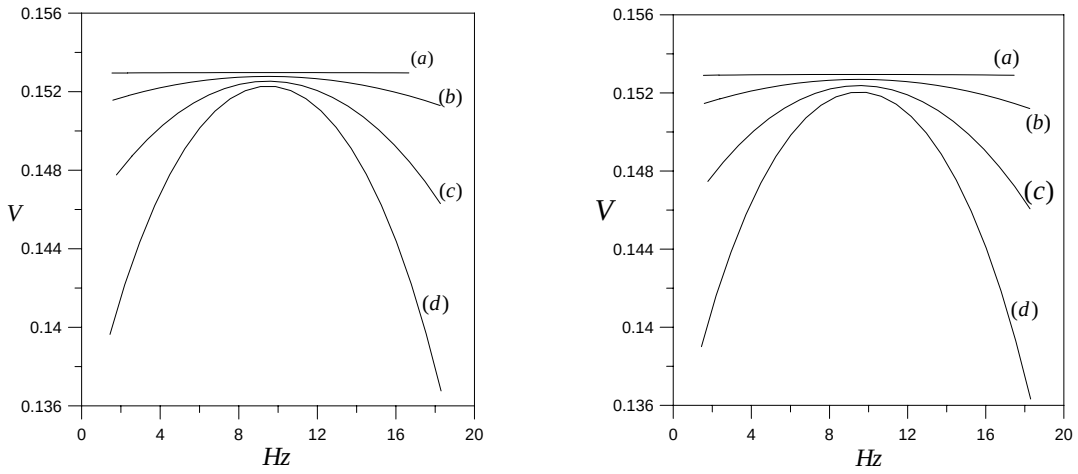

(i) right tail (ii) left tail

Figure 7.2: Effect of varying the damping ratios of the two absorbers on their frequency-response curves (F=3.3 $g, G_i = 1$): a) $\zeta_{3,4}$=0.01, b) $\zeta_{3,4}$=0.1, c) $\zeta_{3,4}$=0.2, and d) $\zeta_{3,4}$=0.3.

implementation of the technique is rendered very effective by tuning the frequency of the absorber equal to the frequency of oscillation of the tail.

7.5 Theoretical Force-Response Curves

In Figures 7.7 and 7.8, we show the closed-loop force-response curves of the two tails and the two absorbers. These figures illustrate the well-known saturation phenomenon. Where the response of the directly excited mode does not vary with the excitation amplitude. In fact, the value of the amplitude is kept fixed. We note that the response amplitude of the tails depend on the damping and the external detuning in the system. Figure 7.7 is generated for a damping ratio of $\zeta_{3,4}$=0.01 of the quadratic absorbers and perfect tuning (natural frequency of the absorber is set equal to one-half the excitation frequency). In fact, as the damping ratio of the absorbers increase, the response of the tails increase. This can be explained by mentioning that as the damping ratio of the absorbers increase, it takes more forcing of the

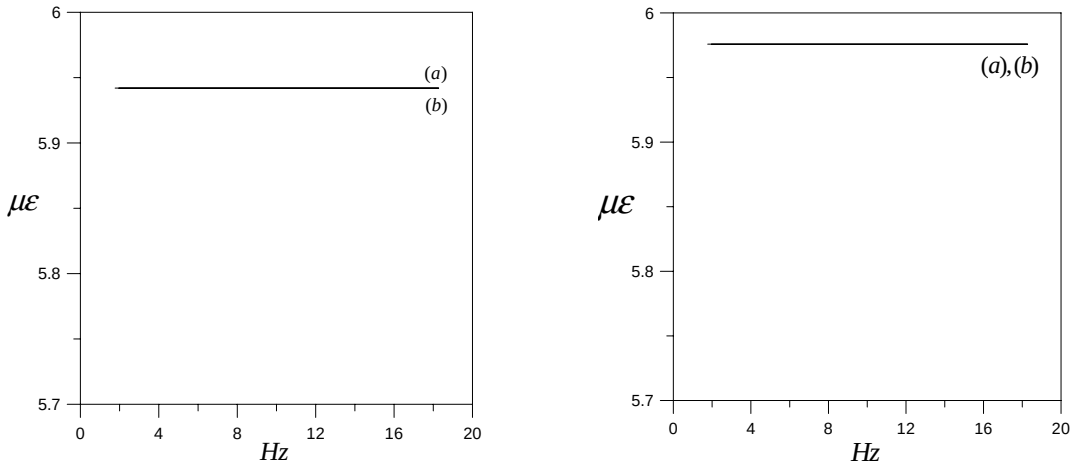

(i) right tail (ii) left tail

Figure 7.3: Effect of varying the feedback gain on the frequency-response curves of the two tails when their frequencies are fixed ($\zeta_{3,4}$=0.2, F=3.3g): a) G=1 and b) G=0.5.

tails for the energy to channel from the tails to the absorbers.

7.6 Experimental Results

Figure 7.9 shows the experimental setup. The maximum tail vibration achieved with the PZT actuators was $0.33V \approx 62\mu\epsilon$, which is in the linear response range of the tails (refer to Figure 5.1). The conversion follows the following equation

$$\mu\epsilon = \frac{4V_{out}}{10 \times 1000 \times 2.12 \times 10^{-6}} \tag{7.40}$$

where 10 is the bridge excitation, 1000 is the amplifier gain, and 2.12 is the gage factor.

Figure 5.8 and Figure 7.10 show the time histories and the FFT of the open- and closed-loop responses of the right tail. Similar results were obtained for the left tail. It is clear that the amplitudes of the responses are reduced by almost 10 times.

Figure 7.11 shows the control signal sent to the power amplifier, which in turn was sent to the

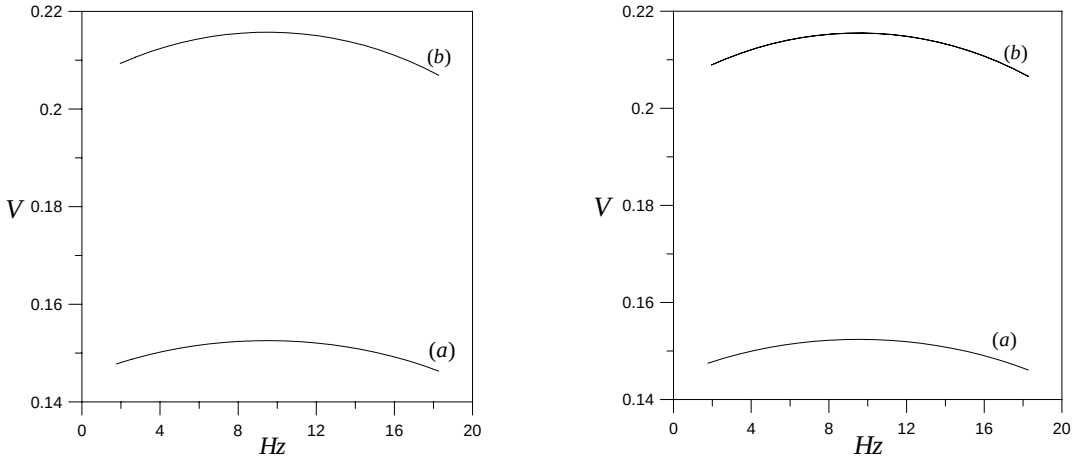

(i) right tail (ii) left tail

Figure 7.4: Effect of varying the feedback gain on the frequency-response curves of the two absorbers when their frequencies are fixed ($\zeta_{3,4}$=0.2, F=3.3g): a) G=1 and b) G=0.5.

PZT actuators. We note that there is a DC offset of the signal due to squaring the coupling term. In fact, this DC term is not desirable from the standpoint of the piezo amplifier.

7.7 Power Requirements

In this section, we follow the analysis of Oueini *et al.* [80] to compare the performance of the quadratic absorber with that of a linear tuned absorber. First, we write the closed-loop governing equations for both techniques applied to the right tail. A similar analysis can be done for the left tail. The right tail dynamics is governed by:

$$\ddot{u}_1 + \omega_1^2 u_1 + 2\epsilon\mu_1\dot{u}_1 + \epsilon\alpha_1 u_1^3 + \epsilon\mu_3\dot{u}_1 \mid \dot{u}_1 \mid -\epsilon k(u_2 - u_1) = \epsilon F\cos(\Omega t + \tau) + K_a F_c(t) \quad (7.41)$$

The linear absorber equation is governed by:

$$\ddot{u}_3 + \omega_3^2 u_3 + 2\epsilon\zeta_3\dot{u}_3 = \epsilon\rho_3 u_1 \quad \text{and} \quad F_c(t) = u_3 \quad (7.42)$$

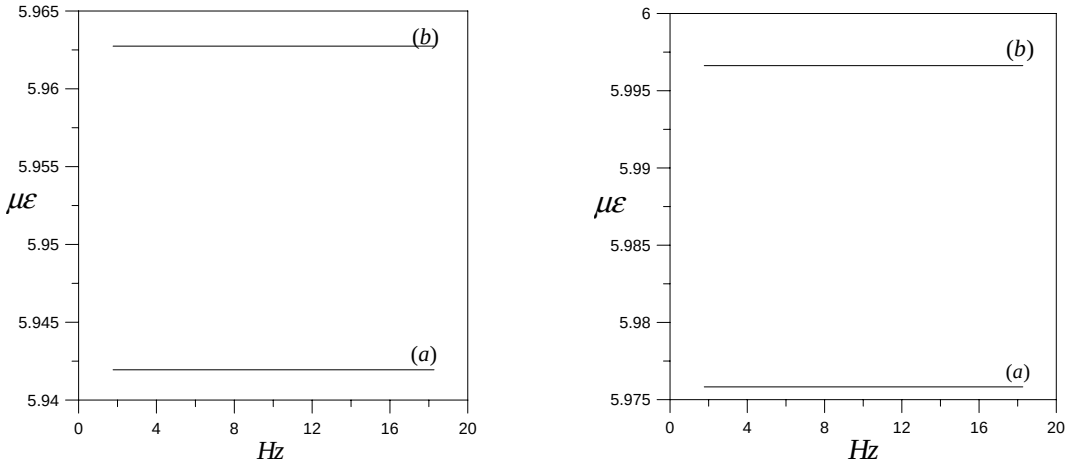

(i) right tail (ii) left tail

Figure 7.5: Effect of detuning the absorber frequency on the frequency-response curves of the two tails when their frequencies are fixed (F=3.3 g): a) $w_{3,4} = \frac{1}{2}\Omega$ and b) $w_{3,4} = \frac{1}{2}\Omega - 2$

The quadratic absorber equation is governed by:

$$\ddot{u}_4 + \omega_4^2 u_4 + 2\epsilon\zeta_4\dot{u}_4 = \epsilon\rho_4 u_1 u_4 \quad \text{and} \quad F_c(t) = u_3^2 \tag{7.43}$$

whereK_a is a constant gain that is dependent on the actuator and amplifier parameters and $F_c(t)$ is a control signal. For a perfectly controlled plant (i.e., $u_1 = 0$), the stroke of each absorber is given by:

$$v_1 \;=\; -\frac{1}{K_a} F\cos(\omega t + \tau) \quad \text{and} \quad v_2 \;=\; \sqrt{\frac{1}{K_a} F\cos(\omega t + \tau)}. \tag{7.44}$$

If the actuators are piezoceramics, then the voltage signals given by

$$V_1 \;=\; -\frac{1}{K_a} F\cos(\omega t + \tau) \quad \text{and} \quad V_2 \;=\; -\frac{2}{K_a} F\cos\left((\frac{1}{2}\omega t + \frac{1}{2}\tau)\right)^2. \tag{7.45}$$

The instantaneous power is defined by

$$P_i \;=\; V_i\, I_i \quad \text{for} \quad i = 1, 2. \tag{7.46}$$

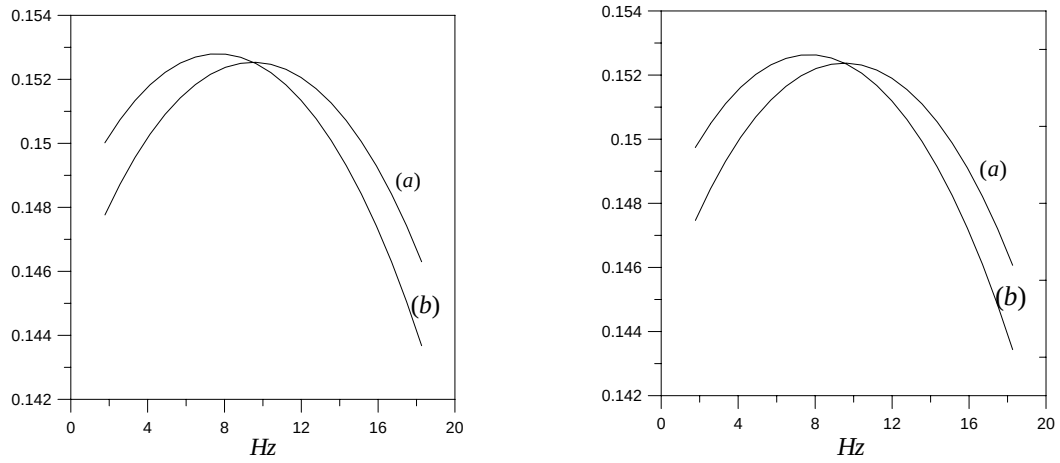

(i) right tail (ii) left tail

Figure 7.6: Effect of detuning the two absorber frequencies on their frequency-response curves when their frequencies are fixed(F=3.3 g): a) $w_{3,4} = \frac{1}{2}\Omega$, b) $w_{3,4} = \frac{1}{2}\Omega - 2$

Here, V_i is the control voltage, and the resulting current I_i is given by

$$I_i \;=\; C\,\frac{dV_i}{dt}, \tag{7.47}$$

where C is the effective capacitance of the actuators. Substituting equations (7.45) into equations (7.46) and (7.47), we obtain, after trigonometric manipulations,

$$P_1 \;=\; -\frac{C\,F^2\,\Omega}{2\,K_a^2}\sin(2\Omega t + 2\tau) P_2 \;=\; -\frac{C\,F^2\,\Omega}{2\,K_a^2}\sin(2\Omega t + 2\tau) - \frac{C\,F^2\,\Omega}{K_a^2}\sin(\Omega t + \tau). \tag{7.48}$$

In Figure 7.12, we illustrate the instantaneous power calculated from equation (7.48). The figure indicates that the quadratic absorber is almost twice that of the linear technique.

7.8 Summary

A saturation-based control law was used to suppress the vibrations of the first bending modes of the twin tails of a 1/16 structural dynamic model of an F-15 twin-tail assembly

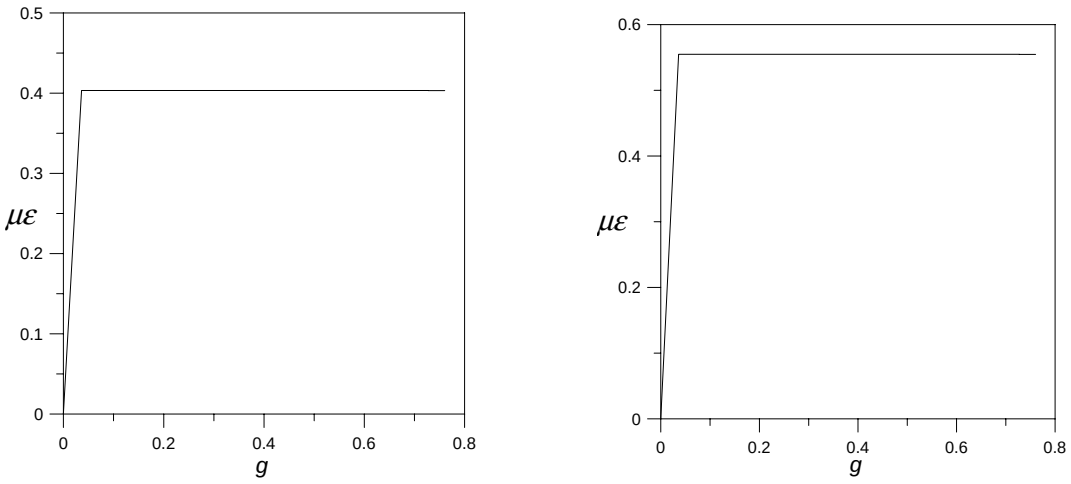

(i) right tail (ii) left tail

Figure 7.7: Force-response curves of the two tails (freq=9.135 Hz, $\zeta_{3,4}$=0.01)

when subjected to primary excitations. The dynamics of the first flexural modes of the twin tails are modeled by two second-order coupled nonlinear ordinary-differential equations. A filter is coupled linearly to one of the tails. The method of multiple scales is used to derive eight first-order differential equations governing the amplitudes and phases of the response. Then a bifurcation analysis is conducted to examine the stability of the closed loop system and investigate the performance of the control law. The control eliminates all multiple responses. The amplitudes of oscillation of the tails decrease tremendously. Once the absorbers frequencies are properly tuned, we show that the control scheme possesses a wide suppression bandwidth. Also, a parametric investigation was carried out to see the effect of changing the damping ratio of the absorber, the value of the feedback gain and the effect of detuning the frequencies of the absorbers in the response of the tails. To verify the theoretical analysis, experiments are done on the structural model of the twin-tail assembly fitted with piezoceramic actuators. We implement the absorber using a digital signal processing (DSP) device. Good agreement between theory and experiments is found.

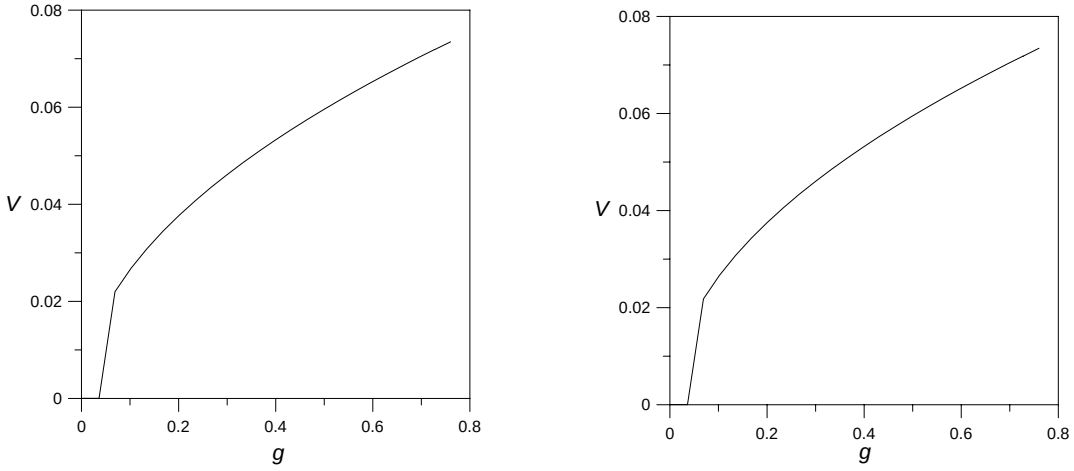

(i) right tail (ii) left tail

Figure 7.8: Force-response curves of the two absorbers (freq=9.135 Hz, $\zeta_{3,4}$=0.01)

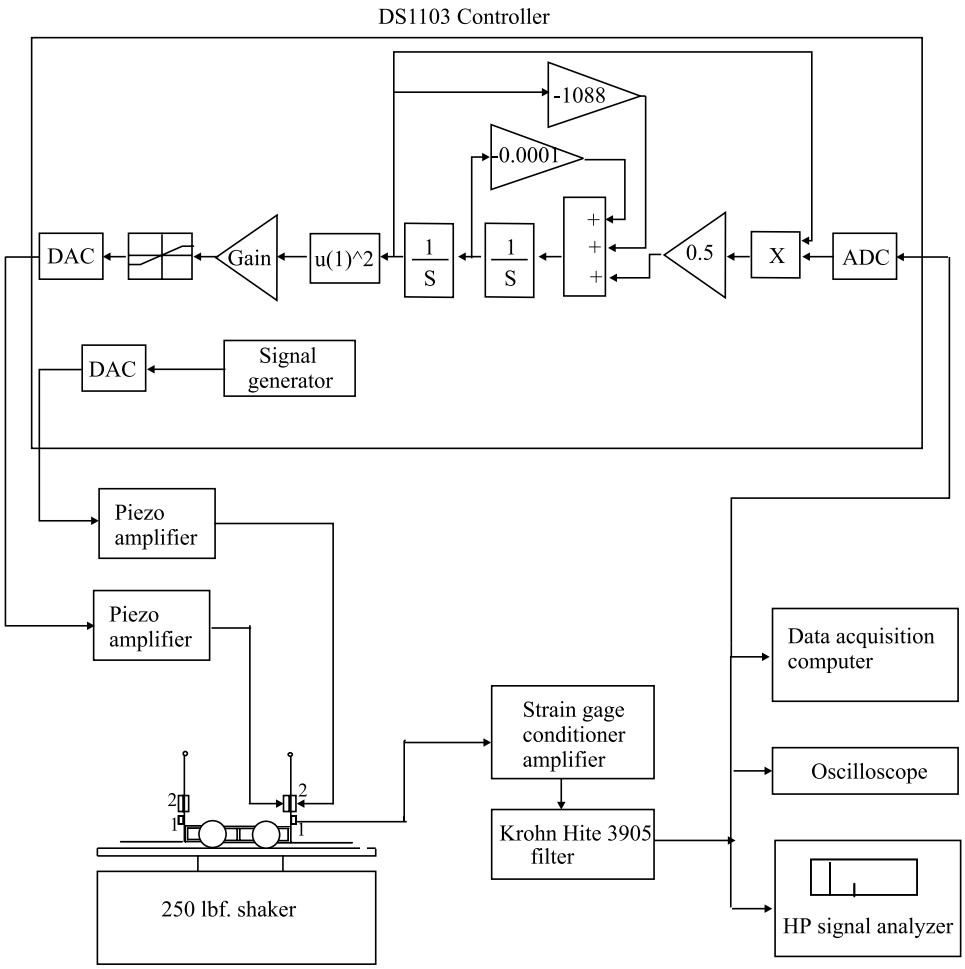

Figure 7.9: Experimental setup.

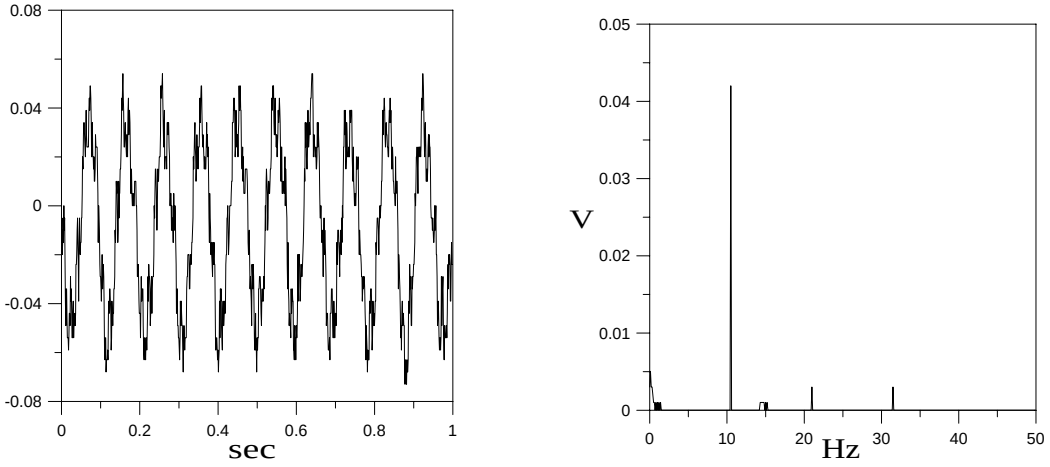

(i) time domain (ii) frequency domain

Figure 7.10: Response of the right tail with the quadratic absorber activated ($\zeta_{3,4} = 0.1$)

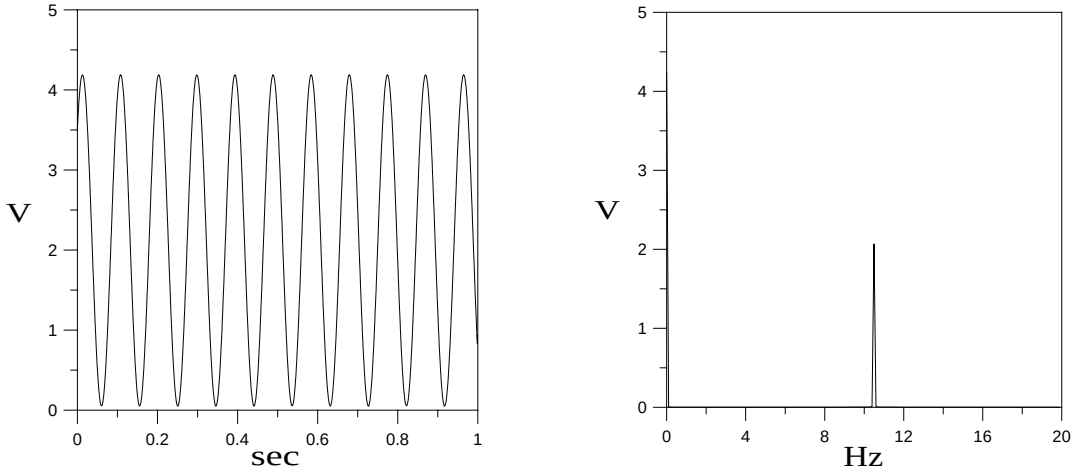

(i) time domain (ii) frequency domain

Figure 7.11: Control signal.

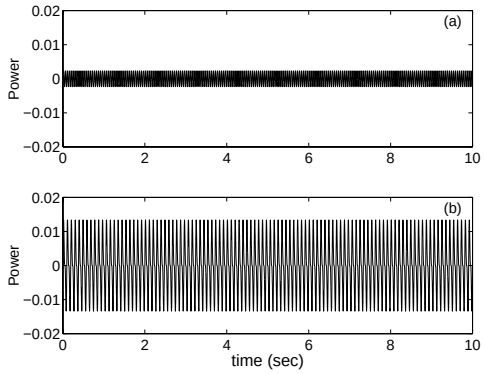

Figure 7.12: Time traces of the instantaneous power. (a) Linear absorber and (b) quadratic absorber.

Chapter 8

Concluding Remarks

8.1 Summary

We developed a mathematical model that describes the structural dynamic behavior of a 1/16 scale model of the F-15 aircraft subjected to either principal parametric or primary external excitations. The model consists of two oscillators, each of which has linear and quadratic damping terms and a cubic nonlinear term. The two oscillators are coupled linearly. All of the parameters of the equations were identified using experimental modal analysis and nonlinear identification techniques. Experimental force- and frequency-response curves were obtained. Good agreement between the experimental and theoretical results was achieved. Description of the different responses was also presented.

Since in the case of parametric excitation, adding damping to the tails will not limit the amplitudes of oscillation once the threshold excitation level is exceeded, we used a nonlinear control law based on feeding back the cube of the velocity to suppress the first-mode vibrations. We employed a controller for each tail and thus reduced the interaction between them. The application of the control law reduced the range of frequencies for which the oscillations are high. Also, increasing the gain decreased the steady-state oscillation amplitudes of as well as improved the transient performance. All of the theoretical results were verified using

experiments.

The application of neural networks was also studied and the use of model reference adaptive control was applied to the scale model. To control the system, we trained a neural network emulator to learn the mapping between the control signal and the response of the tails. Then, the neurocontroller learned how to control the structure with the help of this emulator network. Numerical simulations proved the technique to be effective in alleviating high-amplitude vibrations of the model.

For the case of direct excitation, we developed and investigated the application of four different active buffet-alleviation systems: the use of linear and nonlinear velocity feedback and linear and quadratic absorbers. For the different cases, we employed perturbation methods and modern nonlinear dynamics to find the general nonlinear response of the model and to analyze the performance of the different control laws. Moreover, we performed experiments using piezceramic actuators to confirm and validate the theoretical studies.

For the case of feedback control, it was shown that both techniques are effective in reducing the tail vibrations as well as eliminating all multiple responses. Also, the oscillation amplitudes decreased as the feedback gain was increased. Unlike the linear velocity feedback control, the nonlinear law kept the response of the tails nonlinear even for small amplitudes. To compare the power requirements of the two control techniques, we implemented them on a simple system. The analysis shows that the linear velocity feedback control uses less power than the cubic velocity feedback control. From this analysis, we concluded that the use of linear velocity feedback is preferrable than the nonlinear control law. However, Experimental results showed that only a 50 % reduction was achievable before saturating the actuators.

Two different absorbers, linear and quadratic, were also implemented to suppress the vibrations of the tails subjected to primary external excitations. In both cases, the response amplitudes were reduced by almost 10 times, thus improving on the feedback techniques. However, this happens at the expense of complicating the system by doubling the equations of motion. In each case, a filter was coupled to every tail. Once the absorbers frequencies were properly tuned, both control schemes possessed wide suppression bandwidths. The

difference between the two techniques was clear in the force-response curves. For the case of the linear absorber, increasing the excitation amplitude lead to an increase in the response level. However, for the case of the quadratic absorber, the responses did not increase as the excitation amplitude was increased. That was due to the saturation phenomenon resulting from nonlinearly coupling the tails to the absorbers. We compared the power requirements for the two control techniques. The analysis showed that the linear absorber uses less power than the quadratic absorber. However, the experiments revealed the nonlinear law is globally stable, unlike the linear absorber, where increasing the the feedback gain may lead to instability. This all shows that each control law has its advantages and disadvantages, which need to be taken into consideration before applying any of them. A better technique might be the use of a hybrid controller that uses the best of all worlds. However, this will complicate the control law because it would require switching on the different control laws where they perform the best.

8.2 Future Work

The work presented in this Dissertation can be expanded and enhanced by undertaking the following tasks:

- Some means of providing a hard direct excitation to the F-15 scale model should be implemented in order to validate theoretical analysis.
- Nonlinear mathematical models should be developed for the other significant modes, such as the first torsional and second bending modes. Coupling between the same modes of one tail and their interaction with modes of the other tail should be investigated.
- Different combination and subcombination resonances should be studied and their effects, if any, should be documented.
- The interaction between the horizontal stabilizors and the vertical tails should also be investigated.

- Experiments to validate the neural network control model should be implemented.
- Experiments to show the feasibility of controlling the buffet-induced vibrations during high-angle-of-attack operations on an aeroelastically scaled model in the wind-tunnel should be implemented.
- Testing a full-scale model is a logical step for such work.
- Analysis and selection of piezoceramic actuators that can have enough control authority should be performed.
- To better implement the control laws digitally on DSP processors, and to identify the lowest order of time integration and smallest frequency at which the controller can be implemented to insure both stability and efficiency, a sampled-data formulation of the nonlinear differential equations that govern the model and the control law should be developed.
- The buffet-alleviation system should be tested on other twin-tail aircraft, such as the F-18, to generalize its use to all high-performance twin-tail aircraft.
- Other control strategies, such as Linear Quadratic Control (LQR) and H_∞, should be compared with those studied here.
- The control of multi-input, multi-output systems should be considered and a method for obtaining the influence matrix of the control sensors should be considered to best locate the sensors.
- A study of the robustness of the different control strategies for multi-degree-of-freedom systems should be performed to determine the bounds on system uncertainities that will maintain closed-loop stability and performance.
- Another research area for the different active control techniques is the study of transient effects, such as overshoots and settling times.
- Stability and robustness analysis should be implemented on the discretized system.
- Adaptive or time-varying controllers should also be implemented to alleviate buffeting due to different flight conditions of dynamic maneuvers.

- Optimization studies to size the dimensions of the piezoceramic actuators should be performed. This optimization should maximize the transfer of energy from a piezoceramic actuator to the tail structure while minimizing the local stresses at the location of the actuator. Further weight optimization could be performed by studying the shape of the actuator.
- A study of the stress redistribution in the controlled tails due to the presence of the actuators under closed-loop conditions should be performed to insure that the stresses are not locally increased in a manner that generates new fatigue critical areas.

Bibliography

[1] Y. C. Fung, *An Introduction to the Theory of Aeroelasticity.* Dover Publications, New York, 1955.

[2] R. L. Bisplinghoff, H. Ashley, and R. L. Halfman, *Aeroelasicity.* Addison-Wesley, Cambridge, Mass., 1955.

[3] A. H. Nayfeh, M. R. Hajj, J. Fung, and S. O. Fahey, "Characterization and identification of damping and nonlinear systems parameters with bispectral analysis," in *ASME Design Engineering Technical Conferences*, ASME DETC97/VIB-4407, (Sacramento, CA), September 14-17 1997.

[4] M. A. Ferman, S. L. Liguore, C. M. Smith, and B. J. Colvin, "Composite "exoskin" doubler extends f-15 vertical tail fatigue life," 1993. AIAA paper No. 93-1341-CP.

[5] I. Gursul and W. Xie, "Buffeting flows over delta wings," *AIAA Journal*, vol. 37, pp. 58–65, 1999.

[6] M. A. Ferman, S. R. Patel, N. H. Zimmerman, and G. Gerstenkorn, "A unified approach to buffet response of fighter aircraft empennage," in *NATO/AGARD 70th Structures and Material Panel*, (Sorrento, Italy), 2–4 April 1990.

[7] W. E. Triplett, "Pressure measurments on twin vertical tails in buffeting flow," 1982. AIAA Paper No. 82–0641.

[8] W. L. Sellers, J. F. Meyers, and T. E. Hepner, "Ldv surveys over a fighter model at moderate to high angles of attack," 1988. Society of Automotive Engineers TP Series Paper 88–1448.

[9] N. H. Zimmerman, M. A. Ferman, R. N. Yurkovich, and G. Gerstenkorn, "Prediction of tail buffet loads for design applications," 1989. AIAA Paper No. 89–1378.

[10] S. W. Moss, S. R. Cole, and R. V. Doggett, Jr., "Some subsonic and transonic buffet characteristics of the twin-vertical-tails of a fighter airplane configuration," 1991. AIAA Paper No. 91–1049.

[11] N. M. Komerath, R. J. Schwartz, S. Percival, and J. M. Kim, "Unsteady vortex flow measurments over twin-tailed aircraft at high angles of attack," 1991. AIAA Paper No. 91–0279.

[12] A. E. Washburn, L. N. Jenkins, and M. A. Ferman, "Experimental investigation of vortex-fin interaction," 1993. AIAA Paper No. 93–0050.

[13] O. A. Kandil, H. A. Kandil, and S. J. Massey, "Simulation of tail buffet using delta wing-vertical tail configuration," 1993. AIAA Paper No. 93–3688.

[14] O. A. Kandil, S. J. Massey, and H. A. Kandil, "Computations of vortex-breakdown induced tail buffet undergoing bending and torsional vibrations," 1994. AIAA Paper No. 94–1428.

[15] O. A. Kandil, E. F. Sheta, and S. J. Massey, "Buffet responses of a vertical tail in vortex breakdown flows," 1995. AIAA Paper No. 95–3464.

[16] S. L. Krist, A. E. Washburn, and K. D. Visser, "A computational and experimental investigation of a delta wing with vertical tails," 1993. AIAA Paper No. 93–3009.

[17] P. Rizetta, "Numerical simulation of the interaction between a leading-edge vortex and a vertical tail," 1996. AIAA Paper No. 96–2012.

[18] S. A. Morton, D. P. Rizzetta, and R. B. Melville, "Numerical simulation of the interaction between a leading- edge vortex and a flexible vertical tail," 1998. AIAA Paper No. 98–1957.

[19] M. V. Lowson and A. J. Riley, "Vortex breakdown control by delta wing geometry," *Journal of Aircraft*, vol. 32, no. 4, pp. 58–65, 1995.

[20] I. Gursul, "Unsteady flow phenomena over delta wings at high angle of attack," *AIAA Journal*, vol. 32, no. 2, pp. 225–231, 1994.

[21] N. M. Komerath, S. G. Liou, R. J. Schwartz, and J. M. Kim, "Flow over a twin-tailed aircraft at angle-of-attack. part i: Spatial characteristics," *Journal of Aircraft*, vol. 29, no. 3, pp. 413–420, 1992.

[22] N. M. Komerath, R. J. Schwartz, and J. M. Kim, "Flow over a twin-tailed aircraft at angle-of-attack. part ii: Temporal characteristics," *Journal of Aircraft*, vol. 29, no. 4, pp. 553–558, 1992.

[23] J. P. Hubner and N. M. Komerath, "Spectral mapping of quasiperiodic structures in a vortex flow," *Journal of Aircraft*, vol. 32, no. 3, pp. 493–500, 1995.

[24] J. P. Hubner and N. M. Komerath, "Counter-rotating structures over a delta wing," *AIAA Journal*, vol. 34, no. 9, pp. 1958–1960, 1996.

[25] J. P. Hubner and N. M. Komerath, "Coherence-tracking of quasi-periodic structures in a vortex flow," 1993. AIAA Paper No. 93–2914.

[26] J. P. Hubner and N. M. Komerath, "Visualization of quasi-periodic structures in a vortex flow," 1994. AIAA Paper No. 94–0624.

[27] J. P. Hubner and N. M. Komerath, "Modification of spectral characteristics in a vortex flow field," 1995. AIAA Paper No. 95–1795.

[28] M. A. Klein, W. K. Lentz, and N. M. Komerath, "Reduction of fluctuations over swept wings using passive and active mini-fences," 1997. AIAA Paper No. 97–0548.

[29] K. Gee, S. M. Murman, and L. B. Schiff, "Computation of f/a-18 tail buffet," *Journal of Aircraft*, vol. 33, no. 6, pp. 1181–1189, 1996.

[30] B. Lee and D. Brown, "Wind tunnel studies of f/a-18 tail buffet," *Journal of Aircraft*, vol. 29, no. 1, pp. 146–152, 1992.

[31] S. K. Hebbar, M. F. Platzer, and W. D. Frink, "Effect of leading-edge extension fences on the vortex wake on an f/a-18 model," *Journal of Aircraft*, vol. 32, no. 3, pp. 680–682, 1995.

[32] L. A. Meyn and K. D. James, "Full-scale wind-tunnel studies of f/a-18 tail buffet," *Journal of Aircraft*, vol. 33, no. 3, pp. 589–595, 1996.

[33] C. L. Pettit, D. L. Brown, M. P. Banford, and E. Pendleton, "Full-scale wind-tunnel pressure measurments of an f/a-18 tail during buffet," *Journal of Aircraft*, vol. 33, no. 6, pp. 1148–1156, 1996.

[34] D. E. Bean, D. I. Greenwell, and N. J. Wood, "Vortex control technique for the attenuation of fin buffet," *Journal of Aircraft*, vol. 30, no. 6, pp. 847–853, 1993.

[35] D. E. Bean and N. J. Wood, "Experimental investigation of twin-fin buffeting and suppression," *Journal of Aircraft*, vol. 33, no. 4, pp. 761–767, 1996.

[36] K. Gee, Y. M. Rizk, and L. B. Schiff, "Forebody tangential slot blowing on an aircraft geometry," *Journal of Aircraft*, vol. 31, no. 4, pp. 922–928, 1994.

[37] E. F. Sheta, O. A. Kandil, and Z. Yang, "Effectiveness of flow control for alleviation of twin-tail buffet," 1998. AIAA Paper No. 98–5501.

[38] O. A. Kandil, Z. Yang, and E. F. Sheta, "Flow control and modification for alleviating twin-tail buffet," 1998. AIAA Paper No. 99–0138.

[39] S. Liguore, M. Ferman, and R. Yurkovich, "Integral damping treatment for primary aircraft structures," in *Damping '91 Conference*, (San Diego, Ca), February 13–15 1991.

[40] K. B. Lazarus, E. Saarmaa, and G. S. Agnes, "An active smart material system for buffet load alleviation," in *Smart Structures and Integrated Systems*, vol. 2447, pp. 179–192, 1995.

[41] J. W. Moore, R. L. Spangler, K. B. Lazarus, and D. A. Henderson, "Buffet load alleviation using distributed piezoelectric actuators," in *Proceedings of the ASME Aerospace Division*, vol. 52, pp. 485–490, 1996.

[42] R. L. Spangler Jr. and R. N. Jacques, "Testing of an active smart material system for buffet load alleviation," 1999. AIAA Paper No. 99–1316.

[43] R. M. Hauch, J. H. Jacobs, K. Ravindra, and C. Dima, "Reduction of vertical tail buffet response using active control," *Journal of Aircraft*, vol. 33, no. 3, pp. 617–622, 1996.

[44] F. Nitzsche, D. G. Zimcik, and K. Langille, "Active control of vertical fin buffeting with aerodynamic control surface and strain actuation," in *AIAA/ASME/AHS Adaptive Structures Forum*, (Kissimmee, Fl), pp. 1467–1477, April 7–10 1997.

[45] F. Nitzsche, D. G. Zimcik, T. G. Ryall, R. W. Moses, and D. A. Henderson, "Control law synthesis for vertical fin buffet alleviation using strain actuation," 1999. AIAA Paper No. 99–1317.

[46] R. W. Moses, "Vertical tail buffeting alleviation using piezoelectric actuators - some results of the actively controlled response of buffet-affected tails (acrobat) program," in *SPIE's 4th Annual Symposium on Smart Structures and Materials*, vol. 3044, pp. 87–98, 1997.

[47] R. W. Moses, "Contributions to active buffeting alleviation programs by the nasa langley research center," 1999. AIAA Paper No. 99–1318.

[48] L. E. Pado and P. F. Lichtenwalner, "Neural predictive control for active buffet alleviation," 1999. AIAA Paper No. 99–1319.

[49] S. Hanagud, M. Bayon de Noyer, H. Luo, D. Henderson, and K. S. Nagaraja, "Tail buffet alleviation of high performance twin tail aircraft using piezo-stack actuators," 1999. AIAA Paper No. 99–1320.

[50] M. Hopkins, R. Moses, D. Zimcik, D. Henderson, T. Ryall, and R. Spangler, "Active vibration suppression systems applied to twin tail buffeting," in *SPIE's Industrial and Commercial Applications of Smart Structures Technologies*, vol. 3326, pp. 27–33, 1998.

[51] M. T. Hagan, H. B. Demuth, and M. Beale, *Neural Network Design*. PWS publishing company, Boston, Ma., 1996.

[52] S. Chen, C. F. Cowan, and P. M. Grant, "Orthogonal least squares learning algorithm for radial basis function networks," *IEEE Transactions on Neural Networks*, vol. 2, no. 2, 1991.

[53] D. F. Specht, "A general regression neural network," *IEEE Transactions on Neural Networks*, vol. 2, no. 6, 1991.

[54] J. H. Jacobs, C. E. Hedgecock, P. F. Lichtenwalner, L. E. Pado, and A. E. Washburn, "The use of artificial intelligence for buffet environments," 1993. AIAA Paper No. 93–1534.

[55] L. E. Pado and R. D. Damle, "Predictive neuro control of vibration in smart structures," in *SPIE 1996 Symposium on Smart Structures and Materials*, vol. 2715, pp. 567–575, 1996.

[56] P. F. Lichtenwalner, G. R. Little, L. E. Pado, and R. C. Scott, "Adaptive neural control for active flutter suppression," in *ASME IMEC&E Conference*, (Atlanta, GA), November 1996.

[57] S. O. Fahey and A. H. Nayfeh, "Experimental nonlinear identification of a single structural mode," in *16th International Modal Analysis Conference*, (Santa Barbara, CA), February 3-5 1998.

[58] A. H. Nayfeh, *Perturbation Methods*. Wiley, New York, 1973.

[59] A. H. Nayfeh, *Introduction to Perturbation Techniques*. Wiley, New York, 1981.

[60] A. H. Nayfeh and B. Balachandran, *Applied Nonlinear Dynamics*. Wiley, New York, 1995.

[61] A. H. Nayfeh and D. T. Mook, *Nonlinear Oscillations*. Wiley, New York, 1979.

[62] S. S. Oueini and A. H. Nayfeh, "Control of a system under principal parametric excitation," in *The Fourth International Conference on Motion and Vibration Control*, vol. 2, (ETH Zurich, Switzerland), pp. 405–409, August 25-28 1998.

[63] P. Lisboa, *Neural Networks : Current Applications*. Chapman and Hall, New York, 1992.

[64] F. C. Fu and J. B. Farison, "On the volterra-series functional identification of nonlinear discrete-time systems," *Int.J. Control*, vol. 8, pp. 1281–1289, 1973.

[65] S. J. Farlow, *Self-Organizing Methods in Modeling; GMDH Type Algorithms*. Marcel Dekker, New York, 1984.

[66] J. Park and I. W. Sandberg, "Universal approximation using radial-basis function networks," *Neural Computation*, vol. 3, pp. 246–257, 1991.

[67] M. F. Tenorio and W. T. Lee, "Self-organizing neural nets for the identification problem," in *Advances in Neural Information Processing System Vol. 1* (D. Touretzky, ed.), 1989.

[68] K. Hornik, M. Stinchcombe, and H. White, "Multilayer feedforward networks are universal approximators," *Neural Networks*, vol. 2, pp. 359–366, 1989.

[69] K. S. Narendra and K. parthasarathy, "Neural networks in dynamical systems," *SPIE Intelligent Control and Adaptive Systems*, vol. 1196, pp. 230–241, 1989.

[70] K. S. Narendra and K. parthasarathy, "Identification and control of dynamic systems using neural networks," *IEEE Transactions on Neural Networks*, vol. 1, pp. 4–27, 1990.

[71] V. V. Chalam, *Adaptive Control System–Techniques and Applications*. Marcel Dekker, New York and Basel, 1987.

[72] S. M. Yang and G. S. Lee, "Vibration control of smart structures by using neural networks," *Journal of Dynamic Systems, Measurment and Control*, vol. 119, pp. 34–39, 1997.

[73] H. M. Chen, K. H. Tsai, G. Z. Qi, J. C. S. Yang, and F. Amini, "Neural network for structure control," *Journal of Computing in Civil Engineering*, vol. 9, pp. 168–175, 1995.

[74] G. F. Franklin, J. D. Powell, and M. L. Workman, *Digital Control of Dynamic Systems*. Addison-Wesley, 1990.

[75] The MathWorks, Natick, MA, *SIMULINK: Dynamic System Simulation Software*.

[76] *dSPACE Digital Signal Processing and Control Engineering*. GmbH, Paderborn, Germany.

[77] C. J. Goh and T. K. Caughey, "On the stability problem caused by finite actuator dynamcis in the collocated control of large space structures," *International Journal of Control*, vol. 41, pp. 787–802, 1985.

[78] J. N. Juang and M. Phan, "Robust controller designs for second-order dynamic systems: a virtual passive approach," *Journal of Guidance, Control, and Dynamics*, vol. 15, pp. 1192–1198, 1992.

[79] J. J. Hollkamp and T. F. Starchville, Jr., "A self-tuning piezoelectric vibration absorber," *Journal of Intelligent Material Systems and Structures*, vol. 5, pp. 559–566, 1994.

[80] S. S. Oueini and A. H. Nayfeh, "Analysis and application of a nonlinear vibration absorber," *Journal of Vibration and Control*, 2000. accepted for publication.

[81] J. L. Fanson and T. K. Caughey, "Positive position feedback control for large space structures," *AIAA Journal*, vol. 28, pp. 717–724, 1990.

[82] A. G. Haddow, A. D. S. Barr, and D. T. Mook, "Theoretical and experimental study of modal interaction in a two degree-of-freedom structure," *Journal of Sound and Vibration*, vol. 97, pp. 451–473, 1984.

[83] M. F. Golnaraghi, "Regulation of flexible structures via nonlinear coupling," *Journal of Dynamics and Control*, vol. 1, pp. 405–428, 1991.

[84] K. L. Tuer, M. F. Golnaraghi, and D. Wang, "Development of a generalized active vibration suppression strategy for a cantilever beam using internal resonance," *Nonlinear Dynamics*, vol. 5, pp. 131–151, 1994.

[85] S. S. Oueini and M. F. Golnaraghi, "Experimental implementation of the internal resonance control strategy," *Journal of Sound and Vibration*, vol. 191, pp. 377–396, 1996.

[86] S. S. Oueini, A. H. Nayfeh, and J. R. Pratt, "A nonlinear vibration absorber for flexible structures," *Nonlinear Dynamics*, vol. 15, pp. 259–282, 1998.

[87] P. F. Pai, B. Wen, A. S. Naser, and M. J. Schultz, "Structural vibration control using PZT patches and non-linear phenomena," *Journal of Sound and Vibration*, vol. 215, pp. 273–296, 1998.

[88] B. D. Hall, "Numerical simulations of the aeroelastic response of an actively controlled flexible wing," Master's thesis, Virginia Polytechnic Institute and State University, 1999.

Appendix A

Equilibrium Solutions and their Stability

The source of this appendix is [60]

A.1 Equilibrium Solutions

The equilibrium solutions or constant solutions of an autonomous system defined by

$$\dot{x} = \mathbf{F}(x; \mu) \tag{A.1}$$

where x is a state variables vector, $x_1, x_2, \ldots, x_n, n$ is an integer number, $\mathbf{F}$ is the field vector, and μ is the control parameter of the system, correspond to

$$\dot{x} = 0 \tag{A.2}$$

By equating the right-hand side of equation (A.1) to zero, we end up with either linear or nonlinear algebraic equations. If the function $\mathbf{F}$ in equation (A.1) is linear, then the system is linear. So, it has only one constant solution, namely, the trivial solution if the system matrix is nonsingular. In contrast, for a nonlinear system, there may be more than one constant or

equilibrium solution. Using a continuation scheme, presented later, we solve these equations as a function of the control parameter μ. The stability of this type of solution is discussed next.

A.1.1 Stability of Equilibrium Solutions

The stability of an equilibrium solution x_0 at $\mu = \mu_0$ depends on the eigenvalues of the Jacobian matrix $\mathbf{J}$ of the system (A.1), which is the matrix of first partial derivatives. Consider a small disturbance $\mathbf{y}$ to the equilibrium solution x_0, so that

$$x(t) = x_0 + y(t). \tag{A.3}$$

Substituting equation (A.3) into equation (A.1) gives

$$\dot{y} = \mathbf{F}(x_0 + y; \mu_0). \tag{A.4}$$

Using a Taylor series expansion around x_0 and keeping only the linear terms in y, one obtains

$$\dot{y} = \mathbf{F}(x_0; \mu_0) + \mathbf{D_x F}(x_0; \mu_0)y + \dots \tag{A.5}$$

However, at the equilibrium solution $\mathbf{x_0}$, $\mathbf{F}(\mathbf{x_0}; \mu_0) = 0$. So, equation (A.5) becomes

$$\dot{y} \approx \mathbf{D_x F}(\mathbf{x_0}; \mu_0)\mathbf{y} = \mathbf{J}\mathbf{y} \tag{A.6}$$

The eigenvalues of the constant matrix J provide information about the local stability of the equilibrium solution $\mathbf{X_0}$. An equilibrium solution is classified as hyperbolic or non-hyperbolic. If all of the eigenvalues of J have nonzero real parts, then the corresponding equilibrium solution is called a hyperbolic fixed point; Otherwise, it is called a nonhyperbolic fixed point. The hyperbolic fixed points are of three types: stable nodes, unstable nodes, and saddle points. A fixed point is called a stable node or a sink if all of the eigenvalues of J have negative real parts. If the matrix J associated with a stable node has complex eigenvalues, the stable node is called a stable focus. An equilibrium point is called an unstable node or a source if one or more of the eigenvalues of J have positive real parts. An unstable node is

called an unstable focus if the associated matrix J has complex eigenvalues. An equilibrium pont is a saddle if some, but not all, of the eigenvalues have positive real parts while the rest of them have negative real parts. On the other hand, a nonhyperbolic fixed point is unstable if one or more of the eigenvalues of J have positive real parts. It is said to be marginally stable if some of the eigenvalues of J have negative real parts while the rest of them have zero real parts. It is called a center if all the eigenvalues of J are purely imaginary and nonzero.

A.2 Bifurcations of Fixed Points

Local bifurcation is a qualitative change occuring in the neighborhood of a fixed point or a periodic solution of the system. When a single control parameter is varied, a fixed point of an autonomous system, such as the one given by (A.1), can lose stability through one of the following bifurcations: saddle-node bifurcation, pitchfork bifurcation, transcritical bifurcation, and Hopf bifurcation.

At bifurcation points associated with saddle-node, pitchfork, and transcritical bifurcation, only branches of fixed points or static solutions meet. Hence, these three bifurcations are classified as static bifurcations. In contrast, branches of fixed points and periodic solutions meet at a hopf bifurcation point. Hence, a Hopf bifurcation is classified as a dynamic bifurcation.

In this Dissertation, we faced only systems that deal with static bifurcation of fixed points. Hence let us now give the definition of a static bifurcation. A static bifurcation of a fixed point of (A.1) occurs at a certain value of μ, say $\mu = \mu_0$, if the following conditions are satisfied:

1. $\mathbf{F}(x_0; \mu_0) = \mathbf{0}$

2. The Jacobian matrix $\mathbf{D_x F}$ evaluated at $(\mathbf{x_0}; \mu_0)$ has a zero eigenvalue while all of its other eigenvalues have negative real parts.

It is clear that the first condition ensures that the considered solution is a fixed point of (A.1), while the second condition implies that this fixed point is a nonhyperbolic fixed point. We note that these conditions are necessary but not sufficient.

A.3 Continuation Schemes

Continuation schemes are used to determine how solutions of (A.1) vary with a certain parameter. These schemes are based on the Implicit Function Theorem. There are two categories of continuation schemes. The first category consists of predictor-corrector methods, which approximately follow a branch of solutions. The second category consists of piecewise-linear or simpical methods, which exactly follow a piecewise-linear curve that approximates a branch of solutions.

Among the above two categories, there are many types of continuation methods, such as the sequential scheme, the Davidenko Newton-Raphson scheme, the arclength scheme, and the pseudo-arclength scheme. In the arclength scheme, the arclength s along a branch of solutions is used as the continuation parameter. So, $\mathbf{x}$ and μ are considered to be function of s; that is, $\mathbf{x} = \mathbf{x}(s)$ and $\mu = \mu(s)$. This parameterization is useful in carrying out a continuation along a path with a saddle-node bifurcation. On the path parameterized by the arclength s, we seek $\mathbf{x}$ and μ such that

$$\mathbf{F}(\mathbf{x}(s); \mu(s) = \mathbf{0} \tag{A.7}$$

Thus, differentiating equation (A.7) with respect to s yields

$$\mathbf{F}_{\mathbf{x}}(\mathbf{x}; \mu)\mathbf{x}' + \mathbf{F}_{\mu}(\mathbf{x}; \mu)\mu' = \mathbf{0} \tag{A.8}$$

where $\mathbf{x}' = \frac{d\mathbf{x}}{ds}$ and $\mu' = \frac{d\mu}{ds}$. Hence, equation (A.8) can be written as

$$[\mathbf{F}_{\mathbf{x}}|\mathbf{F}_{\mu}]t = [\mathbf{F}_{\mathbf{x}}|\mathbf{F}_{\mu}][\mathbf{x}'\mu']^T = \mathbf{0} \tag{A.9}$$

where the $(n+1)$ vector $\mathbf{t}$ is the tangent vector at $(\mathbf{x}; \mu)$ of the path. The system (A.8) consists of n linear algebraic equations in the $(n+1)$ unknowns $\mathbf{x}'$ and μ'. To uniquely specify these

unknowns, we supplement A.7) with an inhomogeneous equation. A convenient additional equation is specified by the Euclidean arclength normalization defined as

$$\mathbf{x}'^T\mathbf{x}' + \mu'^2 = 1 \tag{A.10}$$

The initial conditions for equations (A.8) and (A.10) are given by $\mathbf{x} = \mathbf{x_0}$ and $\mu = \mu_0$ at $s = 0$. If the Jacobian matrix $\mathbf{F_x}$ is nonsingular and $\mathbf{F}_\mu$ is a zero vector, equations (A.8) and (A.10) yield

$$\begin{bmatrix} \mathbf{x}'^T & \mu' \end{bmatrix} = \pm \begin{bmatrix} 0 & 0 & \dots & 0 & 1 \end{bmatrix} \tag{A.11}$$

If $\mathbf{F_x}$ is singular and $\mathbf{F}_\mu$ is a nonzero vector, one can solve equations (A.8) and (A.10) to determine the tangent vector $\mathbf{t}$ as follows. First, solve the system of n linear algebraic equations

$$\mathbf{F_x}(\mathbf{x};\mu)\mathbf{Z} = -\mathbf{F}_\mu(\mathbf{x};\mu) \tag{A.12}$$

for the vector $\mathbf{Z}$. Then owing to the linearity of equation (A.8) in x' and μ', we write

$$\mathbf{x}' = \mathbf{Z}\mu' \tag{A.13}$$

where μ' is still unknown. Substituting equation (A.13) into the arclength equation (A.10) yields

$$\mu' = \pm\frac{1}{\sqrt{(1 + \mathbf{Z^T Z})}} \tag{A.14}$$

where the plus and minus signs determine the direction of the continuation. Having determined the tangent vector $\mathbf{t}$, we use it to predict the values of $\mathbf{x}$ and μ at $s = \Delta s$ according to $\mathbf{x} = \mathbf{x_0} + \mathbf{x}'\mathbf{\Delta s}$ and $\mu = \mu_0 + \mu'\Delta s$. These predicted values can be corrected by using a Newton-Raphson procedure, and the predictor-corrector scheme is continued until the branch is traced. The choice of the step size Δs should be such that the initial guess or estimate is within the radius of convergence of the corrector. The step size may have to be adaptively varied during the continuation.

VITA

Ayman Aly El-Badawy was born on August 17, 1972 in Cairo, Egypt. In 1988, he enrolled in the Department of Mechanical Engineering at the American University in Cairo, where he obtained his Bachelor's degree in 1993 and his Master's degree in 1995. Subsequently, he joined the Department of Mechanical Engineering at Virginia Tech, where he completed his doctoral studies in March of 2000.